Catalytic Conversion of e-Methanol to eSAF with Thermal System Integration of Modeled Amine-Based Carbon Capture, Alkaline Water Electrolysis, Methanol Synthesis, and Experimental-Based Methanol-to-Hydrocarbons

Aske V. Blankenfeldt, & Rasmus A. B. Morel

Thermal Energy & Process Engineering, TEPE4-1006, 2025-06

M.Sc. Master Thesis

STUDENT REPORT

AALBORG UNIVERSITY

AAU Energy
Aalborg University
http://www.aau.dk

AALBORG UNIVERSITY
STUDENT REPORT

Title:
Catalytic Conversion of e-Methanol to eSAF with Thermal System Integration of Modeled Amine-Based Carbon Capture, Alkaline Water Electrolysis, Methanol Synthesis, and Experimental-Based Methanol-to-Hydrocarbons

Theme:
Master Thesis

Project Period:
Spring Semester 2025

Project Group:
TEPE4-1006

Participants:
Aske Vincent Blankenfeldt
Rasmus Ask Bjørnemose Morel

Supervisor:
Kamaldeep Sharma
Thomas Helmer Pedersen

Number of Pages: 96

Date of Completion:
May 28th - 2025

Abstract:

This thesis explores the methanol-to-jet (MTJ) pathway as a route for sustainable aviation fuel (SAF) production. The study investigates the potential energy savings of co-locating carbon capture using monoethanolamine, H_2 production via alkaline water electrolysis, and methanol synthesis from CO_2 and H_2, in correlation with experimental catalytic conversion of methanol-to-hydrocarbons (MTH), by heat-integration. Experimental investigations were conducted using various zeolite-based catalysts, modified with metals such as cobalt, nickel, and indium, to evaluate their performance in converting wet methanol into liquid hydrocarbons. Analytical methods like simulated distillation, gas chromatography mass-spectroscopy, and thermogravimetric analysis revealed that Co-ZSM-5(50) favored stable aliphatic production in the gasoline range. Ni-ZSM-5(50) presented opposite results, favouring aromatic production in the kerosene range, at a significantly reduced lifetime, and increased coke formation, whereas In-ZSM-5(50) exhibited intermediate behavior. Pinch analysis showed that system efficiency for liquid fuel production increased by nearly 50% with the addition of heat integration, emphasizing its value. The model also revealed an overall carbon and hydrogen efficiency between 8.85% and 16.69%, and 2.94% and 5.83%, respectively.

Summary

Through increase in *Carbon dioxide* (CO_2) emissions, the requirement for decarbonization of the aviation sector is increasing rapidly. Sustainable Aviation Fuel (SAF) has been proposed as a viable route for achieving net-zero emissions. This study focuses on the *Methanol-to-Jet* (MTJ) pathway, a subbranch of *alcohol-to-jet* (ATJ) and *electro-SAF* (eSAF) fuel production. Through the utilization of renewable energy sources, MTJ distinguishes itself from other biofuel processes. MTJ's unlimited potential, through integration with carbon capture (CC) processes and renewable H_2 production, makes it a viable contender to reach the submandate of the Paris agreement, which aims to supply 75% of all jet fuel consumption through SAF.

The objective of this thesis is to asses and improve the entire MTJ fuel production line from well-to-wake through theoretical modeling of monoethanolamine (MEA) CC, alkaline water electrolysis (AWE), and methanol synthesis, with the extension of an experimental Methanol-to-hydrocarbon (MTH) model. Additionally, it aims to investigate the influence of the catalytic selectivity of various zeolite-based catalysts to improve the production of hydrocarbons (HC) in the kerosene range.
Utilization of CO_2 and H_2 from CC and AWE, respectively, acted as inputs for a e-methanol synthesis conversion model, with high carbon and hydrogen efficiencies of 98.26% and 65.51%, respectively. A significant emphasis was placed on recirculation to enhance conversion efficiency and minimize resource consumption. The methanol produced was then utilized in the MTH process, where it was catalytically converted into HCs suitable for aviation fuel.

Experimentally, the study explored the performance of various ZSM-5-based catalysts, including variants modified by metal impregnation with cobalt, nickel, and indium. These catalysts were tested using wet methanol as feedstock. Gas chromatography-mass spectrometry (GC-MS) and simulated distillation (SimDist) techniques were employed to characterize product composition and determine yield distributions. Aromatic and aliphatic selectivity and catalyst lifetime were found to be influenced by the acidity and metal content of the zeolites. H-ZSM-5(23) exhibited an aromatic selectivity of 84.84%, while Co-ZSM-5(50) demonstrated a higher yield of aliphatic compounds, making it more suitable for producing kerosene-like fuels.

Thermogravimetric analysis (TGA) was utilized to assess coke formation and catalyst deactivation, indicating that while Ni-ZSM-5(50) produced the highest yield in jet-fuel range HC, it suffered from reduced catalytic lifetime. The experimental data were also used to inform and refine the MTH synthesis model, allowing for better prediction of selectivity, heat generation, and system-level performance under different catalyst configurations.

To evaluate the viability and performance of the MTJ system, a comprehensive model was developed, integrating both theoretical and experimental approaches. The system

modeling considered energy consumption, catalyst selectivity, and overall system efficiency. A pinch analysis was conducted to evaluate the benefits of thermal integration, revealing that significant energy savings can be achieved through co-location of CC, H_2 production, methanol synthesis, and a MTH conversion process. Heat integration reduced external heating requirements by up to 10.2%, with most cooling demands met by district heating (DH) systems.

The study concluded that the MTJ pathway, when combined with optimized catalyst selection and system integration, presents a promising strategy for large-scale SAF production. Despite the inability to meet Jet-A quality requirements in terms of lower heating value (LHV) due to the simplified product spectrum, the results underscore the importance of complex molecular composition in achieving commercial viability. Moreover, the integrated approach offers substantial potential in reducing energy consumption, thereby improving economic feasibility.

In summary, this thesis provided a detailed analysis of how renewable methanol can be catalytically converted into HCs, emphasizing the importance of catalyst development and thermal integration. The findings support further exploration of MTJ as a scalable and efficient route for SAF production, especially under climate goals aligned with the Paris Agreement.

Preface

This master thesis is developed by the 10^{th} semester students in group TEPE4-1006 from AAU Energy at Aalborg University. Kamaldeep Sharma and Thomas Helmer Pedersen deserve appreciation for providing useful supervision throughout the project. Furthermore, additional thanks goes to Sebastian Bruhn Petersen and Anders Høndrup Andersen for providing assistance with theoretical modeling and technical construction of experimental setup for the laboratorium.

Expectations for the Reader

The reader is expected to have a general understanding of chemical reactions, chemical compounds, reaction mechanisms, and thermodynamics.

Reading Guide for the Project

Throughout the project, various tables, figures, and equations will be numbered individually. The references implemented throughout the project follow the Oxford referencing method. Figures, calculations, and additional theory not included in the project can be found in the Appendix.

The following software has been used in the project:

- F-Chart Software - Engineering Equation Solver (EES)
- Mathworks - MATLAB
- Microsoft - Office365
- Overleaf - Latex
- Draw.io AG & JGraph Ltd - Draw.io
- Aspen Plus

Rasmus Ask Bjørnemose Morel

Signature: 

Aske Vincent Blankenfeldt

Signature: 

Nomenclature

Symbol	Explanation	Unit
ε	Bed voidage	[-]
ζ	Extent of reaction	[-]
η_{AWE}	Alkaline Water Electrolysis Efficiency	[%]
η_{C}	Carbon Efficiency	[%]
$\eta_{\mathrm{CO_2,Capture}}$	CO_2 Capture Efficiency	[%]
η_{H}	Hydrogen Efficiency	[%]
η_{mv}	Murphree Efficiency	[-]
η_{Tot}	Total System Efficiency	[%]
$\hat{\eta}$	Overpotential	[V]
φ	Volume Fraction	[-]
ρ	Density	[kg/m^3]

Symbol	Explanation	Unit
A_{Cell}	Cell Area	[m^2]
C	Concentration	[mol/L]
c_{KOH}	Potassium concentration	[wt.%]
d_p	Particle Diameter	[mm]
$EJFE$	Energetic Jet fuel Efficiency	[%]
G	Gibbs free energy	[kJ/mol]
H/C	Hydrogen-to-Carbon	[-]
ΔH^0	Enthalpy of formation at standard conditions	[kJ/mol]
HHV	Higher Heating Value	[MJ/kg]
I	Current	[A]
i	Current Density	[A/m^2]
K_{eq}	Equilibrium constant	[-]
k_H	Henrys constant	[$mol \cdot L^{-1} \cdot bar^{-1}$]
L/G	Liquid-to-gas Ratio	[kg/kg]
LHV	Lower Heating value	[MJ/kg]
m	Mass	[kg]
$\dot{m}$	Mass flow rate	[tonne/hr]
MW	Molar Weight	[kg/kmol]
n	Number of mole	[mol]
$\dot{n}$	Molar flow rate	[kmol/hr]
N	Number of Cells	[-]
p_i	Partial pressure of component i	[bar]
$p^*_{i,vapor}$	Vapor pressure of component i at equilibrium	[bar]
P	Pressure	[bar]
Q	Heat	[MW_{th}]
Re	Reynolds Number	[-]
T	Temperature	[°C]
ΔT_{min}	Minimum temperature difference	[°C]
u	Fluid velocity	[m/s]
V_{Cell}	Cell Voltage	[V]
V_{Rev}	Nernst Potential	[V]
$\dot{V}$	Volumetric Flow Rate	[ml/min]
W	Electrical Work	[kW_e]
$WHSV$	Weight hour space velocity	h^{-1}
x_i	liquid mole fraction of component i	[mol/mol]
y_i	Vapor mole fraction of component i	[mol/mol]

Symbol	Explanation	Value	Unit
d_1	Polarization curve constant	-3.12996×10^{-6}	[Ω m^2]
d_2	Polarization curve constant	4.47137×10^{-7}	[Ω m^2 bar^{-1}]
f_{11}	Faraday efficiency constant	478645.74	[A^2 m^{-4}]
f_{12}	Faraday efficiency constant	-2953.15	[A^2 m^{-4} $^\circ$C^{-1}]
f_{21}	Faraday efficiency constant	1.03960	[-]
f_{22}	Faraday efficiency constant	-0.00104	[$^\circ$C^{-1}]
r_1	Polarization curve constant	4.45153×10^{-5}	[Ω m^2]
r_2	Polarization curve constant	6.88847×10^{-9}	[Ω m^2 $^\circ$C^{-1}]
s	Polarization curve constant	0.33824	[V]
t_1	Polarization curve constant	-0.01539	[m^2 A^{-1}]
t_2	Polarization curve constant	2.00181	[m^2 $^\circ$C^2 A^{-1}]
t_3	Polarization curve constant	15.24178	[m^2 $^\circ$C^2 A^{-1}]

Abbreviation	Explanation
ASTM	American Society for Testing and Materials
ATJ	Alcohol-to-Jet
ATJ-SPK	Alcohol-to-Jet Synthetic Paraffinic Kerosene
AWE	Alkaline Water Electrolysis
BAS	Brønsted Acid Sites
BTX	Benzene, toulene, xylene
CC	Carbon Capture
CCS	Carbon Capture and Storage
CCV	Composite Curves
CH-SK	Catalytic Hydrothermolysis Kerosene
CHP	Combined Heat and Power
CW	Cooling Water
DAC	Direct Air Capture
DCP	Dual-Cycle Process
DME	Dimethylether
EJFE	Energetic Jet fuel Efficiency
ELECNRTL	Electrolyte non-random two liquid
EOS	Equation of state
eSAF	ElectroSAF
FT	Fischer-Tropsch
FT-SPK	Fischer-Tropsch Synthetic Paraffininc Kerosene
GC	Gas Chromatography
GC-MS	Gas ChromatographyMass Spectrometry
GCC	Grand Composite curve
GHG	Greenhouse gases
GTJ	Gas-to-Jet
HC	Hydrocarbons
HEFA	Hydroprocessed Esters and Fatty Acids
HFS-SIP	Hydroprocessed Fermented Sugars to Synthetic Isoparaffins
HP	High Pressure
LAS	Lewis Acid Sites
LP	Low Pressure
LPG	Light Petroleum Gas
MB	Mass Balances
MeSAF	Methanol to Sustainable Aviation Fuel
MP	Medium Pressure
MSC	Multi-stage Compression
MTH	Methanol-Hydrocarbons
MTJ	Methanol-to-Jet

Abbreviation	Explanation
MTO	Methanol-to-Olefins
NMR	Nuclear Magnetic Resonance
NRTL	Non-random two liquid
n-MR	n-Membered Rings
OSHA	Occupational Safety and Health Administration
OTJ	Oil-to-Jet
PBR	Packed Bed Reactor
ppm	Parts Per Million
PSCC	Point Source Carbon Capture
PSRK	Predictive-Redlich-Kwong-Soave
PtL	Power-to-Liquid
Redox	Oxidation-Reduction
RWGS	Reverse Water-gas-Shift
SAF	Sustainable Aviation Fuel
SimDist	Simulated Distillation
SPK	Synthetic Paraffinic Kerosene
STJ	Sugar-to-jet
TGA	Thermogravimetric Analysis
TOS	Time on Stream
VLE	Vapor-Liquid Equilibrium
WGS	Water-gas-Shift

Chemical Formula	**Chemical Name**
Al	Aliminium
AlO_4^-	Alumina Tetrahedra
C	Carbon
CH_3OH	Methanol
CH_3OCH_3	Dimthylether
$((CH_3COO)_2CO \cdot 4H_2O)$	Cobalt(II) acetate tetrahydrate
CO	Carbon Monoxide
CO_2	Carbon Dioxide
CO_3^{2-}	Carbonate
Co	Cobalt
Cu	Cobber
Ga	Gallium
H^+	Proton
H_2	Hyrdrogen
H_2O	Water
H_3O^+	Hydronium
HCO_3^-	Bicarbonate
In	Indium
$(In(NO_3)_3 \cdot 5H_2O)$	Indium(III) nitrate hydrate
KOH	Potassium Hydroxide
MEA	Monoethanolamine
$MEACOO^-$	Carbamate
$MEAH^+$	Protonated Monoethanolamine
N_2	Nitrogen
NH_4	Ammonium
Ni	Nickel
$(Ni(NO_3)_2 \cdot 6H_2O)$	Nickel(II) nitrate hexahydrate
O_2	Oxygen
OH^-	Hydroxide
S	Sulfur
SiO_4	Silicon Tetrahedra
V	Vanadium
Zn	Zink

Contents

Chapter 1

Introduction

The Industrial Revolution has greatly influenced living standards since the 18th century but has also been the beginning of the rise of *carbon dioxide* (CO_2) emissions with the widespread use of fossil fuels. With human activity, increasing CO_2 and other *greenhouse gases* (GHG) emissions, enhancing the greenhouse effect, and contributing to global warming, climate change poses the largest threat to the survival of humanity. Since the beginning of the Industrial Revolution in the 18th century, the CO_2 concentrations have risen by over 50%, from 280 ppm in 1780 to 426 ppm as of February 2025 [1]. Moreover, annual global CO_2 emissions have risen to 37.8 $GtCO_2$ in 2023, an increase of almost 45% since 2000 [2]. To combat the increase of CO_2 emissions and the threat of global warming, the Paris Agreement, aiming to limit global temperatures to 1.5°C above pre-industrial levels and achieve CO_2 neutrality by 2050, was signed in 2015 by 196 countries [3]. To achieve this goal, decarbonization of all sectors has begun. The transport sector contributes to approximately 21% of the total annual CO_2 emissions, of which a majority of above 75% is contributed by road transportation, which is rapidly being decarbonized by electrification. While aviation only accounted for 9.9% of the transport sector or roughly 2.5% of the total annual CO_2 emissions, global air traffic is expected to grow by 250% within the next 20 years, leading to an increase in CO_2 emissions projected to reach as high as 1.9 $GtCO_2$ or 3.4 $GtCO_{2e}$ in 2050 [4] [5][6][7]. A solution to these projected emissions in the aviation sector, has to be found, and with only around 10% of the aviation sector that can undergo direct electrification, covering short-distance flights only by 2050, other solutions must be found. [8].

To decarbonize the aviation sector, a four-pillar strategy has been proposed. This aims to reduce air transport demand by improving infrastructure and flight paths, technological improvements to increase energy efficiencies, market-based actions for emission trading, as well as the implementation of *Sustainable Aviation Fuels* (SAF). [4] [9]. Figure 1.1 shows historical CO_{2e} emissions from 1990-2021 and projected emissions from 2022-2050 for three scenarios of varying carbon intensities.

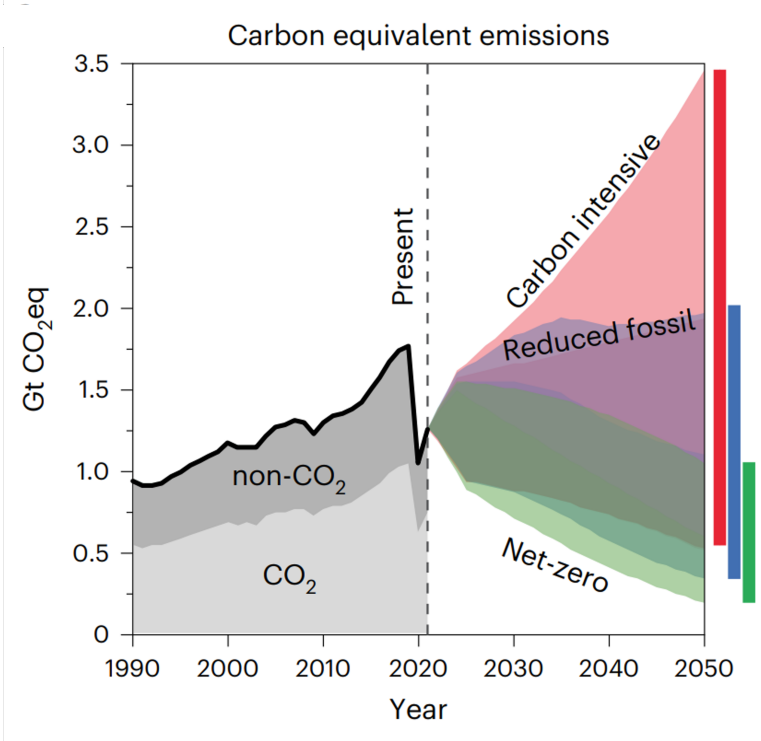

Figure 1.1: Historical and projected CO_{2eq} emissions from 1990-2021 and predicted emissions from 2022-2050, depending on the chosen scenario [4]

Firstly, 'Carbon intensive' governs the CO_{2e} of continuing to rely on fossil jet fuels. Secondly, the 'Reduced fossil' pathway implies 65% of medium- and long-haul aviation in 2050 is met by SAF, while short-haul flights are met by a combination of 13% non-emitting propulsion systems, 57% SAF and 30% fossil jet fuel [4]. Lastly, the 'Net-Zero' pathway governs no combustion of fossil fuels, where both medium- and long-haul flights are 100% replaced by SAF and short-haul flights are powered by 50% non-emitting propulsion systems and SAF.

As of 2024 SAF production only represents 0.53% of global jet fuel use, while the ReFuelEU Aviation Regulation mandates a minimum supply of SAF of 2% by 2025, increasing to 70% by 2050, with a sub-mandate of 35% synthetic *electroSAF* (eSAF) produced from green hydrogen [10]. As of now, safety regulations ensuring international standards for both safety and performance of aviation fuel limit blend ratios of SAF with fossil-based jet fuel to 50%, with goals of reaching 100% SAF drop-in fuel by 2030. Furthermore, SAF is currently 3-10 times more expensive than conventional jet fuel, depending on the production route. However, the price of SAF is expected to reduce substantially as production technologies scale up [10]. However, as the production scale up, improving energy integration across production units is crucial for reducing operating costs and enhancing the economic feasibility of large-scale SAF

production. Efficient use of heat and energy can significantly support upscaling efforts and improve overall process sustainability. Furthermore, to achieve 70% SAF supply by 2050, intensified research into better replicating the properties of conventional jet fuel is needed to enable 100% drop-in compatibility. Since SAF must meet the same stringent regulatory and performance standards as fossil-based jet fuels [11], a deeper understanding of conventional jet fuel composition is essential to overcome limitations related to chemical compatibility and supply potential.

1.1 Conventional Jet Fuel

Conventional or fossil jet fuel is a mix of *hydrocarbons* (HCs) produced by fractional distillation of crude oil. Depending on the application and the environment in which the fuel is used, different specifications and standards of various organizations must be complied with. For commercial use in the USA, standards set by *American Society for Testing and Materials* (ASTM) must be upheld. In addition to ASTM, standards set by the UK Defence Standardization and International Air Transport Association are required for international use[12]. These standards ensure safety and performance requirements are upheld and allow for certain additives to the jet fuel to change certain properties depending on the application.

To produce jet fuel that upholds these standards and safety regulations, the crude oil is distilled and separated based on boiling temperature, in a process called fractional distillation. Depending on the regulatory requirements, HC components that boil within the range of 150 °C and 280 °C are typically defined as kerosene and usually have carbon lengths C_8-C_{16}. If the distilled kerosene does not meet the required standards, it can undergo various upgrading processes and be supplemented with additives to enhance its quality.

After kerosene is distilled and upgraded, it must be analyzed and categorized based on its chemical composition and intended application. Mainly three types of conventional jet fuel are in use: Jet A, Jet A-1, and Jet B. Jet A and Jet A-1 are primarily composed of highly refined kerosene, with Jet A-1 being more widely used internationally due to its lower freezing point. Jet B, on the other hand, is a wide-cut fuel consisting of approximately 65% kerosene and 35% gasoline, making it suitable for colder climates due to its higher volatility and better cold flow properties, acquired from the addition of gasoline. The physical properties of the three commercialized jet fuels can be seen in Table 1.1. However, jet B is less utilized due to its increased volatility, thereby reducing the safety. The application where the different types of jet fuels are utilized or required is highly dependent on the chemical properties of the fuel. [13] [14]

Fuel		**Jet A Kerosene**	**Jet A-1 Kerosene**	**Jet B wide-cut**
Flash Point [°C]	Min.	38	38	-18
Freezing Point [°C]	Max.	-40	-47	-51
Specific Energy [MJ/kg]	Min.	42.8	42.8	42.8
Density @ 15 °C [kg/m^3]		775-840	775-840	751 - 802
Distillation [°C]:				
Initial boiling point		-	Report	Report
10% Recovered	Max.	205	205	Report
50% Recovered		Report	Report	Min 125; Max 190
90% Recovered	Max.	Report	Report	Report
End point		300	300	270
Approximate HC Length		C_8 - C_{16}	C_8 - C_{16}	C_5 - C_{15}

Table 1.1: Physical properties of commonly used commercial jet fuels [11] [15] [16] [17]. [14]

1.1.1 Properties of Conventional Jet Fuel

Kerosene-type jet fuels, characterized by their boiling point within the kerosene range, are composed of a mixture of hundreds of different aliphatic and aromatic compounds [11]. The mixture of aliphatic and aromatic compounds influences the physical properties of the jet fuel, as the different HC classes exhibit different properties depending on their structures. This influences the jet fuel mixture's overall cold flow properties, combustion quality, and energy contents, as seen in Table 1.2. An illustration of different aliphatic and aromatic compounds can be seen in Figure 1.2.
The freezing point is heavily influenced by the HC classes' molecular structure, with n-paraffins and unsubstituted aromatics crystallizing at much higher temperatures than other HC classes, as their geometry allows them to easily pack together into a crystalline structure. To ensure good cold flow properties and avoid possible clogging within the pump systems, low freezing points are favorable.

	Hydrocarbon Class			
Jet Fuel Property	**n-Paraffin**	**Iso-paraffin**	**Cycloaliphatics**	**Aromatic**
Gravimetric energy content	+	+	0	-
Volumetric energy content	-	-	0	+
Combustion quality	+	+	+	-
Low-temperature fluidity	- -	0/-	+	0/-

Table 1.2: Contributions of different HC classes to the jet-fuel mixture. "+" indicates a beneficial effect, "0" indicates a neutral or minor effect, and "-" indicates a negative effect [11]

The energy content of the different HC classes also differs as their densities differ. In general, longer carbon chains result in higher densities; however, for compounds of the same carbon number, aromatics have the highest density, followed by naphthenes and then paraffins. Consequently, this results in paraffins' gravimetric energy content

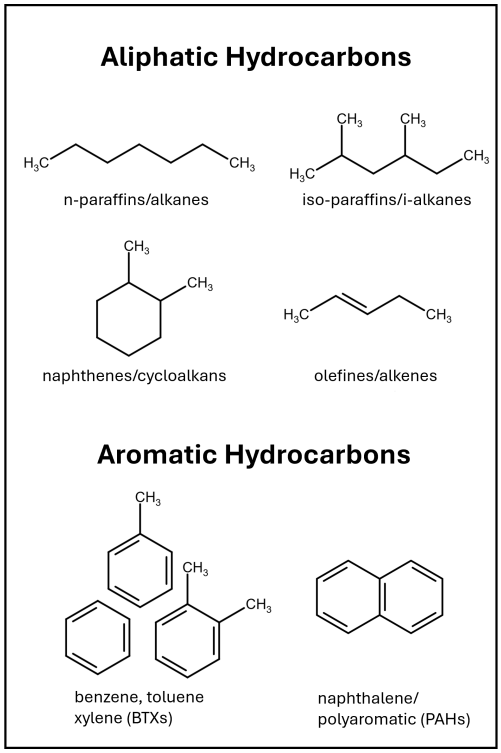

Figure 1.2: Representation of different classes of aliphatic and aromatic HCs. The xylene shown is o-xylene and has 3 different isomers. [18]

followed by naphthenes and then aromatics for the same number of carbon atoms, with the order reversed for volumetric energy content. Apart from the energy content of the HC classes, the combustion quality is also influenced. Aromatics have the lowest *hydrogen-to-carbon* (H/C) ratio, resulting in more soot formation and particulate pollution. The ring formation of aromatics also has the strongest bonds, requiring the most energy to break, which can also lead to slower and incomplete combustion. However, the aromatic compounds exhibit lubricating properties required to lubricate and prevent leakage within the engines. Because of this, a maximum of 25% vol aromatics is allowed within the jet fuel mixture.
Typical Jet A-1 fuel consists of roughly 35-60% paraffins, <1% olefins, as they can lead to gum formation within the engine, 25-35% naphthenes, and 15-25% aromatics depending on the chemical composition of the sourced crude oil. Additionally, a maximum of 3% vol naphthalene is allowed for both Jet A, A-1, and Jet B fuel [19] [20].

The goal of SAF is to mimic the physical and chemical properties of conventional jet fuel utilizing renewable feedstocks. However, currently produced SAF lacks some of the essential chemical compositions of conventional jet fuel, which limits the blend ratio, and thereby demands the usage of conventional jet fuel to uphold the regulations

stated by the ASTM [21]. This is emphasized in Table 1.3, comparing typical chemical compositions of jet fuels produced from various ASTM-certified SAF pathways.

Fuel	n-Paraffin	i-paraffin	Olefin	Cycloaliphatics	Aromatic
Jet A-1	28.8%	39.7%	1.2%	15.5%	14.8%
FT-SPK	19.7%	80.1%	0.1%	0.1%	-
SIP	-	98.5%	0.2%	1.3%	-
HEFA	9.2-12.8%	86.8-90%	0.1%	0.3 - 0.37%	-
ATJ-SPK	-	99.8%	0.2%	-	-
CH-SK	45%	7.1%	33.7%	9%	5.2%

Table 1.3: Chemical composition of Jet A-1, and SAF produced by ASTM-certified production pathways [22]

Expansion upon the currently available methods to produce SAF is needed to reach higher blend ratios and eliminate the requirement of conventional jet fuel.

1.2 Renewables to Sustainable Aviation Fuels

Multiple renewable pathways exist for producing SAF from non-petroleum feedstocks, significantly reducing CO_{2e} emissions. These pathways can be broadly categorized into two types:

1. **Biojet fuel**, derived from biomass-based feedstocks such as sugars, energy crops, forest residues, biowaste, lipids, fats, oils, algae, or biocrude. The specific feedstock and conversion technology determine the final fuel characteristics.

2. **Synthetic Jet Fuels (eSAF)**, produced using renewable electricity in *Power-to-Liquid* (PtL) processes. These involve converting captured CO_2 and green hydrogen (H_2), generated via water electrolysis, into liquid hydrocarbons through methods such as *Fischer-Tropsch* (FT) synthesis or *methanol-to-jet* (MTJ) conversion.

An overview of SAF production routes can be seen in Figure 1.3.

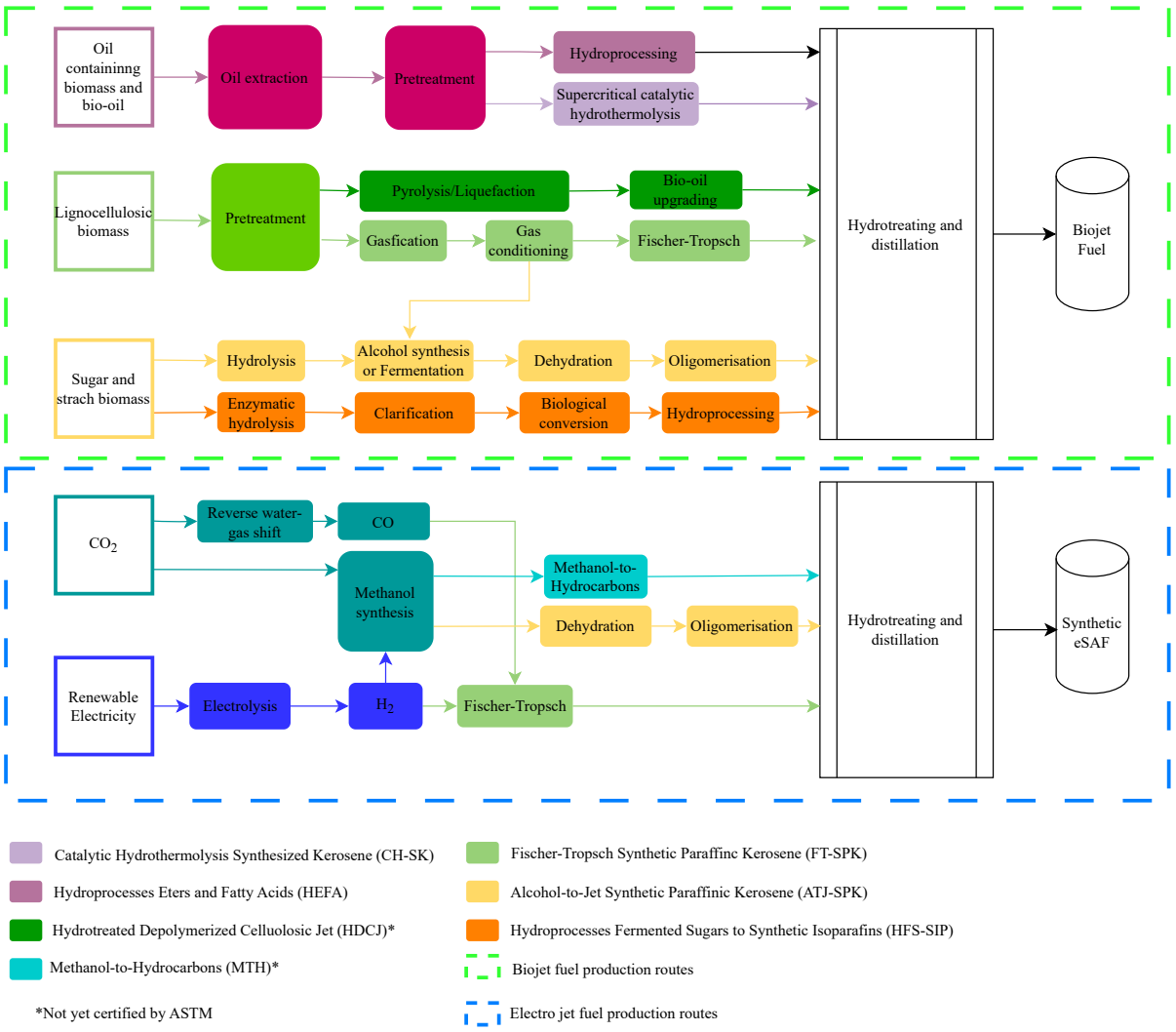

Figure 1.3: Production pathways for biojet fuel and synthetic eSAF utilizing different feedstocks.

1.2.1 Biojet Fuel

Currently, only biojet fuel production routes have been ASTM certified (ASTM D7566), between 2009 and 2020 [23]. Biojet feedstock depends on the production route obtained from triglyceride, lignocellulosic, sugars, and starchy biomasses through a series of conversion pathways, classified into *gas-to-jet* (GTJ), *oil-to-jet* (OTJ), *sugar-to-jet* (STJ) and *alcohol-to-jet* (ATJ). The different ASTM-certified pathways include *Fischer-Tropsch Synthetic paraffinic kerosene* (FT-SPK), utilizing syngas from gasification of lignocellulosic biomass, to produce a linear and branched paraffinic mixture, primarily within the range of kerosene and FT-SPK with the addition of aromatics (FT-SPK/A), *Hydroprocessed Esters and Fatty Acids* (HEFA) utilizing oil-containing biomass and hy-

droprocessing processes to produce paraffinic HCs. *Hydroprocessed Fermented Sugars to Synthetic Isoparaffins* (HFS-SIP) converts sugars and cellulosic biomass to iso-paraffins, through hydroprocesses. *Alcohol-to-Jet Synthetic Paraffinic Kerosene* (ATJ-SPK) converts alcohols to paraffinic kerosene through a series of dehydration, oligomerization and hydrotreating processes. Lastly, *catalytic hydrothermolysis synthesized kerosene* (CH-SK) converts oil-containing biomass to a mixture of HCs through near supercritical catalytic hydrothermolysis, similar to hydrothermal liquefication processes.

Commonly, for all production routes is the primary production of *Synthetic Paraffinic Kerosene* (SPK), leading to a lack of aromatic and cycloaliphatic compounds found in traditional commercial jet A or jet A-1 fuel, leading to blending requirements or the addition of aromatic compounds.
Table 1.4 provides an overview of the current ASTM-certified SAF production pathways and their feedstock, while Table 1.3, provides an overview of the chemical composition of the produced SAF.

SAF Production Pathways				
Pathway	**Feedstock**	**Chemical Process**	**Distilation fraction [Gasoline:Kerosene:Diesel]**	**Blending Ratio**
Fischer-Tropsch Synthetic Paraffinic Kerosene (**FT-SPK**)	Municipal solid waste, agricultural and forest wastes, energy crops	Gasification of biomass into syngas followed by FT synthesis reactions to paraffinic HC mixture	[20:40:40][a]	50%
FT-SPK with Aromatics (**FT-SPK/A**))	Municipal solid waste, agricultural and forest wastes, energy crops	Gasification of biomass into syngas followed by FT synthesis reactions to paraffinic HC mixture with addition of aromatic components	[20:40:40][a]	50%
Hydroprocessed Esters and Fatty Acids (**HEFA**)	Oil-based feedstocks (e.g waste oil, algae, slaughterhouse waste, plant oil, yellow or brown greases)	Hydroprocessing of said feedstocks to break apart long fatty acids, followed by hydroisomerization and hydrocracking	[19:55:26][b]	50%
Hydroprocessed Fermented Sugars to Synthetic Isoparaffins (**HFS-SIP**)	Sugars, cellulosic biomass, pretreated waste fat, oil or greases	Microbial conversion of sugars to HC from celluosic biomass	[0:100:0][c]	10%
Alcohol-to-Jet Synthetic Paraffinic Kerosene (**ATJ-SPK**)	Cellulosic biomass, starchy biomass	Conversion of cellulosic biomass into alcohol which is further converted into synthetic paraffins through a series of chemical reactions, including dehydration, hydrogenation, oligomerization, and hydrotreating processes.	[30:70:0][d]	50%
Catalytic Hydrothermolysis Synthesized Kerosene (**CH-SK**)	Fatty acids, fatty acid esters or lipids from fat oil greases	Converts lipid feedstock into unsaturated triglycerides in a catalytic hydrothermolysis reactor which is further converted into a mixture of iso-paraffins under supercritical conditions.	[25:37:28][e]	50%

Table 1.4: ASTM-certified production routes for SAF. [23] [24] [25] [26]
[a] Optimized for SAF production [27]
[b] Optimized for SAF production, based on vegetable oil, various with feedstock [28]
[c] Primary product of farnesane ($C_{15}H_{32}$)
[d] Based on ethanol [29]
[e] Depended on feedstock, last 10% are unaccounted for [26]

Biojet fuels are produced from biomass-based feedstocks such as agricultural residues, waste oils, and algae. However, these resources are inherently limited and face strong competition from other sectors like renewable heat and power generation. Within the

EU, regulations restrict feedstock to second- and third-generation biomass, further narrowing the available supply and making large-scale expansion challenging. Additionally, the GHG savings from biojet fuel vary significantly depending on the feedstock and conversion process, with some pathways even emitting more than conventional jet fuel. Despite its limitations, biojet fuel remains crucial in the near term due to its compatibility with existing infrastructure and more mature production pathways. [30] [31]

1.2.2 Synthetic Jet Fuel

In contrast to biojet fuel, eSAF offers a more scalable and potentially sustainable long-term solution. Produced from captured CO_2 and green hydrogen using renewable electricity, eSAF is not constrained by biomass availability, land use, or feedstock competition. This makes it particularly attractive for the large-scale decarbonization of aviation required to reach the 2050 goals.
As illustrated in Figure 1.3, there are two primary pathways for eSAF production, consisting of FT synthesis which uses syngas consisting green hydrogen and CO derived by *reverse water-gas shift* (RWGS) of captured CO_2, and MTJ processes, which convert e-methanol, also synthesized from green hydrogen and CO_2 into jet fuel.

Contrary to biojet fuels, synthetic jet fuel produced from captured CO_2 and H_2 sourced from electrolysis, does not rely on limited feedstock availability of varying quality and does not compete with land use of agriculture. The usage of captured CO_2 and green hydrogen in a PtL process, also makes eSAF theoretically net zero-emission, if sustainably integrated. However, both electrolysis and CO_2 capture require a lot of electricity and have low overall efficiencies due to losses in all conversion steps. This makes the use of electricity to produce eSAF inefficient, with an overall well-to-wake efficiency of 12-15%, depending on whether FT synthesis or MTJ conversion is used. This efficiency is significantly lower than the direct electrification of electric vehicles with an efficiency of around 80% [32] [33].

Due to the low well-to-wake efficiency, the required energy to produce 1 tonne of eSAF is significantly higher than that of biojet fuel, primarily due to the production of green hydrogen requiring vast amounts of electricity, corresponding to higher costs of eSAF. Depending on the source of CO_2 the associated energy requirements also differs corresponding to higher prices. In Table 1.5 a price comparison between conventional jet fuel, biojet fuel and eSAF produced from CO_2 sourced by *point source carbon capture* (PSCC), or directly from the atmosphere in *direct air capture* (DAC), can be seen.

Production Method	Price [$/L]
Conventional Jet Fuel	0.60
Biojet Fuel	0.79-2.49
$eSAF_{PSCC}$	2.70
$eSAF_{DAC}$	4.02

Table 1.5: Minimum selling prices of eSAF, biojet fuel, and average selling price of conventional jet fuel [34][35]

For eSAF to become commercially competitive, the high cost must be driven down to a commercial level, which is estimated to be \$1.12-1.28/L. These reductions mainly lie in the electrolyzer systems, carbon capture (CC) systems, and renewable electricity production[33]. For eSAF to meet the ReFuelEU Aviation Regulations sub-mandate of 35% eSAF by 2050, the production must be ramped to a degree of significance.

Among the two main eSAF production pathways, FT and MTJ both offer significant potential for large-scale deployment. However, MTJ presents several practical advantages over FT, particularly in terms of storage, transport, and process conditions, as hydrogen is challenging to store. In contrast, methanol is a stable liquid at ambient conditions, making it easier and more cost-effective to handle. Furthermore, methanol is a widely used intermediate in the chemical industry, serving as a precursor for formaldehyde in urea-based fertilizers, and as a feedstock in processes like methanol-to-propylene for plastics production. Additionally, FT synthesis requires the conversion of CO_2 to CO via RWGS, which adds additional complexity to the system and requires high temperatures and pressures up to 750 °C and 45 bars [36] [37]. In contrast, methanol synthesis and MTJ processes operate under milder conditions at lower temperatures under 400 °C and potentially lower pressures [38]. This offers potential benefits in terms of energy efficiency and system integration. This report, therefore, focuses on the MTJ pathway.

1.3 Methanol-to-Jet

As illustrated in Figure 1.3, the MTJ pathway consist of two main production routes. The first involves methanol dehydration to light olefins via the *methanol-to-olefins* (MTO) process, followed by oligomerization, hydrotreating, and distillation to produce SPK. However, as discussed earlier, the production of SPK introduces limitations regarding the imitation of conventional Jet fuel, due to its lack of aromatics and cycloaliphatics, limiting its possible blend ratio.

Alternatively, methanol can also be converted into synthetic fuels through *methanol-to-hydrocarbons* (MTH), of which the HCs within the jet fuel range will consist of a mixture of HCs, more representative of conventional jet fuel, by introducing a series

of secondary reactions. While the MTH process can theoretically yield HCs of varying chain lengths suitable for different fuel types, the actual product distribution is constrained by the selectivity of the catalysts used, which govern the dominant reaction pathways and limit the range of HCs efficiently produced.

The MTJ process begins with the synthesis of methanol from CO_2 and green hydrogen, as shown in Reaction (R 1.1):

$$CO_2 + 3H_2 \rightleftharpoons CH_3OH + H_2O \qquad \Delta H^0 = -49 kJ/mol \qquad \text{(R 1.1)}$$

Methanol undergoes an initial dehydration to dimethyl ether (DME), as shown in Reaction (R 1.2):

$$2CH_3OH \rightleftharpoons CH_3OCH_3 + H_2O \qquad \Delta H^0 = -23.5 kJ/mol \qquad \text{(R 1.2)}$$

DME acts as an intermediate before it turns into ethene, in the next exothermic dehydration reaction, and can be seen in Reaction R 1.3. [39]

$$CH_3OCH_3 \rightleftharpoons C_2H_4 + H_2O \qquad \Delta H^0 = 52.4 kJ/mol \qquad \text{(R 1.3)}$$

Ethene, due to its high reactivity, plays a key role in forming longer-chain HCs through oligomerization and other secondary reactions. These reactions are central to both MTO and MTH pathways.

1.3.1 Single Stage Catalytic Conversion Process

To enhance the chemical composition of eSAF and increase blend ratios, research has explored combining MTO and MTH processes into a single-stage catalytic system. Mentzel et al. [40] proposed using acidic zeolite-based catalysts in a continuous packed bed reactor (PBR) to promote secondary reactions such as aromatization and cyclization. An illustration of this concept is shown in Figure 1.4.

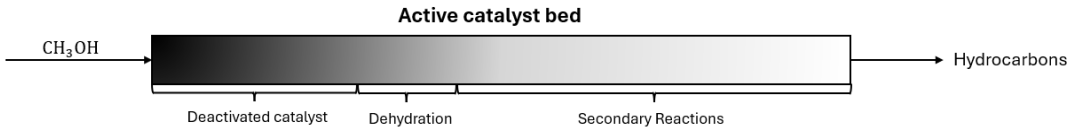

Figure 1.4: Illustration of a PBR to promote secondary reactions [18]

However, this process does not come without drawbacks. As the dehydration reactions end inside the reactor and the secondary reaction starts to be promoted, aromatics are formed. These aromatics can undergo polymerization to form large polyaromatics, which have a higher solidification temperature than the reaction temperature, resulting in hard coke deposits on the catalyst, thereby deactivating it and reducing its

lifetime. Additionally, the formation of aromatic compounds can also exceed the 25 wt.% that is allowed in jet fuel, introducing a new deviation from that of conventional jet fuel [41]. Furthermore, studies have shown that the formation of coke slows the kinetics of the catalyst, altering the chemical composition of the HCs produced, introducing new technical challenges [42].

To overcome these challenges and maximize the yield of jet fuel, catalyst design must be optimized to selectively promote desired secondary reactions while minimizing coke formation. Targeted catalyst modification is therefore essential to improve performance and longevity to ensure high and consistent yields of jet fuel with properties mimicking those of conventional jet fuel [43]. Understanding the underlying reaction mechanisms is therefore essential for advancing the single-stage MTJ approach.

1.4 Reaction Mechanism

The conversion of methanol to HC involves a complex series of reactions, making it impossible to determine a definitive pathway. However, various reaction pathways have been proposed, considering various reaction mechanisms. Here, the most widely accepted reaction pathway is based on a dual-cycle concept, which provides a framework for understanding the formation of HCs over zeolite-based catalysts and is supported by extensive catalyst characterization studies, including *nuclear magnetic resonance* (NMR) spectroscopy and carbene-trapping experiments. [41]

1.4.1 Dual Cycle Concept

Once the initial carbon-carbon bond is formed through the generation of ethene, a steady-state autocatalytic process is initiated to promote the formation of longer HCs. This process, known as the *dual cycle process* (DCP), involves two parallel catalytic cycles that continuously convert methanol into longer-chain olefinic or aromatic HCs, in the olefinic or aromatic cycle, as illustrated in Figure 1.5.

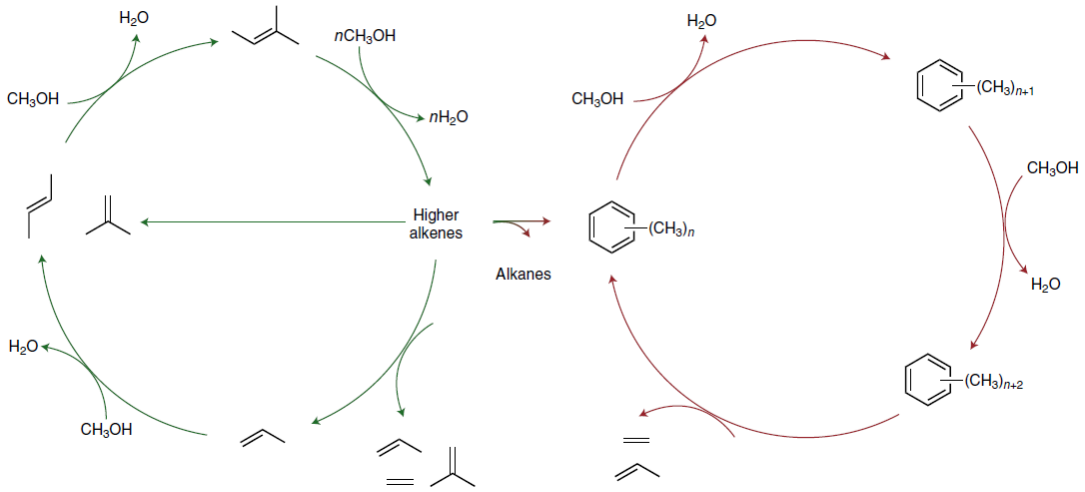

Figure 1.5: Steady-state DCP based on various framework, highlighting the olefinic and aromatic cycle [41]

Here, ethene and other light olefins act as intermediates, reacting with incoming methanol molecules to form higher olefins. The higher alkenes will either remain, leave the DCP by converting to unreactive paraffins through hydrogenation reactions, or enter the aromatic cycle through a series of cyclization and aromatization reactions, governed by dehydrogenation.

The selectivity towards one cycle over the other depends on the acidic properties of the catalyst, while the length of the HCs is primarily dominated by the structural properties of the zeolite. Understanding and tuning these properties of zeolite-based catalysts is therefore essential to optimizing product selectivity and limit the production of aromatic compounds. [41] [44].

1.4.2 Zeolite Catalyst

Zeolite-based catalysts are constructed by porous crystalline grids of silicon and aluminum atoms connected by oxygen atoms to form a framework of *silicon tetrahedra* (SiO_4) and *aluminum tetrahedra* (AlO_4^-), consisting of uniform pores and channels. Depending on the geometry of the structured grid, differently sized uniform pores and channels are formed, allowing for selective molecular diffusion, of which only molecules smaller than the pore size can enter. Different frameworks can hence be engineered to consist of pores of various sizes to tailor the selectivity towards differently sized compounds, depending on the application.

Likewise, the zeolite contains active *Brønsted acid sites* (BAS), which function as proton donors. These are formed with H^+ compensating for the negative charge of AlO_4^-,

creating the Brønsted acid site. Depended on the Si/Al ratio, commonly measured as the SiO_2/Al_2O_3 ratio. In addition to the active BAS, *Lewis Acid Sites* (LAS) function as electron pair acceptors and are typically created with the addition of metal ions to the framework, and promote *oxidation-reduction* (redox) reactions. In addition to redox reactions promoted by LAS, zeolites promote various reactions, including cracking, isomerization, alkylation, and dehydration.
Depending on the acidity of the catalyst, influenced by the SiO_2/Al_2O_3 ratio, leads to selectivity changes as either the olefinic or aromatic cycle will be favored. This is related to the amount of BAS the alumina oxide provides to the framework. Studies have shown that the amount of alumina in the framework directly relates to the selectivity of the catalyst. [41]

Framework

Most commonly used zeolite frameworks contain microscopic pores with sizes ranging from 4 to 10 Å (0.4 to 1.0 nm) formed from rings of Si and Al atoms linked by oxygen ions, of which the (SiO_2/Al_2O_3) ratio can be determined. Larger rings are formed by more atoms linked, referred to as *n-membered rings* (n-MR), where 8-, 10-, and 12-MR containing zeolites are commonly known as small, intermediate and large pores. Depending on the structure of rings, different channel geometries can also be achieved, of which differently shaped molecules will occupy the surfaces of the zeolite. An illustration of the variance in frameworks of different catalysts can be seen in Figure 1.6

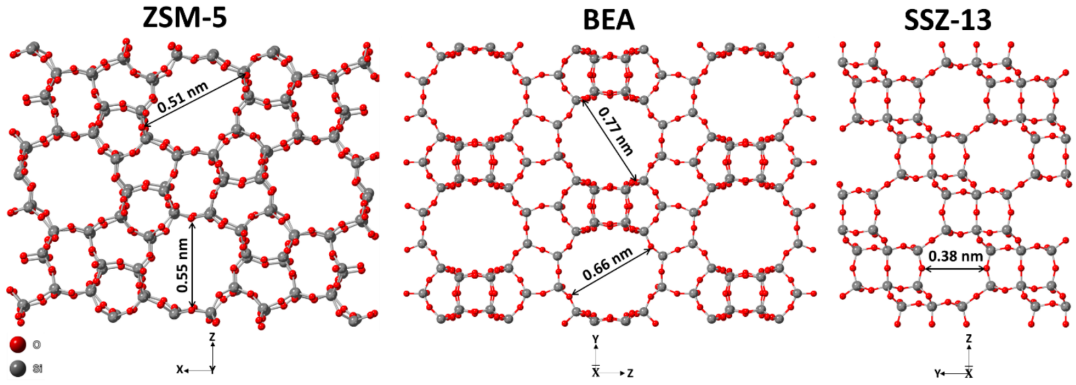

Figure 1.6: Illustration of different frameworks of ZSM-5, Beta-Zeolite (BEA), and SSZ-13 catalysts, highlighting the variance in pore size, and geometry. [45]

A table of commonly used zeolite frameworks can be seen listed in Table 1.6 below, including their pore sizes, typical (SiO_2/Al_2O_3) ratios, and applications.

Framework	Pore Size (Å)	Membered Ring (MR)	Typical (SiO_2/Al_2O_3)	Applications
ZSM-5	~5.4-5.6	10 (Intermediate)	~12-200	Wide range of applications, including MTH
Zeolite A	~4.1	8 (Small)	~1-1.5	Used for gas separation and drying applications
Zeolite Y	~7.4	12 (Large)	~2.5-6	Used in catalytic cracking applications
Beta Zeolite (BEA)	~6.6-7.7	12 (Large)	~25-300	Wide range of applications, including petrochemical production
SAPO-34	~3.8	8 (Small)	~0.5	Light olefin production, MTO
SSZ-13	~3.8	8 (Small)	~10-30	Light olefin production, MTO, NOx reduction

Table 1.6: Comparison of commonly used zeolite frameworks [44] [46] [47].

For jet fuel applications, the goal is to selectively produce C_8-C_{16} HCs with appropriate branching and aromatic content to match the properties of conventional jet fuel. The pore size of the framework thus has to be large enough to accommodate the molecule size of jet fuel, while tailoring the acidity of the framework to favor the formation of branched and cyclic HCs, while maintaining low coke formation and undesired light gases.

Catalyst Acidity

The acidity of the catalysts plays an important role in promoting various reactions, as previously mentioned. However, depending on the desired products, either BAS or LAS can be desired. The zeolite's acidity is often related to the amount of aluminum present in the zeolite, where higher amounts of aluminum result in lower SiO_2/Al_2O_3 ratios. Depending on the purpose of the catalyst, its SiO_2/Al_2O_3 ratio can be tailored to have a specific ratio. Low SiO_2/Al_2O_3 ratios favor the aromatic cycle, increasing the yield of aromatic compounds, while higher SiO_2/Al_2O_3 ratios favor the olefinic cycle, increasing yields of olefinic compounds. Higher acidity is also accompanied by higher activity, increasing the number and thus the kinetics of reactions occurring, resulting in increased coke formation, which heavily influences the lifetime of the catalysts. [41] [44]
While the amount of acid sites plays a major role in selectivity of the products, the location and strength of the acid sites also play a significant role. By having strong

and stable acid sites in the zeolite, destructive effects, such as leaching, can be avoided. Leaching of the acid sites leads to reduced catalytic performance and irreversible catalyst deactivation.

Metal Loading

Base zeolites often have a set framework based on the SiO_2/Al_2O_3 ratio, giving them a certain amount of BAS. However, often a certain amount of BAS is desired to promote either the olefinic or aromatic cycle and specific reaction mechanisms. To change the selectivity of a base zeolite, the framework can be altered through post-synthetic modifications by the deposition of metal ions onto the zeolite. The deposition can be achieved through different methods, one of which includes wet metal impregnation. Depending on the characteristics of the deposited metal ions, different reactions will be promoted. Apart from the additional reactions promoted by the active metal ions, the acidity of the zeolite can also be affected, influencing the amount or strength of BAS and LAS. This can happen through metal impregnation of, e.g., earth alkaline metals, which attach to the BAS and provide new properties to the zeolite.

Metal impregnation can often remove the majority of the BAS of a zeolite, as metal ions can neutralize acid sites or replace protons in BAS during exchange. However, this can be beneficial due to some metals' unique properties that promote certain reaction types. Studies have shown that, when impregnating metals such as calcium and vanadium, a 10-fold reduction in BAS can occur under the correct conditions. This reduction in BAS suppresses the catalyst's hydrogen transfer properties, reducing the selectivity towards cyclization reactions and paraffin production by shifting the acidity towards the olefinic cycle, increasing the yield of olefins [48]. However, introducing metals to the zeolite catalyst does not always reduce the amount of BAS, but it can also introduce more BAS to the catalyst and more LAS.

Depending on the active metals and their loadings, additional deactivation mechanisms can be introduced, further influencing the deactivation and longevity of the catalysts. First of all, the metal can increase the selectivity towards reactions forming compounds that are more susceptible to polymerization and coking. Secondly, excessive metal loading, or simply long operation time, can result in metal agglomeration, where metal nanoparticles sinter, decreasing the active surface area, irreversibly deactivating the catalyst. Furthermore, depending on the activity of the metal, specific molecules or ions can bind to the active site, effectively deactivating it irreversibly [49]. However, metal loading can also increase the lifetime of the catalyst by primarily increasing the selectivity towards the hydrogenation reaction of coke precursors, or by simply tailoring the reaction pathway away from the formation of coke-prone intermediates.

Deactivation and Regeneration

Catalyst deactivation is a common and unavoidable challenge in MTH processes. In these processes, unwanted products like polyaromatics are slowly formed, with a higher boiling temperature than that of the process. This results in coke deposits on the catalyst, which occupy the active acid sites, slowing the reactions and deactivating the catalyst.

Unlike irreversible deactivation mechanisms such as leaching or mechanical degradation, e.g., crushing or metal agglomeration, coke formation is reversible. This allows for catalyst regeneration, achieved through oxidative treatments that burn off coke deposits. Regeneration is a well-established industrial practice, especially in fuel refining, and is essential for maintaining catalyst longevity and economic viability in large-scale eSAF production. Depending on the nature of the coke species formed, the required temperature for complete regeneration will differ.

1.5 Current Challenges and Opportunities for Methanol-to-Jet Implementation

As discussed in Sections 1.2.2 and 1.3.1, the commercialization of MTJ fuel faces several technical and economic barriers. These include the high production cost of eSAF due to the high energy requirements, limitations in chemical composition affecting possible blend ratios and the yield of jet fuel, and the need for stable, long-lasting catalysts. Companies such as Metafuels, Vertimass, and European Energy are all currently working on the *methanol to sustainable aviation fuel* (MeSAF) project, which aims to commercialize the production of e-fuels to the aviation industry. However, each part in the MeSAF project is experiencing challenges that need to be addressed before the commercialization stage can progress towards a point of influence, including both political, economic, and the aforementioned technical challenges [50].

A critical factor influencing both the feasibility and sustainability of eSAF production is the source and handling of CO_2. Ørsteds Kalundborg CO_2 Hub is a *carbon capture and storage* (CCS) project that contributes to national climate goals by capturing and permanently storing 280.000 tonnes of biogenic CO_2 annually from the flue gas of the Asnæs *Combined Heat and Power* (CHP) plant, and 150.000 tonnes from Avedøre Power Station. While effective for emissions reduction, such CCS initiatives also eliminate the opportunity to utilize CO_2 as a feedstock for eSAF production [51]. However, by directly using the captured CO_2, the costs and emissions associated with the liquefaction required for storage of CO_2 and transport are avoided. Thus, locating CC, H_2 production, methanol synthesis, and MTJ conversion at a single site allows for energy and heat integration and eliminates the need for storing and transporting in-

termediate products. This enables substantial energy and emission savings, associated with transport and storage, reducing the overall cost and carbon footprint of the eSAF production. This will inevitably drive down the prices of eSAF, making it more commercially desirable.

This study will aim to model the entire MTJ process chain, from CO_2 capture of flue gas from Asnæs CHP plant, and green H_2 production, to the methanol synthesis and MTH conversion process. The aim is to evaluate the overall efficiency of MTJ fuel production within a fully integrated, co-located system, assessing each stage from CC and H_2 production to the final jet fuel output.

Chapter 2

Objective

The conversion of e-Methanol towards electro-sustainable aviation fuels (eSAF) shows great promise for decarbonizing the aviation sector, due to its unlimited potential. However, due to the high energy requirements associated with eSAF production and low well-to-wake efficiencies, further energy optimization is required to drive commercialization of the technology forward. Furthermore, the complex dynamics of catalyst properties create challenges regarding chemical selectivity, stability, longevity, and yields. To overcome these challenges, catalytic modifications are required to increase the catalyst performance in a methanol-to-jet (MTJ) process.

How can catalyst design and process integration be optimized to enhance the performance, selectivity, and energy efficiency of a continuous single-stage MTJ process for eSAF production from wet methanol?

In addition to this, this thesis aims to answer the following research questions:

- How do different zeolite-based catalyst modifications affect the chemical selectivity, liquid yield, stability, deactivation, and operational lifetime of the MTJ process?
- How can empirical data from the experimental evaluation of zeolite-based catalysts be used to tune an MTH model of the eSAF production chain, for the assessment of performance parameters?
- How does thermal integration of CO_2 capture, H_2 production, methanol synthesis, methanol-to-hydrocarbon, and catalyst selection impact the efficiency of an eSAF production system?

Chapter 3

Methodology

Throughout Chapter 1, different pathways towards producing SAF were presented. Lack of technological development showcased that eSAF is yet to be commercialized, but it has unlimited potential. The following chapters propose a possible pathway for eSAF to push the technological development forward by using relevant theory to model the CC process via amine-based chemical absorption, green hydrogen production through *alkaline water electrolysis* (AWE), and e-methanol synthesis based on the captured CO_2 and produced H_2. Building on the theoretical foundation presented, this study develops corresponding process models to evaluate the potential energy savings achievable through co-location and heat integration of all MTJ-related processes, via pinch analysis. By simulating the full system, from CO_2 capture and green hydrogen production to methanol synthesis and the MTH conversion, the study aims to assess the overall carbon efficiency (η_C) and hydrogen efficiency (η_H). These metrics will quantify how much of the captured CO_2 and supplied hydrogen are retained in the final jet fuel product, and where losses occur throughout the process chain. Moreover, the hydrogen efficiency and internal energy requirements for each process will be used to assess the *energetic jet fuel efficiency* (EJFE), and the total system efficiency η_{Tot}.

Due to the complex reaction dynamics and variability in catalyst selectivity associated with the MTH process, the MTH model must be developed based on empirically gathered experimental data. Further research and development are required to identify catalysts capable of delivering a consistent and stable yield of high-quality HCs, particularly within the jet fuel range, further motivating the experimental research.
To support this, experiments will be conducted using wet, undistilled methanol, representative of the output from the e-methanol synthesis model, as feedstock for conversion over various zeolite-based catalysts. These experiments aim to evaluate catalyst selectivity and product yield, with a focus on HCs in the kerosene range. *Gas chromatographymass spectrometry* (GC-MS) and simulated distillation (SimDist) will be used to identify key product components and establish distillation profiles. These data will inform the selection of representative compounds for input into the MTH model for the different catalysts.
Additionally, temperature measurements during the experiments will be used to estimate the MTH process's exothermicity and heat generation, providing insight into each catalyst's potential for heat recovery. Furthermore, catalyst lifetime and deactivation due to coke formation will be assessed through *thermogravimetric analysis* (TGA), but due to steady-state assumptions, they will not be directly used within the model. A simplified illustration of the overall model can be seen in Figure 3.1.

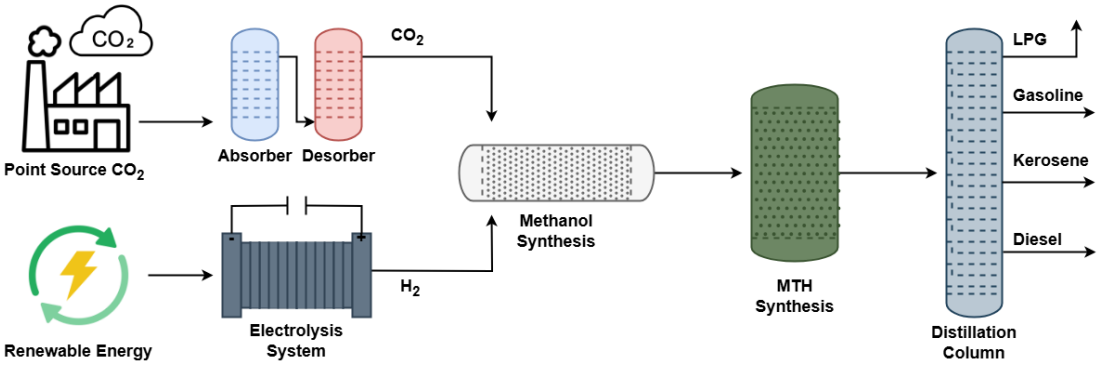

Figure 3.1: Simplified topology of eSAF production utilizing the methanol pathway. Electrolysis, CC process, and methanol synthesis are modeled based on available theory, while the MTH synthesis and distillation are based on conducted experiments.

Chapter 4

Modeling

Understanding the production pathway and energy requirements associated with MTJ, a comprehensive system model has been developed, with the aim of investigating the potential energy savings that co-locating could entail. This chapter thus delves into the theory and modeling of the theoretically based models, consisting of amine-based CC of the fluegas from Asnæs CHP, green hydrogen production from AWE and e-methanol synthesis from the captured CO_2 and the produced H_2.

4.1 Flue Gas Estimation from Asnæs Power Plant for Carbon Capture Modeling

To model CC and determine the best technology for flue gas from the Asnæs power plant, it is essential to estimate the flue gas composition produced during the biomass. The Asnæs Power Plant utilizes wood chips from waste wood as feedstock in a CHP cycle [51]. To ensure complete combustion and minimize the formation of carbon monoxide and other incomplete combustion products, the plant operates under over-stoichiometric conditions. An excess air ratio of $\lambda = 1.3$ is assumed, consistent with values recommended by the Danish Energy Agency for CHP performance assessments [52].

The combustion process is modeled using the elemental composition of the wood chips, sourced from the Phyllis2 database [53]. The selected biomass to represent the waste wood chips consists of dry pine wood chips with bark, excluding ash content, as particulate matter is assumed to be removed via filtration [54]. The elemental composition of the woodchip is summarized in Table B.1.

	Carbon	**Hydrogen**	**Oxygen**	**Nitrogen**	**Sulfur**
Wood chip	50.50 wt.%	6.10 wt.%	42.93 wt.%	0.20 wt.%	0.03 wt.%

Table 4.1: Chemical composition of wet pine wood chip containing bark, used for the calculation of the flue gas [54].

Normalizing the wood chip composition to 1 mol of carbon, the reaction of the over-stoichiometric combustion can be seen in Reaction (R. 4.1).

$$C_{1.0}H_{1.44}O_{0.64}N_{0.0034}S_{0.00022} + 1.56\ (O_2 + 3.76\ N_2) \rightarrow CO_2 + 0.72\ H_2O + 0.0002225\ SO_2 + 5.87\ N_2 + 0.52\ O_2 \quad \text{(R. 4.1)}$$

The flue gas produced by burning pinewood chips with bark with 30% excess air, sim-

ulating the flue gas directly from the boiler, can be seen in Table B.1 in Appendix B alongside all the following calculations. However, depending on the flue gas temperature, water vapor may condense once the saturation pressure is reached, assuming the gas is fully saturated with water vapor. Additionally, while sulfur compounds in flue gas are typically removed using desulfurization units, the very low sulfur content in wood chips allows for the assumption that any sulfurous components in the flue gas can be neglected.

The temperature of the flue gas exiting the steam boiler is estimated to be approximately 130 °C. However, large CHP systems typically utilize flue gas condensation heat exchangers to enhance district heating efficiency, cooling the flue gas to around 50 °C. Furthermore, to maximize the heat recovery of the CHP system, additional absorption heat pumps are employed to reduce the temperature even further to approximately 30 °C, at which point the majority of the water vapor condenses out [55]. The final flue gas stream, suitable for CC, is thus characterized by the following thermodynamic conditions and chemical composition seen in Table 4.2.

Parameter	**Pine Wood Chips**
Temperature [°C]	30
Pressure [bar]	1.01325
Composition [wt.%]	
H_2O	2.50
O_2	4.96
N_2	70.71
CO_2	21.82

Table 4.2: Conditions and composition of the flue gas for carbon capture.

Based on the final flue gas composition and a state-of-the-art evaluation of various CC technologies presented in Appendix A, chemical absorption using monoethanolamine (MEA) has been selected for modeling. This decision is supported by MEAs technological maturity and widespread application in post-combustion CC systems. [56]

4.2 Chemical Absorption Carbon Capture with MEA

Chemical adsorption utilizes an adsorption tower and a stripper tower, alongside auxiliary components, to exchange heat and control the flow within the system. A schematic of an absorption-based CC system can be seen in Figure 4.1.

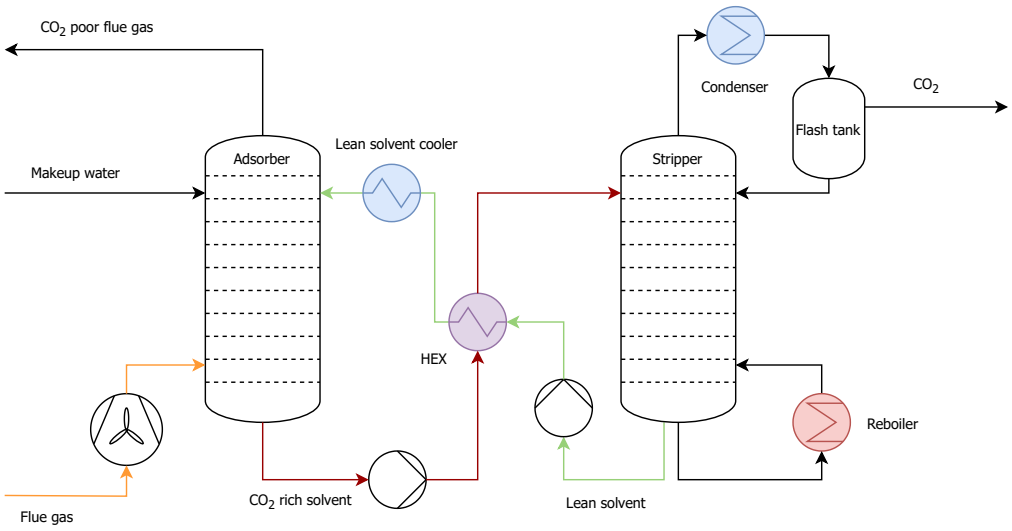

Figure 4.1: Schematic of adsorption-based carbon capture system.

Flue gas, typically from post-combustion processes, enters the bottom of a packed adsorber or tray column at atmospheric pressure and 40-60 °C. If the flue gas is hotter than the selected column temperature, a cooler can be placed before it enters the column. The flue gas containing CO_2 will flow upwards from the bottom of the column counter-current to the flow of lean solvent entering at the top of the column. Makeup water is typically added to the top of the absorber to account for water loss in the CO_2 poor flue gas. The gaseous CO_2 then interacts with an aqueous MEA solution containing 7-35 wt.% MEA. to form aqueous carbamate ($MEACOO^-$) and bicarbonate (HCO_3^-) through various exothermic intermediate reactions. The main reaction of CO_2 into carbamate can be seen in Reaction (R. 4.3). [57] [58]

$$2MEA + CO_2 \rightleftharpoons MEAH^+ + MEACOO^- \qquad \Delta H^0 \approx -2MJ/kg_{CO_2} \qquad \text{(R. 4.2)}$$

The CO_2 rich solvent is extracted at the bottom of the absorber and transferred to the top column of the stripper, also called desorber, through a compressor to increase the pressure to roughly 2 bars and a heat exchanger to heat the stream to 100-120°C. In the stripper, chemical equilibrium between gasoues CO_2 and the aqueous carbamate and bicarbonate shifts, and the CO_2 is released in the reverse endothermic reaction. A reboiler is used to reheat the cooled solvent from the endothermic reactions and increase the amount of CO_2 desorbed. The now gaseous CO_2 leaves the top of the stripper column, and water trapped within the gaseous gas is condensed and separated in the condenser and flash tank, respectively. Depending on the application for the CO_2 it can be compressed or further purified to remove any impurities from the flue gas or additional moisture. Additionally, makeup solvent can be added to the absorber to

account for thermal degradation due to high temperatures within the stripper and the oxidative degradation due to O_2 from the flue gas reacting with the MEA. Some solvent will also be lost in flue gases leaving the absorber, as MEA is highly volatile; however, due to the toxic nature of MEA, its emission is heavily regulated and often removed before it is released. [59] [56] [60]

4.3 Modeling of MEA-based Carbon Capture

To evaluate the energy requirements associated with renewable CO_2 production, a post-combustion CC model has been made in Aspen Plus, utilizing the *equation of state*(EOS) *electrolyte non-random two liquid* (ELECNRTL) method to determine the chemistry and ionic species. The model consists of an equilibrium steady-state amine-based carbon capture, utilizing an aqueous solution of MEA with a capacity of capturing 280.000 tons of CO_2 yearly, and a flue gas composition of combustion pine wood chips including bark. This mimics the conditions of the CC facility to be used for CCS at Ansæs Power Plant and will be used as the baseline for all model cases.

4.3.1 Conditions and Limitations of Selected Conditions

Steady-State

It has been chosen to model the CC system in steady-state and equilibrium conditions. Steady-state conditions have been assumed as dynamic conditions are unavailable and would greatly increase the complexity of the system, which is not required for the calculation of thermal integration. However, this also neglects the varying flow rates of flue gas depending on the hourly heat and power demand, which the power plant would have to follow.

Equilibrium and Rate-based Modeling

Equilibrium conditions have been assumed for both the absorber and desorber columns. This means vapor and liquid phases are considered to be in thermodynamic and chemical equilibrium at each theoretical stage. While rate-based modeling offers more detailed insight by accounting for reaction kinetics and mass transfer, useful for dynamic control and economic assessments, it also increases model complexity and computational demand.
Given the focus on energy optimization and thermal integration in MTJ production, equilibrium modeling is considered sufficient. It is acknowledged that this may slightly overestimate CO_2 capture efficiency and underestimate reboiler duty, but these effects can be mitigated by applying stage efficiency corrections [61] [62].

4.3.2 Overall Model Description

The overall system can be seen in Figure 4.2

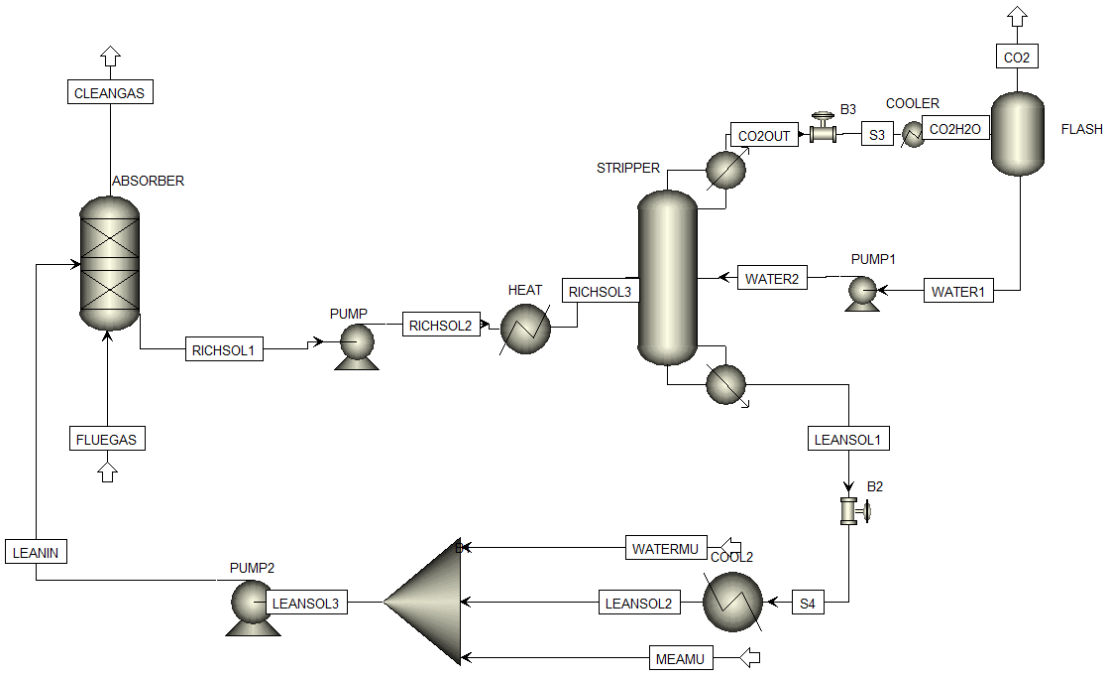

Figure 4.2: MEA amine-based carbon capture in Aspen Plus.

The flue gas (FLUEGAS) from the combustion of bark containing pine wood chips enters the bottom of the absorber at atmospheric pressure and 30 °C due to flue gas condensation, as summarized in table 4.2 [55]. The lean solvent (LEANIN) enters the top of the absorber where the reactions between CO_2 and MEA occur, and the CO_2 gets chemically absorbed under atmospheric pressure. The CO_2 poor flue gas (CLEANGAS) leaves the top of the absorber, carrying some water and MEA. The CO_2 rich solvent (RICHSOL) leaves the bottom of the absorber, from where it is pumped to 1.8 bars and heated to 107 °C, before it enters the top of the stripper, in which the CO_2 is desorbed. The desorbed CO_2 (CO2OUT) contains water and leaves the top of the stripper. To separate the water, it enters a valve, where it is depressurized to atmospheric pressure before it enters the condenser and is cooled to 25 °C and separated in a flash tank, leaving the pure CO_2 (CO2). The water (WATER1) is pressurized again to 1.8 bar before it enters the top of the stripper. Lean solvent (LEANSOL1) enters a valve to depressurize to atmospheric pressure and is cooled to 40 °C. Makeup MEA and water are added to uphold the mass balance and to account for any losses in the (CLEANGAS) and (CO2) stream. The thermal properties of all components can be seen in Table 4.3.

Name	Component	Temperature [°C]	Pressure [bar]
Abosorber	RadFrac	N/A	1.01325
Pump	Pump	N/A	1.8
Heat	Heater	107	1.8
Stripper	RadFrac	N/A	1.8
B3	Valve	N/A	1.01325
Cooler	Heater	25	1.01325
Flash	Flash2	25	1.01325
Pump1	Pump	25	1.8
B2	Valve	N/A	1.01325
Cool2	Heater	40	1.01325
Mixer	Mixer	N/A	1.01325
Pump2	Pump	N/A	1.01325

Table 4.3: Thermal properties of components used within the model

Water and Solvent loss

As the CO_2 gets absorbed in the absorber and desorbed in the stripper, the clean gas exiting the absorber will be CO_2 poor, and the CO_2 stream leaving the stripper will be CO_2 rich. However, some water and MEA will also leave the system. This is governed by Raoult's law, as seen in Equation (4.1):

$$p_i = x_i p^*_{i,vapor} \tag{4.1}$$

where p_i is the partial pressure of component i, while $p^*_{i,vapor}$ is the equilibrium vapor pressure of the component and x_i is the mole fraction of the component in the liquid phase. Combined with Dalton's law, which states that the sum of partial pressures of each component in a mixture must add up to the total pressure, the mole fraction of water, or MEA in the leaving streams is found:

$$y_i = \frac{p^*_{i,vapor}}{P_{total}} \tag{4.2}$$

Due to this, some solvent will invariably exit the system through the clean flue gas stream and the CO_2 leaving the system. Most of the solvent leaving with the clean CO_2 stream in the stripper is recovered by the flash tank, due to the lower vapor pressure at lower temperatures and lower partial pressures obtained through cooling and depressurization of the stream. The recovered solvent is then recirculated to the stripper column. Thus, most of the solvent is expected to leave the system through the clean gas stream exiting the absorber. Two makeup streams have been added to account for the lost solvent, entering a lean solvent stream at atmospheric conditions.

4.3.3 Chemical Reactions

The main reversible chemical reactions occurring when CO_2 is absorbed/desorbed into the MEA solution in the absorber/stripper are based on the NRTL electrolyte wizard, and can be seen in (R. 4.3) to (R. 4.7) [63]:

$$MEACOO^- + H_2O \overset{K_1}{\rightleftharpoons} MEA + HCO_3^- \tag{R. 4.3}$$

$$CO_2 + 2H_2O \overset{K_2}{\rightleftharpoons} HCO_3^- + H_3O^+ \tag{R. 4.4}$$

$$HCO_3^- + H_2O \overset{K_3}{\rightleftharpoons} H_3O^+ + CO_3^{2-} \tag{R. 4.5}$$

$$MEAH^+ + H_2O \overset{K_4}{\rightleftharpoons} MEA + H_3O^+ \tag{R. 4.6}$$

$$2H_2O \overset{K_5}{\rightleftharpoons} OH^- + H_3O^+ \tag{R. 4.7}$$

The equilibrium constants K_i are temperature-dependent and determine the concentrations of the reactants and products of each reaction at any given temperature. The chemical equilibrium states that the rates of the forward and backward reactions are in equilibrium, which occurs at the reaction's lowest energy level at a given constant pressure and temperature. This is given by the change in Gibbs free energy, as seen in Equation (4.3).

$$\left(\frac{\delta G}{\delta \zeta}\right)_{T,P} = 0 \tag{4.3}$$

In Aspen Plus, the chemical equilibrium constants for all reactions are calculated from a parameter-based correlation as a function of temperature, as seen in Equation (4.4).

$$\ln(K_{\text{eq}}) = A + \frac{B}{T} + C\ln(T) + DT \tag{4.4}$$

The parameters A, B, C, and D are determined from databases within the library of Aspen Plus, while T is the temperature. If the chemical equilibrium constant $K > 1$ the forward reaction is favored, if $K = 1$ the reaction is in equilibrium, and when $K < 1$, the backward reaction is favored. Higher temperatures tend to shift the equilibrium towards the reactants for exothermic reactions, favoring the endothermic backward reactions, counterbalancing variations. Because of this shift in equilibrium, the exothermic absorption reactions will be favored at lower temperatures, while the endothermic desorption reactions will be favored at higher temperatures.

Physical Absorption

Apart from the chemical absorption of CO_2, small amounts of CO_2 will be dissolved in the water and MEA. This is governed by Henry's law, which describes the solubility of a gaseous compound in a liquid being directly proportional to the partial pressure of CO_2, as seen in Equation (4.5):

$$C_{CO_2} = k_H p_{\mathbf{CO_2}} \tag{4.5}$$

Where C_{CO_2} is the CO_2 concentration dissolved in the solution, k_H is Henry's law constant and dependent on the temperature, and p_{CO_2} is the partial pressure of CO_2.

4.3.4 Absorber Design

The absorber unit consists of a RadFrac with 20 stages, operating at atmospheric conditions, with the lean solvent with a MEA loading of 30 wt.% entering the top of the column and the flue gas entering the bottom of the column. The number of stages is typically determined by the height of the column, where more stages, corresponding to a higher tower, increase the capture efficiency and typically vary between 10-20 stages. Whereas more stages increase the *capital expenses* CAPEX of the column, too few stages risk CO_2, not allowing sufficient time for the CO_2 to get absorbed, decreasing the performance of the absorber [64]. As CAPEX is not explored within this project, 20 stages have been selected for the base case. Likewise, a MEA loading of 30 wt.% has been chosen for the base case, as it is commonly used for similar flue gas compositions [65] [66] [64].

Vapor-Liquid Equilibrium

The Vapor-Liquid Equilibrium (VLE) in Aspen Plus is determined using the ELECNRTL method. This method calculates VLE based on activity coefficients, stoichiometric balances, equilibrium constants, and Henry's Law components. The electrolyte extension of the NRTL model further incorporates electrostatic ion-ion interactions, as well as local interactions at the molecular level, including molecule-molecule and molecule-electrolyte interactions within the MEA-CO_2-H_2O system. These effects are estimated through semi-empirical equations that utilize binary interaction energies, with parameters automatically retrieved from Aspen Plus databases when selecting the ELECNRTL method.

Murhpree Efficiency

To account for deviations between the actual vapor composition on each stage and the ideal vapor composition predicted by equilibrium calculations, a Murphree efficiency

of $\eta_{mv} = 0.25$, as reported by Lars Erik Øi [61], is applied. This adjustment compensates for mass transfer limitations that are not represented in equilibrium-based models, as described by Equation (4.6).

$$\eta_{mv} = \frac{y_{i,j} - y_{i,j+1}}{y^*_{i,j} - y_{i,j+1}} \tag{4.6}$$

where, y is the vapor fraction and i indicates each component and j indicates the stage number, while $*$ indicates phase equilibrium [67].

CO_2 Loading

The CO_2 loading, or just loading, is a common measurement used within amine-based CC and describes the molar ratio of CO_2 absorbed in the solvent as seen in Equation (4.7).

$$\text{Loading} = \frac{y_{CO_2}}{y_{MEA}} = \frac{y_{CO_2} + y_{HCO_3^-} + y_{CO_3^{2-}} + y_{MEACOO^-}}{y_{MEA} + y_{MEAH^+} + y_{MEACOO^-}} \tag{4.7}$$

The numerator includes CO_2 and all the ions, while the denominator includes the MEA and its ions. When the lean solution and CO_2 enter the absorber column, the CO_2 is absorbed in the solvent and leaves as a CO_2 solvent. Typical values for the CO_2 loading in the lean is around 0.15 - 0.30 in the lean stream and 0.4 - 0.5 for the rich stream [68]. The loading in the lean and rich streams gives insight into the system's efficiency. Lower lean loadings allow for more CO_2 absorption in the absorber, increasing the CO_2 absorption efficiency. However, as the absorption of CO_2 is an exothermic reaction, higher absorption increases the temperature, shifting the equilibrium towards desorption, limiting the achievable CO_2 loadings in the rich stream. Additionally, achieving low lean loadings also requires effective desorption in the stripper, which can be energy-intensive. [64]

Liquid-to-Gas ratio

The *liquid-to-gas* ratio (L/G), measured either mass-based or molar-based, describes the ratio between the flow rate of flue gas and the lean solvent into the absorber. Higher L/G ratios result in more solvent in recirculation, increasing the capture efficiency and reducing the need for larger columns. However, more recirculating liquid also requires more energy for desorption at higher temperatures, meaning an optimum exists. The ideal L/G is also dependent on the fluegas composition, with lower CO_2 concentration, a higher flow of gas is required as the driving force of partial pressure difference is lower, and the mass transfer for CO_2 absorption would take a longer time to reach equilibrium. Likewise, for flue gases of higher CO_2 concentrations, the

mass transfer is less of a limiting factor, with more solvent being required to accommodate the CO_2. Lower MEA concentrations thus also require higher L/G ratios. Sources suggest that the ideal L/G ratio can vary from down to 3 kg MEA/kg CO_2, up to 6.5 kg MEA/kg CO_2 for systems of similar flue gas composition and 30 wt.% MEA [64][69]. For the purposes of this project, an initial L/G ratio of 3.76 kg/kg has been used, corresponding to the findings of Paty Muñoz [62].

4.3.5 Stripper Design

The stripper, also called the desorber, desorbs the captured CO_2 by shifting the equilibrium towards the reverse, endothermic reaction. Because of this, the higher temperatures are favorable. This is achieved by increasing stripper pressure to increase the saturation temperature of the rich solvent to where more CO_2 can be desorbed. The pressure is therefore set to the highest value at which the solvent boils without degradation of MEA, at a temperature of 122 °C, as determined by Alie [70]. This corresponds to a pressure of 1.8 bar, to which the rich solvent is pressurized before entering the stripper. Likewise, the solvent is typically heated through a counterflow heat exchanger between the cold rich stream leaving the absorber, and the hot lean stream leaving the stripper, of which higher inlet temperatures increase overall efficiency. For all cases, this is initially simulated by a heater set to 107 °C, corresponding to the findings of Paty Muñoz, also utilizing 30 wt.% MEA, equal operating conditions, and a similar flue gas composition [62]. Identical to the absorber, the stripper consists of 20 stages with the rich solvent entering the bottom of the column and the CO_2 leaving the top of the column, with the water separated from the CO_2 recirculating back into the top of the column. However, no Murphree efficiency was applied to the stripper, as the desorption process exhibits relatively fast kinetics and operates under near steady-state conditions [61].

4.3.6 Results and Discussion

It is standard procedure for new CC facilities to have design goals regarding the efficiency of carbon captured. For those reasons, three cases for the CC model have been made, for a CO_2 capture efficiency of 80%, 85%, and 90%, as defined in Equation (4.8).

$$\eta_{CO_2,\text{capture}} = \frac{\dot{m}_{\mathbf{CO_2,in}}}{\dot{m}_{\mathbf{CO_2,out}}} \cdot 100 \tag{4.8}$$

The different capture efficiencies have been achieved by varying the reboiler duty within the stripper to increase the desorption of CO_2, lowering the CO_2 loading within the lean stream, allowing for more efficient absorption. Otherwise, all simulations' parameters have been constant, with an initial guess L/G ratio of 3.86 [kg/kg], varied until the coverage criteria were met, and a satisfying solution has been found. The key parameters and energy requirements of the results from the model can be seen in

Table 4.4.

		CO_2 Capture Efficiency		
Parameter	Unit	**80%**	**85%**	**90%**
Initial Conditions				
Murphree Efficiency Absorber	[-]	0.25	0.25	0.25
Murphree Efficiency Stripper	[-]	1	1	1
Stages in Absorber Column	[-]	20	20	20
Stages in Stripper Column	[-]	20	20	20
Initial L/G ratio	[kg/kg]	3.86	3.86	3.86
Reboiler Duty	[kW]	23850	26180	28560
Flue gas flow rate	[tonnes/hr]	160	160	160
Flue gas CO_2 flow rate	[tonnes/hr]	34.92	34.92	34.92
Key Parameters				
Recovered CO_2 Flow rate	[tonnes/hr]	27.93	29.68	31.43
Lean CO_2 Loading	[mol CO_2/mol MEA]	0.280	0.264	0.247
Rich CO_2 Loading	[mol CO_2/mol MEA]	0.495	0.493	0.489
L/G ratio	[kg/kg]	4.030	4.011	3.991
CO_2 Purity	[mol%]	96.81	96.82	96.82
Water Makeup	[kg H_2O/ton CO_2]	415.1	407.4	431.2
MEA Makeup	[g MEA/ton CO_2]	763	890	1037
MEA concentration at Absorber outlet	[ppm]	65.9	81.9	101.5
Clean gas temperature	[°C]	45.90	45.56	45.10
Lean Solvent Temperature at Stripper outlet	[°C]	118.3	118.8	119.3
Energy Requirements				
Reboiler Heating Requirement	GJ/tonne CO_2	3.074	3.175	3.272
Pre-Heater Heating Requirement	GJ/tonne CO_2	4.623	4.524	4.394
Pre-Cooler Cooling Requirement	GJ/tonne CO_2	4.857	4.885	4.911
Condenser Cooling Requirement	GJ/tonne CO_2	1.685	1.676	1.667
Electrical Work Requirement	kJ/tonne CO_2	2.135	2.008	1.896

Table 4.4: Key parameters and energy requirements from amine-based carbon capture model.

From the amine-based CC model results at 80%, 85%, and 90% CO_2 capture efficiencies, insights into the trade-offs between energy requirements and capture efficiency have been obtained. With the electrical work required to drive the pumps being insignificant, varying from 2.135 - 1.896 kJ/tonne CO_2, four main energy requirements have been observed: The reboiler heating requirement within the stripper column, pre-heater heating requirement heating the rich solvent to 107C, pre-cooler cooling requirement, cooling the lean solvent down to 40°C, and lastly the condenser cooling requirement, cooling the CO_2/steam stream to 25°C, to separate the water from the CO_2. It is to be noted that the pre-heater and pre-cooler are typically integrated with a heat-exchanger, as previously mentioned. The reboiler duty is typically supplied by

expensive hot steam, while the condenser cooling requirement is typically supplied by relatively inexpensive cooling water. The reboiler duty is therefore the main energy concern for amine-based CC. Expectedly, a clear trend of higher reboiler heating requirements is seen for higher capture rates, varying between 3.074 - 3.272 GJ/ton CO_2 between 80 - 90% CO_2 capture efficiency. This is slightly lower than 3.6 - 4.0 GJ/ton CO_2 for equal MEA concentration and slightly lower CO_2 concentrations, as reported by Bio et al [71]. The higher reboiler duties also correspond to a lower lean CO_2 loading as more CO_2 is desorbed, leading to higher capture efficiencies, as more CO_2 can be absorbed.
Another typical concern regarding amine-based CC is the makeup of solvent and water. Higher MEA and water makeup are also observed for higher capture efficiencies, varying from 763 - 1037 g MEA/tonne CO_2 and 407.4 - 431.2 kg H_2O/ton CO_2. The makeup primarily corresponds to the solvent and water lost in the gas stream leaving the absorber column, in which the MEA slip potentially could pose environmental concerns.

Despite the higher energy costs associated with increased efficiency, the CC model used for this project has been set at a fixed CO_2 capture efficiency of 90%, aligning with the benchmarks set by other studies [64]. Additionally, the CO_2 capture system is scaled to capture 32 tonnes per hour, reflecting Asnæs CHP's goal of capturing 280,000 tonnes annually.

4.4 Green Hydrogen Production

Electrolyzers for green hydrogen production utilize renewable electricity to split H_2O molecules into oxygen and H_2 as seen in the overall water electrolysis Reaction (R. 4.8).

$$H_2O(aq) \rightarrow H_2(g) + \frac{1}{2}O_2(g) \qquad \Delta H^0 = 285 kJ/mol \qquad \text{(R. 4.8)}$$

All electrolyzers work by producing either an ion (OH^- or O^{-2}) or a proton (H^+) through the decomposition of water on an anode electrode, carrying oxidation reactions, and the cathode electrode, carrying reduction reactions, through the supply of voltage. The charged protons/ions are then transferred to the cathode/anode through an electrolyte medium. Depending on the technology, the materials of the electrodes and electrolyte differ.
Three main types of water electrolyzers exist, consisting of *alkaline water electrolyzer* (AWE), *Proton exchange membrane water electrolysis* (PEMWE), and *solid oxide water electrolyzer* (SOWE), and operate at different conditions, utilizing different materials. An overview of the different technologies can be seen in Table 4.5.
AWE and SOWE have primarily been investigated as low- and high-temperature pathways, respectively, for green hydrogen production. Studies by IR Skov and H. Abid

Electrolysis type	AWE	PEMWE	SOWE
Type of electrolyzer	Alkaline	Polymer electrolyte	Solid oxide
Electrolyte	NaOH/KOH	PEM	Ceramic
Electrode	Ni & Ni-Mo alloys	Pt, Pd-Pd, Ir, Ru,	Ni-cermet, ZrO_2
Operating Pressure	1-30 bars	1-300 bars	1-25 bars
Operating Temperature	40-90°C	50-90°C	800-1000°C
System efficiency (HHV)	68-77%	62-77%	89%
Minimum load (% of design capacity)	15-40%, 5% (SOTA)	0-10%	>3%
TRL	Mature TRL 9	Commercial TRL 7-8	R&D TRL 5-7
Capital cost	$800-1000/kW	∼$1400/kW	∼$2000/kW

Table 4.5: Overview of different electrolysis technologies [72] [73] [74].

have conducted multiple case analyses comparing eSAF production from various CO_2 and H_2 sources and different production pathways. Their findings indicated that due to the significantly lower CAPEX cost associated with AWE, it was deemed more cost-effective and economically viable across all scenarios, for both the current technological maturity and projected advancements for eSAF production. Consequently, AWE was selected for this project [75].
A schematic of an AWE system can be seen in Figure 4.3.

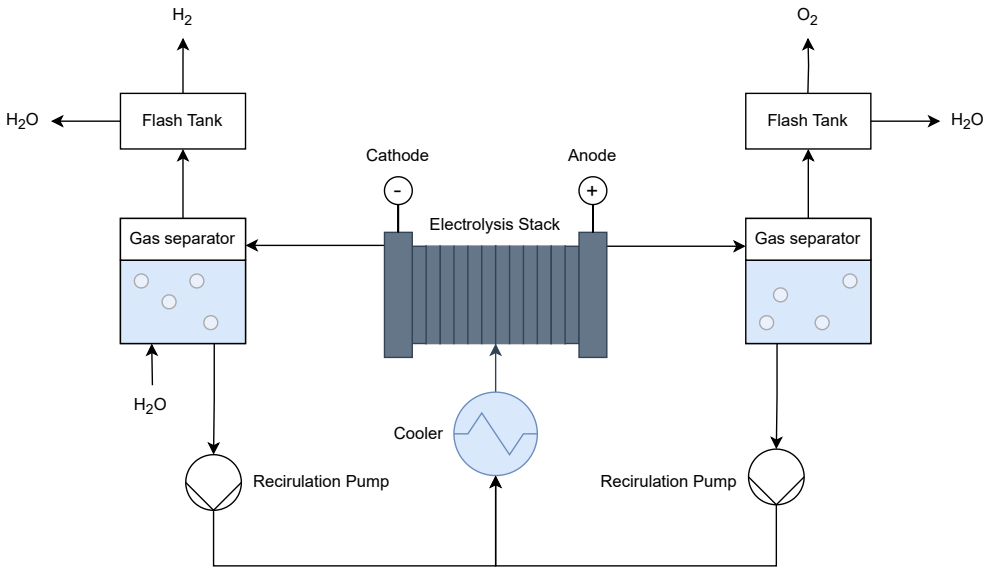

Figure 4.3: Schematic of an Alkaline Water Electrolysis System

The AWE system consists of the electrolyzer stack, carrying the splitting reaction through an alkaline electrolyte medium consisting of an aqueous potassium hydroxide

(KOH) solution. The produced H_2 and O_2 at the cathode and anode are separated, and the electrolyte is recirculated and cooled to maintain a stable operation temperature, from the heat generation of excess power consumption.

4.5 Alkaline Water Electrolysis Model

The AWE model was developed in Aspen Plus with integrated MATLAB calculations for electrochemical and energy/mass balance assessments. The model is based on the findings of Sánchez et al. [76] and scaled to produce 4.398 tonnes/hr of hydrogen, ensuring a 3:1 H_2/CO_2 molar ratio for methanol synthesis. The Aspen Plus simulation of the AWE system is shown in Figure 4.4.

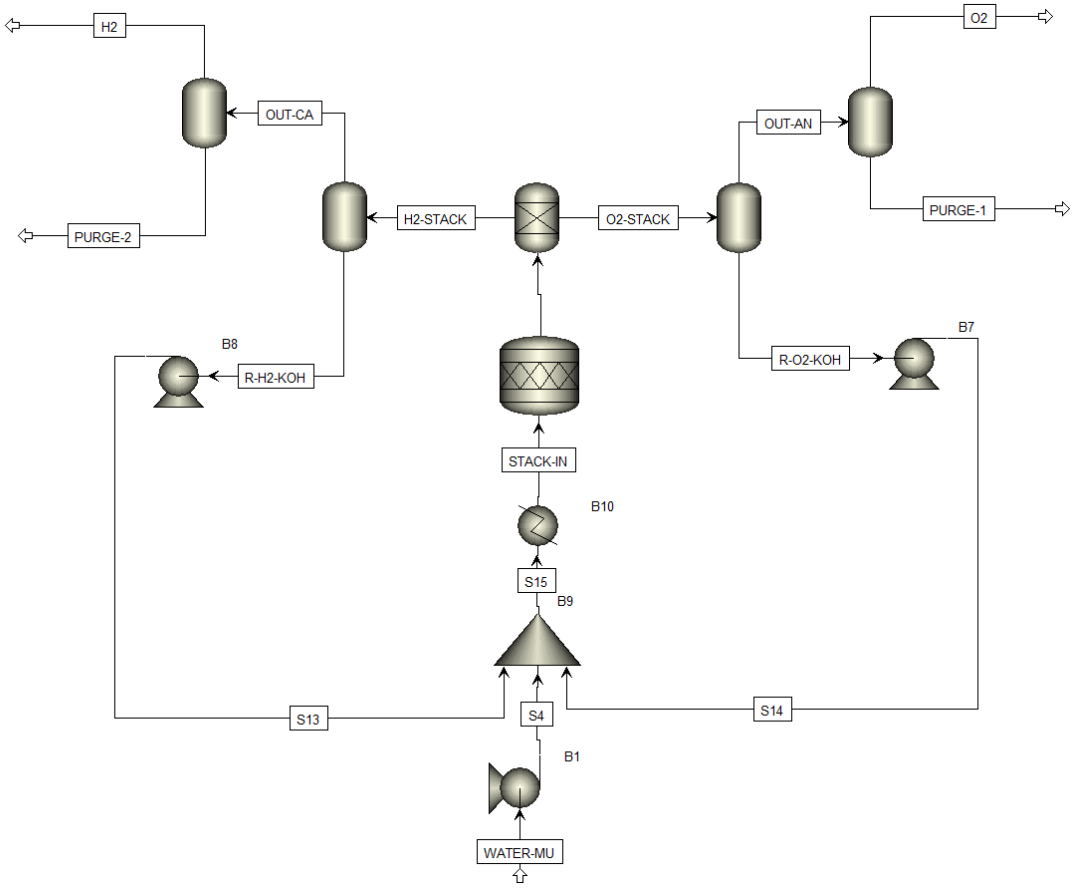

Figure 4.4: Alkaline Water Electrolysis model in Aspen Plus.

4.5.1 Overall Model Description

The electrolyzer stack is represented by an adiabatic steady-state, RSTOIC reactor in Aspen Plus, simulating the electrochemical water splitting reaction seen in Reaction (R. 4.8), utilizing the ELECNRLT method to account for the produced ions, as well as its associated heat duties.
The model separates water into hydrogen (cathode side) and oxygen (anode side) through a component splitter, reflecting Reaction (R. 4.8). Both the H_2-stack and O_2-stack streams leave the reactor in the vapor phase, trapped in the electrolyte, at 35 wt.% KOH aqueous solution.

To simulate the outputs from the cathode and anode, the hydrogen and oxygen are separated from the electrolyte using flash tanks. These tanks operate under conditions similar to the stack, with a pressure corresponding to a 0.3 bar pressure drop in the stack. To increase the gas purity, the hydrogen and oxygen are further separated in a secondary flash unit at 25°C, of which the streams exit with a purity of 99.5 mol.%.
The non-reacted electrolyte, containing the majority of water, is recirculated using pumps from which the water purged from separation in the flash units is re-added as water makeup. The amount of water converted to hydrogen and oxygen is determined based on the mass flow of water in the electrolyte feed and the hydrogen output, experimentally determined by Sánchez et al. [76]. The conversion of water is expressed as seen in Equation (4.9):

$$X_{H_2O} = \frac{n_{H_2,\text{prod}} MW_{\mathbf{H_2O}}}{(1 - c_{KOH})\dot{n}_{\text{stack}}} \tag{4.9}$$

This results in a low conversion rate of water, corresponding to large recirculating flows. The large recirculating flows are advantageous in quickly transferring the gas bubbles, minimizing the temperature increase from the exothermic splitting in the stack, resulting in more stable operation. The primary operating conditions of the AWE model are summarized in Table 4.6.

Parameter	**Value**	**Unit**
Stack Operation Temperature, T_{stack}	75	[°C]
Stack Operation Pressure, P_{stack}	7	[bar]
Electrolyte Concentration, c_{KOH}	35	[wt.%]
Cell Number, N	300	[-]
Current Density, i	4200	[A/m^2]
H_2O Conversion, X_{H_2O}	2.73x10^{-3}	[-]

Table 4.6: Operation conditions of the Alkaline Water Electrolysis model used for Hydrogen production [76]

The number of cells determines the stack voltage and is chosen based on typical con-

figurations in high-power commercial AWE systems [77]. To meet the required hydrogen output, the electrolyte flow rate and electrode area are scaled in accordance with electrochemical and energy/mass balance calculations performed in MATLAB, as described in the following sections.

4.5.2 Electrochemical Modeling Equations

To estimate the required energy input and size of the electrolyzer stack for the desired hydrogen output, the following electrochemical modeling equations have been calculated. As per Ohm's law, the electrical work of the stack is the product of the voltage and the current. The voltage of the stack is determined from the voltage of each individual cell and the number of cells connected in series, while the current is determined from the area of cells in parallel. The voltage of a single cell is determined from the reversible cell voltage, also called Nernst potential, and energy losses within the electrolyzer, commonly referred to as overpotentials, as seen in the following Equation (4.10):

$$V_{\text{cell}} = V_{\text{rev}} + (\hat{\eta}_{\text{act}} + \hat{\eta}_{\text{ohm}} + \hat{\eta}_{\text{conc}}) \tag{4.10}$$

where V_{rev} is the Nernst potential, describing the minimum theoretical voltage required to split water into hydrogen and oxygen under ideal conditions, assuming no energy losses. At standard conditions, the Nernst potential is equal to V_{rev} = 1.23 V for water splitting, as determined from the change in Gibbs free energy of the reaction. $\hat{\eta}_{\text{act}}, \hat{\eta}_{\text{act}}$ and $\hat{\eta}_{\text{conc}}$ are the activation, ohmic and concentration overpotentials, relating to physical limitations within the electrolyzer stack regarding reaction kinetics, electron resistance and mass transfer respectively. These resistances are typically measured and determined experimentally utilizing polarization curves, for which a semi-empirical equation can be used. The actual cell voltage can therefore be determined by Equation (4.11), with parameter values as seen in Table C.1 in Appendix C.

$$V_{\mathbf{cell}} = V_{\mathbf{rev}} + [(r_1 + d_1) + r_2 T + d_2 P]\, i + s\log\left[\left(t_1 + \frac{t_2}{T} + \frac{t_3}{T^2}\right) i + 1\right] \tag{4.11}$$

where T, P, and i are the stack temperature, pressure, and current density, respectively. Similar to the actual cell voltage, the actual current required to produce a mole of H_2 is determined by Faraday's efficiency, describing the ratio between the theoretical maximum and the actual hydrogen production. This is seen in Equation (4.12),

$$\eta_F = \frac{n_{\text{H}_2,\text{prod}}}{n_{\text{H}_2,\text{th}}} \tag{4.12}$$

where $n_{\text{H}_2,\text{prod}}$ is the actual measured hydrogen production and $n_{\mathbf{H_2,th}}$ is the theoretical maximum determined from the thermoneutral voltage, described by Faraday's law

and the reaction enthalpy, as described by Equation (4.13).

$$V_{\text{tn}} = \frac{\Delta H}{zF} \tag{4.13}$$

where F is Faraday's constant and z is the number of electrons transferred per mole of water, and is equal to 2. The thermoneutral voltage describes the minimum voltage required for water electrolysis at adiabatic conditions and equals V_{tn} = 1.48, at standard conditions. The Faraday efficiency has also been determined experimentally and follows the semi-empirical Equation (4.14), with parameter values seen in Table C.1 in Appendix C. [76]

$$\eta_F = \left(\frac{i^2}{f_{11} + f_{12}T + i^2} \right) (f_{21} + f_{22}T) \tag{4.14}$$

Faraday's efficiency can then be combined with Faraday's law to calculate the actual hydrogen production, as seen in Equation (4.15).

$$n_{\text{H}_2,\text{prod}} = \eta_F \frac{iA_{\text{cell}}}{zF} N \tag{4.15}$$

From the element balance of the overall electrolysis splitting reaction (4.11), oxygen production must be half the production of hydrogen:

$$n_{\text{O}_2,\text{prod}} = \frac{1}{2} n_{\text{H}_2,\text{prod}}$$

In physical electrolysis systems, small amounts of hydrogen will travel from the cathode to the oxygen in the anode and vice versa, in a process known as hydrogen crossover. This is highly undesirable due to the explosive safety hazards of mixing H_2 and O_2. However, for the purposes of this project, any hydrogen crossover is neglected.

Energy Balances

The total energy demand for hydrogen electrolysis is given by the enthalpy of reaction, as described in Equation (4.16).

$$\Delta H = \Delta G + T\Delta S \tag{4.16}$$

With all the energy required for water electrolysis supplied by electricity, the thermoneutral voltage describes the minimum voltage for driving the water splitting reaction; any additional energy applied to the system is converted to heat. The heat generation can thus be determined from the difference between the cell and thermoneutral voltage, as described by Equation (4.17).

$$Q_{\text{gen}} = N \cdot iA_{\text{cell}}(V_{\text{cell}} - V_{\text{tn}}) \tag{4.17}$$

Any heat losses within the system are neglected; therefore, to maintain a steady operation temperature, the generated heat must be removed from the system by cooling the recirculating stream. The efficiency of the electrolyser system can thereby be determined by the total electrical power input compared to the chemical power output of the hydrogen, as described by Equation (4.19).

$$\eta_{\text{AWE}} = \frac{n_{\text{H}_2,\text{out}}\text{LHV}_{H_2}}{W_{\text{Net}}} \tag{4.18}$$

where LHV_{H_2} is the lower heating value of hydrogen and W_{Net} is the total electrical work required for the system. The lower heating value has been used to represent the usable energy of hydrogen better, as the higher heating value includes the energy used to condense water vapor formed during combustion, which will not be the case during methanol synthesis. The total electricity work of the system is determined from the energy required in the stack and the pumps for recirculation and water makeup, as described in Equation (4.19).

$$W_{\text{net}} = W_{\text{stack}} + W_{\text{pump,R1}} + W_{\text{pump,R2}} + W_{\text{pump,H}_2\text{O}} \tag{4.19}$$

The electric power input W_{stack} to the electrolysis stack is determined by the required voltage and current, as described in Equation (4.20).

$$W_{\text{stack}} = V_{\text{stack}} I = (V_{\text{cell}} N)(i A_{\text{cell}}) \tag{4.20}$$

The electrochemical model and associated energy balances can estimate the total energy requirements for the upscaled AWE system, as presented in Table 4.7.

4.5.3 Results and Discussion

Summary of Scaled Alkaline Water Electrolysis System		
Parameter	**Value**	**Unit**
Key Parameters		
Mass Hydrogen Output $\dot{m}_{H_2,out}$	4.398	[tonne/hr]
Molar Hydrogen Output $\dot{n}_{H_2,out}$	2.181	[kmol/hr]
Electrolyte Recirurlation Flow, $\dot{m}_r$	22151.5	[tonne/hr]
Cell Voltage, V_{cell}	2.02	[V]
Electrode Area, A_{cell}	255.4	[m^2]
AWE System Efficiency η_{AWE}	58.8	[%]
Energy Requirements		
Recirculation Cooler Duty, Q_{cooler}	-75.0	[MW]
Cathode Flash Duty, Q_{Cat}	-1.62	[MW]
Anode Flash Duty, Q_{Stack}	-0.84	[MW]
Stack Electrical Work, W_{Stack}	292.2	[MW]
Recirculation Pump Electrical Work 1, W_{Stack}	0.10	[MW]
Recirculation Pump Electrical Work 2, W_{Stack}	0.10	[MW]
Water-makeup Pump Electrical Work, W_{Stack}	0.0098	[MW]

Table 4.7: Key parameters and energy requirements from alkaline water electrolysis model.

Hydrogen production via electrolysis is inherently energy-intensive, with the majority of energy consumption stemming from the electrical work required for water splitting. In this model, the scaled AWE system produces 4.398 tonnes of hydrogen per hour, corresponding to the 3:1 H_2/CO_2 molar ratio required for e-methanol synthesis, and an overall system efficiency of 58.8%. The total stack power requirement reaches 292.2 MW, highlighting the importance of integrating such systems with surplus renewable electricity to reduce operating costs and emissions as seen in commercial electrolysis systems [78] [79].

Despite the substantial electrolyte recirculation flow rate of over 22000 tonnes per hour, the associated pumping power remains negligible, accounting for less than 0.1% of the total electrical load. This indicates that most of the energy input is dedicated to the electrochemical reaction rather than fluid transport.

The significant cooling duty of 75 MW is required to regulate the temperature of the recirculating electrolyte, ensuring stable operation around 75 °C. This cooling removes the excess heat generated by the stack due to ohmic losses and overpotential effects. Additional thermal duties from the cathode and anode flash stages are relatively small in comparison.

Understanding the power demand and heat removal of the AWE system is critical, as these factors directly impact the overall efficiency of eSAF production. The heat generated by the electrolysis stack will be recovered and integrated into the broader process, as discussed in Chapter 8. This thermal integration is essential for improving the thermal efficiency of the MTJ process.

4.6 e-Methanol Synthesis Model

The methanol is synthesized utilizing the captured CO_2 from the MEA-based CC process described in Section 4.3 and green hydrogen from the AWE model described in Section 4.5, to form the basis of the e-methanol utilized in the MTH process.
Traditional methanol synthesis typically uses a mixture of syngas derived from gasification processes of fossil fuels and operates at moderate pressures of 30-100 bar and temperatures around 200-300 °C, utilizing heterogeneous catalysts to increase the rate of reaction [80] [81]. In contrast, production of e-methanol avoids the usage of syngas by directly converting renewable CO_2 and H_2 into methanol, in a process similar to the one seen in Figure 4.5.

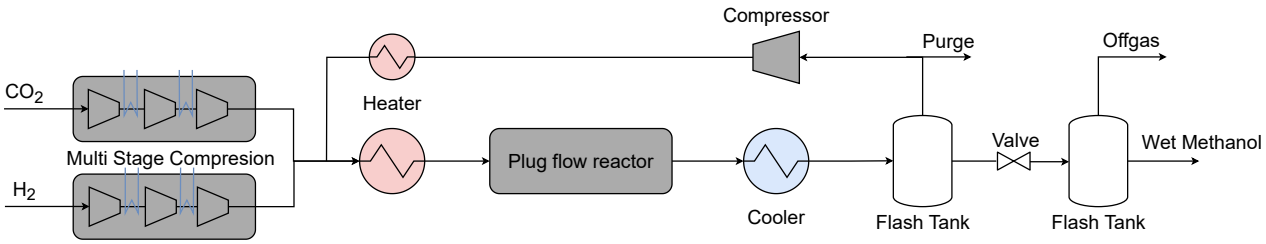

Figure 4.5: Schematic of an e-methanol production system

Due to the presence of CO in conventional methanol synthesis, the requirement for water is increased to convert CO to CO_2 through *water-gas-shift* (WGS) reaction. This conversion is described by Reaction (R 4.9).

$$CO + H_2O \rightleftharpoons CO_2 + H_2 \qquad \Delta H^0 = -41\,kJ/mol \qquad \text{(R 4.9)}$$

At lower temperatures, like the usual conditions of the methanol synthesis, the WGS is shifted towards the right side due to its exothermic nature. At higher temperatures, upwards of 700 °C, the reaction reverses, and becomes the endothermic RWGS.[80]

Through the utilization of syngas, three reactions typically occur simultaneously, during methanol synthesis. These are (R 4.9), (R. 4.10), and (R. 4.11) [81].

$$CO_2 + 3H_2 \rightleftharpoons CH_3OH + H_2O \qquad \Delta H^0 = -49\,kJ/mol \qquad \text{(R. 4.10)}$$

$$CO + 2H_2 \rightleftharpoons CH_3OH \qquad \Delta H^0 = -91\,kJ/mol \qquad \text{(R. 4.11)}$$

However, studies have shown that at temperatures ranging from 200 to 300 °C, 30-100 bar, and in the presence of a Zink (Zn) or Cobber (Cu) catalyst, the primary source of carbon for methanol is CO_2, thereby favouring Reaction (R. 4.10). This primary conversion of CO_2 provides significant benefits for the e-methanol production through pure CO_2 and H_2. Kinetic studies have shown that the Reaction (R. 4.10) occurs up to two orders of magnitude faster than Reaction (R. 4.11), in the presence of a Cu-based catalyst. Based on these findings, a kinetic model has been utilized to determine the production of methanol through Reactions (R 4.9) and (R. 4.10). [80] [81]

4.6.1 Kinetic modeling

The methanol synthesis model is constructed Aspen Plus and is based on the kinetics and reactor properties presented by Cui et al., unless stated otherwise, the equations, relations, and reactor parameters are sourced by Cui et al.[82] All the kinetic parameters can be seen in Appendix D
The methanol synthesis model utilizes the EOS, *Predictive-Redlich-Kwong-Soave* (PSRK), to estimate chemical properties and relations. The methanol synthesis model utilizes the H_2 produced from the AWE model and the CO_2 captured from the MEA CC, to satisfy reaction (R. 4.10). The model uses the "RPlug" block in Aspen Plus to represent the kinetics of methanol conversion, presented in Figure 4.6 as R1.

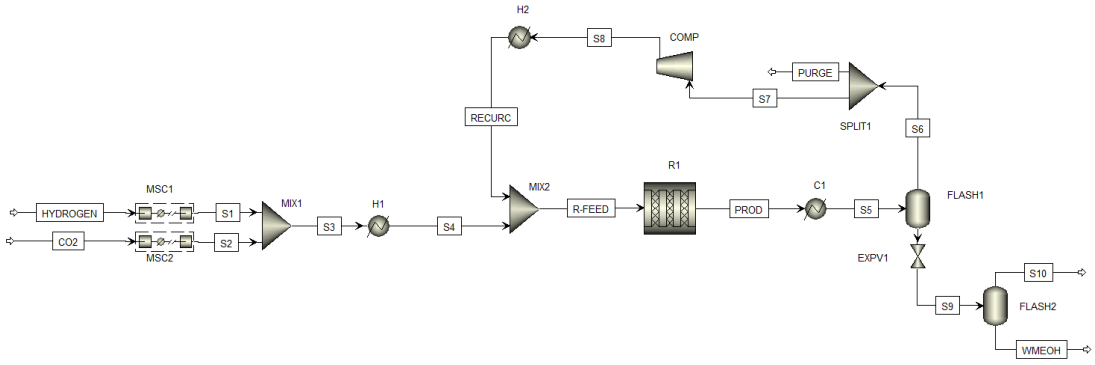

Figure 4.6: Aspen Plus methanol synthesis model from H_2 and CO_2

4.6.2 Reactor Specifications

The plug flow reactor is modeled with a loaded catalyst, pressure loss, adiabatic energy conditions, specified size, and under steady-state conditions. These specifications can be seen in Table 4.8.

Parameter	Value	Unit
Reactor length	7	[m]
Reactor diameter	4	[m]
Pressure drop scaling factor	1	[-]
Rougness	$4.572x10^{-5}$	[m]
Bed voidage	0.385	[-]
Particle density	1950	$\left[\frac{kg}{m^3}\right]$
Particle diameter	6	[mm]
Catalytic shape factor	0.857	[-]

Table 4.8: Reactor specifications for RPlug in Aspen Plus[82]

Since the reactor dimensions utilized by Cui et al. are designed for smaller flows, a size correction calculation has been done. Only the diameter of the reactor has been changed to ensure that the flow velocity through the reactor stays the same. This diameter is scaled with the same ratio as the molar flow is scaled with. The reason for only scaling the diameter is to keep the pressure loss over the reactor to a minimum. The pressure loss over the reactor is calculated using the Ergun equation, which can also be seen in Equation (4.21)

$$\frac{dP}{dz} = -\left(1.75 + 150\frac{1-\varepsilon}{Re_p^s}\right)\frac{1-\varepsilon}{\varepsilon^3}\frac{\rho_f u^2}{d_p^s} \tag{4.21}$$

Here $\frac{dP}{dz}$ describes the pressure loss P as a function of the reactor length z. ε is the bed voidage, Re_p is the particle Reynolds number, s is the catalytic shape factor, ρ_f is the fluid density in which the particle is submerged, u is the fluid velocity, and d_p is the particle diameter.

Since the compressibility factor for H_2 and CO_2 is not the same under the operating conditions, the required compressor work varies with the pressure. Through a compressor work sensitivity, the ideal operating pressure was found to be 36 bar. The conditions for the compressor work sensitivity analysis can be found in Appendix D.1.1.

Due to H_2 low compressibility factor at ambient temperature, it has been chosen to compress H_2 and CO_2 in two separate three-stage *multi-stage compression* (MSC) systems. H_2 is compressed from 6.7 bar and 25 °C, which are the exit conditions of the AWE model, to 36 bar. Likewise, the CO_2 is compressed from atmospheric pressure and 25 °C, which are the exit conditions of the MEA CC model, to 36 bar. The MSC systems utilize intercooling to account for the temperature increase during compression. However, to minimize the required cooling through intercooling, cooling is not applied at the last stage of the MSC. Furthermore, to minimize the required number

of heating units, mixing is applied before heating through "H1", where it is heated to 220 °C . Hereafter, it is sent into the reactor "R1", where the conversion to methanol and water occurs. After the reactor, the temperature increases, due to the exothermic nature of Reaction (R. 4.10), which introduces increased cooling. The product mixture is then cooled through "C1" to 25 °C, where the unreacted gas and the produced methanol and water are separated afterwards in "FLASH1". The unreacted gas is then recirculated, where 0.1% is purged from the system in "SPLIT1" to avoid mass buildup in the system. The remaining gas is then recompressed back to 36 bar via "COMP", due to the influence of the pressure drop from the reactor. The recirculated gas, is then reheated to 220 °C in "H2", before it is mixed back in with the feed flow in "MIX2", for further conversion in the reactor.

Recirculation is required to both increase conversion and reduce cost. By recirculating the unreacted reactants, a shift in equilibrium occurs in Reaction (R. 4.10), resulting in products being produced. Furthermore, since H_2 is upwards of 50 times more expensive than CO_2 from CCS, recirculation is required to make the process economically feasible. [83][84]

The liquid product stream, consisting mainly of water and methanol, is then depressurized through an expansion valve "EXPV1" to atmospheric pressure, where the remaining gas is purged out. This purge is required due to the VLE and CO_2's nature to dissolve in water, which is governed by Henry's law.

4.6.3 Results and Discussion

To look at how efficient the methanol synthesis model is, some parameters are more insightful than others. Values such as η_C, η_H, and the required duties are all relevant parameters to investigate to determine the overall performance of the system. These conditions can be seen in Table D.4

Summary of the Scaled Methanol Synthesis Model		
Parameter	**Value**	**Unit**
Key Parameters		
Mass Methanol Output, $\dot{m}_{\mathrm{MeOH}}$	22.89	[tonne/hr]
Mass Wet Methanol Output,$\dot{m}_{\mathrm{Wet,MeOH}}$	35.81	[tonne/hr]
Recirculation,m_{recirc}	101.10	[tonne/hr]
Unreacted H_2, y_{H_2}	87.7	[Mol%]
Unreacted CO_2,y_{CO_2}	4.02	[Mol%]
$\eta_{\mathrm{C}\rightarrow\mathrm{MeOH}}$	98.26	[%]
$\eta_{\mathrm{H}\rightarrow\mathrm{MeOH}}$	65.51	[%]
Energy Requirements		
MSC1 Duty, Q_{MSC1}	-3.32	[MW_{th}]
MSC2 Duty, Q_{MSC2}	-2.08	[MW_{th}]
H1, Q_{H1}	2.39	[MW_{th}]
H2, Q_{H2}	36.52	[MW_{th}]
C1, Q_{C1}	-67.90	[MW_{th}]
MSC1 Electrical Work,W_{MSC1}	5.02	[MW_e]
MSC2 Electrical Work,W_{MSC2}	3.07	[MW_e]
COMP, W_{COMP}	0.12	[MW_e]

Table 4.9: Required heating and cooling during methanol synthesis model

From Table D.4, it can be seen that the majority of the energy requirements come from cooling the product stream before separation, and reheating it again before mixing. The significant heating required is based on the recirculated amount of gas of 101.10 tonne/hr, which introduces a large amount of thermal mass to the system. The required compressor work to lift the pressure back up to 36 bar is almost insignificant compared to the required compressor work delivered by MSC1 and MSC2 to lift the pressure from 6.7 and 1.01 bar to 36 bar, respectively. The overall heat requirements are dominated by the cooling requirement of "C1". This cooling requirement could potentially be reduced through heat integration with units such as "H1", which have similar temperature ranges, but are opposite. The investigation of the potential heat integration, is further analyzed in Chapter 8.

From Table D.4, it can be seen that the η_{C} and η_{H} are approximately 98.3% and 65.5%, respectively. Even though the model experiences atom balance, a 100% carbon conversion is nearly impossible to achieve. The carbon atoms which is not being turned into methanol are either turned into CO through the WGS reaction or not reacted at all, resulting in unreacted CO_2. These gases are purged from the system to avoid mass buildup. A η_{H} of 65.51%, reflect the close to ideal conversion H_2 to methanol through Reaction (R. 4.10). 100% conversion, through this reaction would result in a η_{H} of 66.66%. Due to the impossible nature of reaching 100% equilibrium, this would not be reachable.

4.7 Experimental and Model Integration

The technologies presented in Chapter 4 have all been developed and commercialized to varying degrees, based on known chemical and physical characteristics. All technologies, including the MEA CC model, the AWE Model, and the Methanol Synthesis model, have been theoretically modeled based on existing literature to form a framework for eSAF production via MTH and its integration.
However, due to the complexity of MTH and its reactions, further extensive research is necessary to fully understand the mechanisms behind its conversion, which is essential for theoretical modeling of the process. Additionally, the technology is far from mature and still requires research regarding catalyst selection to find an optimal candidate that maximizes the yield of jet fuel while ensuring its quality is eligible for either blending or replacement of commercial jet fuel. Upon the already highly complex mechanisms governing MTH reaction, the addition of catalyst selection introduces dynamic variables impossible to predict and accurately model based on available theoretical information. Thus, experimental data are required to represent a commercial MTH synthesis plant for integration in an eSAF system.
The following experimental Chapter 5, thus, aims to both find a well-suited catalyst, producing high yields, as well as high-quality jet fuel eligible as blendstock or complete substitution, and inputs to an experimentally tuned MTH model, which can be integrated into the eSAF production model. Figure 4.7, illustrates the pathway of experiments conducted to achieve a representative selection of reference compounds to acquire yields of produced HCs in the *light petroleum gas*(LPG), Gasoline, Kerosene, and Diesel range, as well as heat generation associated with the conversions, to model the thermal integration of eSAF production.

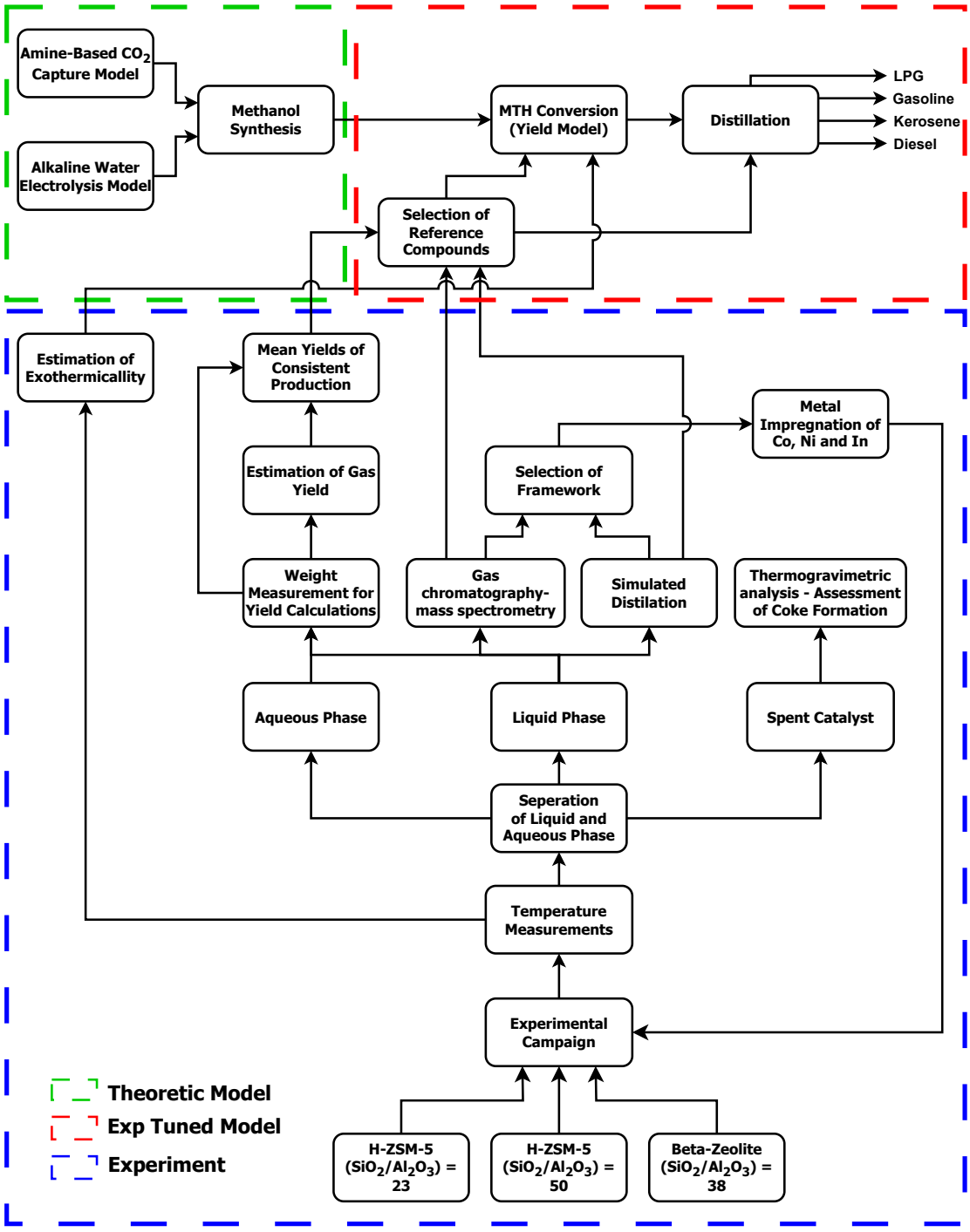

Figure 4.7: Flowchart of the connection between theoretical modeling and experimental work used to experimentally tune the MTH and distillation model.

Chapter 5

Experimental Methods

Given the dynamic complexity of MTH and the lack of well-defined reaction pathways, experiments were performed using a methanol/water mixture of 64/36 vol.%, representing that of undistilled methanol, to gather inputs for a yield-based MTH model. For further reference, the methanol/water mixture will be referenced as wet methanol. This composition was selected to align with the modeling assumptions and to maintain consistency with previous, yet to be published, experimental studies by Kamaldeep Sharma, using the same mixture.

The experimental work has two primary objectives:

1. To gather input for the MTH model through experimental data.
2. To evaluate various catalysts in a continuous packed bed reactor (PBR) to identify the most suitable candidate for jet fuel production.

The experimental analysis consists of the following methods:

- **Liquid Yields Analysis**: Collected mass balances are used to calibrate the model by fitting to experimental yields.
- **Temperature Measurements**: To assess the reaction enthalpy of tested catalysts, providing data for heat integration in the MTH model.
- **Simulated Distillation**: Determines the distribution of products in the LPG, gasoline, jet fuel, and diesel ranges, supporting the selection of reference chemicals to match experimental data.
- **Gas chromatography-mass spectrometry (GC-MS)**: Provides detailed information on the produced compounds, enabling the selection of appropriate reference compounds for the MTH model.
- **Thermogravimetric analysis (TGA)**: Assesses coke formation and identifies the regeneration temperatures required for different catalysts. This analysis is not intended for model tuning but is crucial for understanding catalyst deactivation.
- **Catalyst Lifetime Evaluation**: Although not directly influencing model inputs, catalyst stability and longevity are critical for optimizing jet fuel production.

5.1 Experimental Setup

The experimental setup used for all conducted experiments consists of the following key components and can be seen in Figure 5.1.

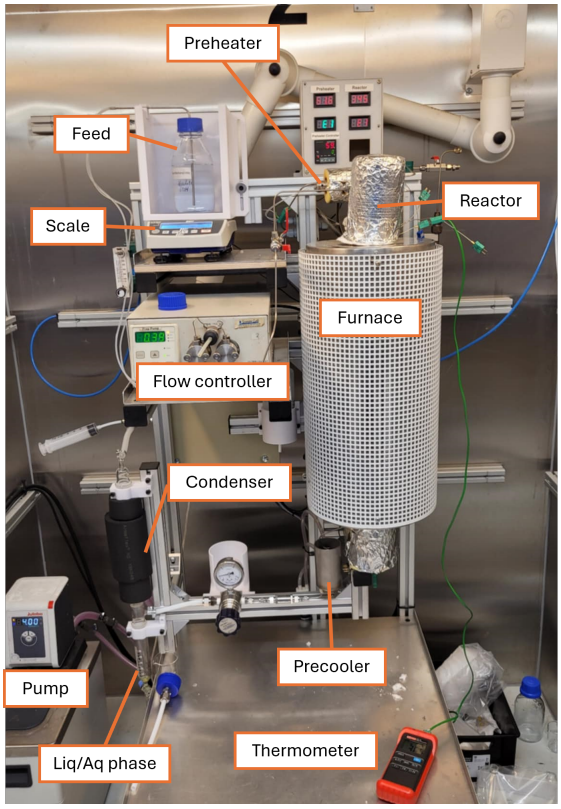

Figure 5.1: Experimental setup used for all conducted experiments [18].

- **Scale**: Measures the feed of wet methanol to calculate the mass balances and estimate the gas yield
- **Flow Controller**: Pumps and regulates the flow rate of wet methanol to the PBR. A fixed flow rate corresponding to a *Weight hour space velocity* (WHSV) = 1.6 h^{-1} has been used for all experiments.
- **Preheater**: Heats the wet methanol to 200°C before entering the PBR. 200°C has been aligning with previously conducted experiments.
- **Packed Bed Reactor**: Reacted bed fully packed with synthesized catalysts.
- **Furnace**: Heats the PBR to a selected temperature for 350°C. This temperature has been selected from previous findings from temperature studies with ethanol feed [18].
- **Thermocouples**: Measures the temperature in the top, middle, and bottom sections of the reactor.
- **Precooler**: Cools the unreacted water from the wet methanol and liquid products from the reactions at room temperature.

- **Back Pressure Regulator**: Regulates the back pressure of the system. A gauge pressure of 1 bar has been used to ensure consistent flow.
- **Condenser**: Condenses reaction products at atmospheric pressure and 4°C for collection.
- **Cylindrical Separation Funnel**: Collects the aqueous and liquid HC phases for sampling.

5.2 Catalyst Selection

As discussed in Section 1.4.2, the selection of the catalyst is vital for the selectivity. Considering the technical challenges associated with commercializing the MTJ technology in a single PBR zeolitic MTH process, along with the findings from previous experiments with ethanol feed over V-ZSM-5 with a SiO_2/Al_2O_3 = 23, the chosen catalyst should aim to achieve the following:

- Enhance the yield of liquid HC within the distillation range of Jet fuel
- Reduce the selectivity towards aromatic compounds, better aligning with the mix of typical Jet A-1 fuel
- Resistant to deactivation by coke formation
- Maintain consistent yields of liquid HC over extended operation
- Be applicable for regeneration to support prolonged catalyst lifetime.

5.2.1 Catalyst Framework

Given that the zeolite framework largely dictates the size of the HC products, two primary frameworks, ZSM-5 and Beta Zeolite, were selected for testing without metal loading and H^+ as the cation.
ZSM-5 has been widely utilized in MTH processes since the 1980s, primarily for gasoline production, due to its intermediate pore size of 5.4 - 5.6 Å [85]. This pore structure typically favors the formation of HCs within the gasoline distillation range. However, if its primary distillation range can be tuned towards jet fuel, ZSM-5 presents a promising candidate for MTJ in a single PBR system and has therefore been chosen as one of the tested frameworks.
In contrast, Beta Zeolite has larger pores of 6.6 - 7.7 Å, making it capable of producing longer-chain HCs compared to ZSM-5. This characteristic is expected to enhance the yield of HCs within the jet fuel distillation range. Furthermore, metal-loaded Beta Zeolite has successfully demonstrated its potential in producing bio-jet fuel through hydrotreatment of long-chain fatty acids, as well as in FT synthesis, indicating its

potential for jet fuel applications. [86] [87]. However, studies surrounding its utilization in MTH within the jet-fuel range are limited, motivating the investigation of the framework. However, as later discussed in Section 6.6, MTH conversion over the Beta-Zeolite framework was unsuccessful.

5.2.2 Acidity

Among the tested frameworks, ZSM-5 was chosen for further investigation at two different SiO_2/Al_2O_3 ratios of 23 and 50. This was aimed at exploring the influence of acidity on the DCP process. Theoretically, the lower SiO_2/Al_2O_3 ratio increases the number of BAS, enhancing the catalyst's acidity and promoting the aromatic cycle. Conversely, a higher SiO_2/Al_2O_3 ratio reduces the number of BAS, decreasing acidity and favoring the olefinic cycle.
The primary objective of testing the higher SiO_2/Al_2O_3 ratio of 50 was to mitigate the high aromatic yield observed in previous studies during ethanol conversion to HCs [18]. By reducing aromatic content, the goal was to increase the proportion of aliphatic compounds, thereby achieving a product distribution more representative of jet fuel. However, literature indicates that lower acidity is often associated with reduced catalytic activity, and the olefinic cycle typically produces shorter-chain HCs. Consequently, the overall yield of HCs within the jet fuel distillation range is expected to decrease [43] [88].

5.2.3 Metal-Loading

Following the testing of various zeolite frameworks and acidity properties, ZSM-5(50) was selected for metal loading, due to its higher selectivity towards aliphatic components, better mimicking the composition of conventional jet fuel, as further discussed in Section 6.3. All metal depositions were carried out via the wet impregnation method, targeting a loading of 10 wt.% for each selected metal, as described in Section 5.2.4. The metal loading calculation is defined in Equation (5.1):

$$\text{Metal loading} = \frac{m_{\text{metal}}}{m_{\text{ZSM5}}} \cdot 100 = 10\% \tag{5.1}$$

where m_{metal} represents the mass of the active metal, which is determined from the metal precursor. The mass contribution of the metal in the precursor is calculated based on its molar fraction, as described by Equation (5.2):

$$m_{metal} = \frac{MW_{\text{metal}}}{MW_{\text{precursor}}} m_{\text{presursor}} \tag{5.2}$$

Three metal candidates were selected for testing based on their catalytic properties and industrial applications:

- Nickel (Ni)
- Cobalt (Co)
- Indium (In)

Nickel

Nickel was chosen due to its widespread application in olefin oligomerization and dimerization on various catalyst supports [89]. Industrial processes utilizing nickel typically operate at lower temperatures (<200°C) and higher pressures (10-50 bar) than the MTH process. Although commercial oligomerization plants prefer utilizing homogeneous catalyst systems associated with superior stability and selectivity [89], it is still expected that the addition of nickel on the heterogeneous ZSM-5 will promote more oligomerization and dimerization reactions. This should enhance the formation of longer HC chains, increasing the yield within the distillation range of jet fuel.

Cobalt

Cobalt is primarily used in Fischer-Tropsch synthesis for converting syngas into long-chain paraffins under moderate pressures (>10 bar) and temperatures below 250°C [90]. Its applications in MTH are less explored, but literature suggests that Co-loaded ZSM-5 increases selectivity towards the olefinic cycle, due to its selectivity towards hydrogenation reactions [91]. This should favor the formation of aliphatics over aromatics and imitate the composition of typical jet fuel better. However, due to the olefinic cycle producing short-chained HCs, it is anticipated that the addition of cobalt may decrease the overall yield within the liquid fraction or the chain length of liquid HCs.

Indium

Indium is commonly used in industrial applications for dehydrogenation of light alkanes to alkenes, such as the conversion of propane to propylene and ethane to ethylene. While typical reaction temperatures for dehydrogenation processes exceed those of MTH, up to 700°C, [92, 93]. However, under the milder conditions of MTH, adding indium to ZSM-5 is still expected to promote more dehydrogenation, potentially increasing the liquid yield due to the more reactive nature of alkenes. However, the promotion of the dehydrogenation reactions is also expected to increase aromatization reaction, increasing the selectivity towards aromatics.
Additionally, group 13 metals, including Aluminium (Al), Gallium (Ga), and Indium (In), increase the Lewis acidity due to their strong electron deficiency, promoting redox reactions and aromatization [94]. As a result, higher liquid yield is expected with a trade-off of lower aliphatic yields.

An overview of all tested catalysts is shown in Table 5.2.3 below:

Catalyst	SiO_2/Al_2O_3	Metal loading	Feed	Temperature	WHSV
H-Beta[a]	38	N/A	Wet Methanol	350 °C	1.6 h^{-1}
H-ZSM-5	23	N/A	Wet Methanol	350 °C	1.6 h^{-1}
H-ZSM-5	50	N/A	Wet Methanol	350 °C	1.6 h^{-1}
Co-ZSM-5	50	10 wt.%	Wet Methanol	350 °C	1.6 h^{-1}
Ni-ZSM-5	50	10 wt.%	Wet Methanol	350 °C	1.6 h^{-1}
In-ZSM-5	50	10 wt.%	Wet Methanol	350 °C	1.6 h^{-1}

Table 5.1: Experiments conducted on the PBR setup.
[a] Only one sample collected, due to repeated equipment failure, identified by excessive penta- and hexamethylbenzene formation, condensing and clogging the precooler.

5.2.4 Catalyst Synthesis

Commercial NH_4-ZSM-5 (product no. CBV 2314), SiO_2/Al_2O_3 = 23 was previously purchased from Zeolyst International, while NH_4-ZSM-5 (product no. 45881.22), SiO_2/Al_2O_3 = 50, and Zeolite NH_4-Beta (product no. 45874.22) SiO_2/Al_2O_3 = 38, was purchased from Avantor ScienceCentral (VWR). Both H-ZSM-5 SiO_2/Al_2O_3 = 23 & 50, as well as, H-Beta SiO_2/Al_2O_3 = 38. All were prepared by calcination overnight under air at 550°C for 6 hours with 2°C/min ramping rate, followed by an isotherm temperature at 105°C, replacing the ammonium cation with H^+.

Wet Impregnation

For the preparation of the metal-loaded catalysts, Co-ZSM-5, Ni-ZSM-5, and In-ZSM-5 with SiO_2/Al_2O_3 = 50, the following metal precursors were used:

- **Cobalt(II) acetate tetrahydrate** ($(CH_3COO)_2Co \cdot 4H_2O$)
- **Nickel(II) nitrate hexahydrate** ($Ni(NO_3)_2 \cdot 6H_2O$)
- **Indium(III) nitrate hydrate** ($In(NO_3)_3 \cdot xH_2O$), assuming $x = 5$ during calculations.

The precursors were dissolved in a 0.10 M aqueous solution within a round-bottom reaction flask under a fume hood. The required mass of each precursor was determined using Equations (5.1) and (5.2). Next, 15 g of NH_4-ZSM-5 (SiO_2/Al_2O_3 = 50) was gradually added to the solution. The mixture was suspended under reflux with constant stirring and heated to 80 °C using an oil bath for 16 hours. To minimize water consumption, the reflux condensers were connected to a closed-loop cooling pump operating at 4 °C. After wet impregnation of the metals, the solutions were triple vacuum filtered at 550 mbar, followed by drying at 105 °C for 4 hours. Subsequently, the catalysts were separated from the filter paper and dried for an additional 12 hours before calcination at 550 °C for 6 hours with a ramping rate of 2 °C/min.

Pellet Extrution

After calcination, the catalysts were combined with organic and inorganic binders and mixed with distilled water to form a thick, homogeneous paste. This paste was extruded using a custom-built extruder to produce uniform pellets.
The complete catalyst synthesis procedure is illustrated in Figure 5.2.

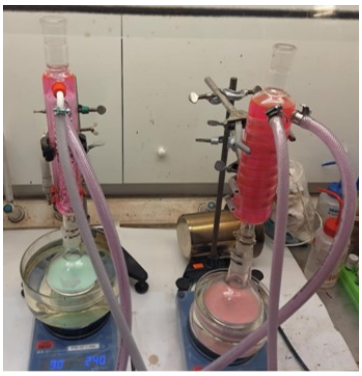

(a) Wet impregnation of ZSM-5 with nickel (left) and cobalt (right).

(b) Vacuum filtration of impregnated ZSM-5 at 550 mbar

(c) Calcined impregnated ZSM-5

(d) Wet catalyst paste with binders

(e) Extruded uniform strands of catalyst

(f) Final catalyst pellets

Figure 5.2: Complete catalyst synthesis procedure.

5.2.5 Activation of Catalyst

The synthesized catalysts pellets were packed into the PBR, and the catalyst mass loaded into the reactor was noted as m_{catalyst}. Prior to methanol feed introduction, the catalysts were activated under nitrogen flow at 400 °C for one hour. This activation process serves multiple purposes:

Nitrogen flow acts as a cleaning process, which facilitates the removal of adsorbed

water, organic residues from the binder, and potential by-products from the catalyst synthesis. This purification process increases the surface area accessibility and minimizes surface contamination, improving catalytic performance. This step is essential to expose the active metallic sites necessary for catalytic activity. Furthermore, activating the catalyst under an inert atmosphere prevents the impregnated metal from potentially oxidizing and changing the activity of the catalyst. [95].

5.3 Experimental Campaigns

Each catalyst test underwent an experimental campaign where wet methanol was continuously fed and converted until the end-of-life was reached at a given time-on-stream (TOS). Under each campaign, samples were collected at set intervals, from which the liquid HC yields were estimated.

5.3.1 Theoretic Maximum Yields

Each catalyst was tested with a wet methanol feed to achieve WHSV of 1.6 h^{-1}, as determined by Equation (5.3):

$$\text{WHSV} = \frac{\dot{m}_{\text{MeOH}}}{m_{\text{catalyst}}} = \frac{\dot{V}_{\text{MeOH}}\rho_{\text{MeOH}}}{m_{\text{catalyst}}} = \frac{\dot{V}_{\text{feed}}\left(\varphi_{\text{MeOH}}\rho_{\text{MeOH}} + \varphi_{\text{H}_2\text{O}}\rho_{\text{H}_2\text{O}}\right)}{m_{\text{catalyst}}\varphi_{\text{MeOH}}} = 1.6\ \text{h}^{-1} \tag{5.3}$$

where $\dot{V}_{\text{feed}}$ is the total volumetric flow rate of the feed, φ and ρ represent the volume fraction and density of methanol and water, respectively. Since only methanol reacts, the total feed flow rate is adjusted based on its volumetric fraction in the mixture.
As described in Section 1.3, methanol first undergoes dehydration to form DME, which is subsequently converted to ethene. The overall reaction pathway can be summarized as shown in Reaction (R. 6.2):

$$2\text{CH}_3\text{OH} \rightleftharpoons \underbrace{\text{C}_2\text{H}_4}_{43.75\ \text{wt.\%}} + \underbrace{2\text{H}_2\text{O}}_{56.25\ \text{wt.\%}} \tag{R. 6.2}$$

Only ethene is further converted to higher HCs, setting the maximum theoretical HC yield from the methanol feed at 43.75 wt.%, assuming complete methanol conversion.

5.3.2 Sample Collection

Samples, referred to as "mass balances" (MB), consisting of the liquid HC and aqueous phases, were collected every two hours, with the exception of 12-hour samples for overnight runs. To ensure steady-state conditions, products collected during the first hour of TOS of each campaign were discarded. The first analyzed samples were taken at TOS = 2 h, under the assumption that steady-state operation is reached after two hours, with coke formation considered negligible.

Chapter 6

Experimental Results and Discussion

This chapter presents the outcomes of the experimental campaign conducted to evaluate the performance of various zeolite-based catalysts in the MTH process. The experiments were carried out under controlled conditions, as described in Chapter 5, and are aimed at understanding differences in catalytic activity, product distribution, and catalyst stability across the selected catalysts.

6.1 Liquid Hydrocarbon Yields and Time-on-Stream Stability

The catalytic performance of each tested catalyst was evaluated based on the yield of liquid HC relative to the theoretical maximum yield of 43.75 wt.%. Since the primary objective of this study is the production of liquid fuels suitable for jet fuel applications, the collected liquid phase was isolated, weighed, and its yield calculated. The remaining theoretical yield was assumed to be distributed within the gaseous phase, under the assumption of complete methanol conversion, corresponding to the finding in the literature before end-of-life [96]. Any amount of unreacted methanol is thus neglected and unaccounted for. The yield of liquid HCs as a function of time on stream (TOS) for all catalysts is presented in Figure 6.1.

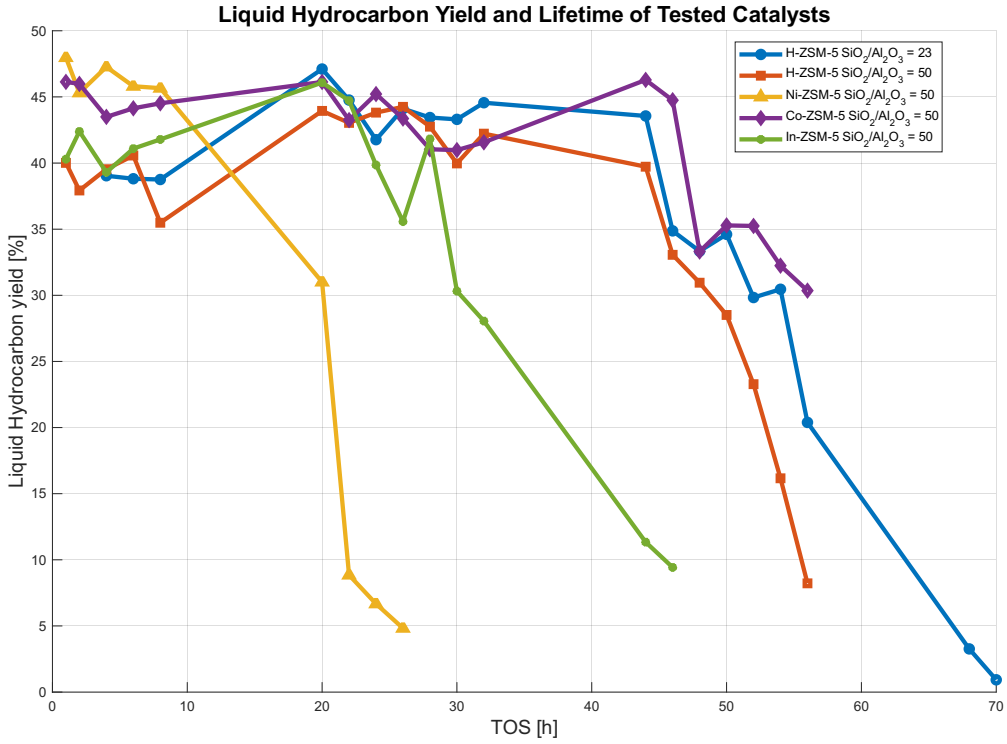

Figure 6.1: Actual/Theoretical maximum Liquid HC yield and lifetime of tested catalysts.

Each catalyst exhibited distinct deactivation behavior and stable HC yields within their active lifetime. Notably, fluctuations in HC yield were observed across the TOS for all tested catalysts. These variations are primarily attributed to measurement and sampling uncertainties. Significant increases in yield were linked to temporary reductions in the WHSV caused by air bubbles entering the pump during feed refilling, thereby decreasing the overall volumetric flow rate and allowing for increased reaction time.
The active lifetime has been defined as the TOS before a decrease in liquid yield, which has been used to determine the mean yield. Total lifetime has been defined as the TOS before the yield has reduced significantly, to 75% of its average yield.

Both H-ZSM-5(23) and H-ZSM-5(50) demonstrated stable HC yields of approximately 43.0 wt.% and 41.1 wt.%, over a period of 44 hours, respectively, and maintained activity for over 50 hours. Ni-ZSM-5(50) displayed a notably higher initial yield of 46.0 wt.%, but experienced rapid deactivation, leading to a significant drop in liquid yield before the 20-hour mark. It is worth noting that Ni-ZSM-5(50) deactivated during an overnight sampling, rendering the exact active lifetime uncertain.
The Co-ZSM-5(50) catalyst maintained its activity for 46 hours with a stable yield of 43.9 wt.%. However, complete deactivation was not observed during the campaign, and its total lifetime remains partially undetermined. In contrast, In-ZSM-5(50) showed moderate stability with an active lifetime of 28 hours and an average yield of

41.4 wt.%. The summary of catalyst performance is provided in Table 6.4.

Catalyst	Max yield	Mean yield	Active lifetime	Total lifetime
H-ZSM-5(23)	47.1 wt.%	43.0 wt.%	44 h	56 h
H-ZSM-5(50)	44.2 wt.%	41.1 wt.%	44 h	52 h
Ni-ZSM-5(50)	47.3 wt.%	46.0 wt.%	<20 h[a]	22 h
Co-ZSM-5(50)	46.1 wt.%	43.9 wt.%	46 h	56 h[b]
In-ZSM-5(50)	46.1 wt.%	41.4 wt.%	28 h	32 h

Table 6.1: Summary of yield and lifetimes of tested catalysts. Active lifetime refers to the TOS before a decrease in liquid yield, while total lifetime is defined as the TOS before a yield reduction to 75% of its average.
[a] Ni-ZSM-5(50) deactivated during overnight sampling; the exact active lifetime is unknown.
[b] Co-ZSM-5(50) campaign ended before complete deactivation.

Overall, the yields of the tested catalysts followed the expected trends, with higher SiO_2/Al_2O_3 ratios resulting in lower liquid HC yields, as observed for the H-ZSM-5 zeolites. This is attributed to increased selectivity towards the olefinic cycle. However, H-ZSM-5(50) was expected to exhibit a longer lifetime compared to H-ZSM-5(23) due to its reduced activity and lower aromatic formation, associated with lower acidity. This could suggest that the coke formed at higher acidities differs from the coke formed at lower acidities. Here, less acidic catalysts may be dominated by the condensation of larger aliphatic compounds, contrary to the condensation of aromatic compounds in the formation of polyaromatics. This difference in coke nature could influence the energy required for its regeneration, and has, as a result, been further investigated by TGA analysis.

Expectedly, the nickel impregnated catalyst increased the yield of liquid HCs, consistent with its enhanced selectivity towards oligomerization and dimerization reactions of short olefins. However, as a tradeoff, nickel also significantly decreased the lifetime of the catalysts. This could be attributed to two main factors: Firstly, the nickel loading of 10 wt.% may be excessive and exceed the optimal loading capacity, resulting in sintering and pore blockage, which reduce the accessible active surface area [97] [98]. Furthermore, literature suggests that nickel inherently has a lower resistance to coking, comparable to other metals, often requiring additional catalyst engineering to increase its resistance to coking [99].
Despite the favorability of the olefinic cycle with the incorporation of cobalt, the overall liquid yield increased compared to the unmodified H-ZSM-5(50). This suggests that, despite cobalt being used as an FT synthesis catalyst due to its selectivity towards hydrogenation of CO, cobalt also increases the selectivity towards oligomerization and dimerization of the short olefins produced from methanol, increasing the yield of liquid HCs. Furthermore, cobalt exhibited great resistance to coking, slightly extending the catalyst's active lifetime compared to its unmodified counterpart.

Indium addition had minimal impact on the average liquid yield during periods of stable operation but notably reduced the catalyst's overall lifetime. This could be attributed to excessive loading, resulting in faster deactivation. Interestingly, at TOS = 28 h, a substantial increase in yield from 35.6 wt.% to 41.8 wt.% was observed when the flow rate was temporarily reduced, due to air bubbles in the pump. This suggests that the reactions facilitated by indium may be highly sensitive to WHSV, potentially indicating slower kinetics compared to the other tested catalysts, as no comparable yield increase was observed for the other catalysts under similar changes in WHSV, when air bubbles entered the pump. However, due to the lack of repeatability and the presence of experimental uncertainties and potential errors, this observation remains inconclusive.

6.2 Recorded Temperature Measurements

The temperature profiles within the reactor provide insights into the enthalpy changes associated with the HC formation reactions. An increase in temperature, $\Delta T > 0$, indicates that the overall reaction is exothermic ($\Delta H_r < 0$), while a decrease ($\Delta T < 0$) suggests endothermic behavior ($\Delta H_r > 0$). Depending on the selectivity towards the aromatic or olefinic cycle and the predominant reaction pathways, the overall reaction enthalpy within the reactor varies, resulting in different temperature gradients along the catalyst bed.

Described in Section 1.3.1, the reactor setup follows the "cigar model," where catalyst deactivation progresses along the flow path of methanol. Initially, reactions are most intense at the top of the reactor, which is the first point of methanol contact. Over time, this region deactivates due to coke formation, shifting the reaction zone further down the reactor. This progressive deactivation creates distinct reaction zones, where the majority of HC synthesis occurs. Given that the primary reactions are exothermic, hotspots emerge in these active regions depending on the TOS. The temperature measurements recorded throughout the campaigns of all tested catalysts are illustrated in Figure 6.2.

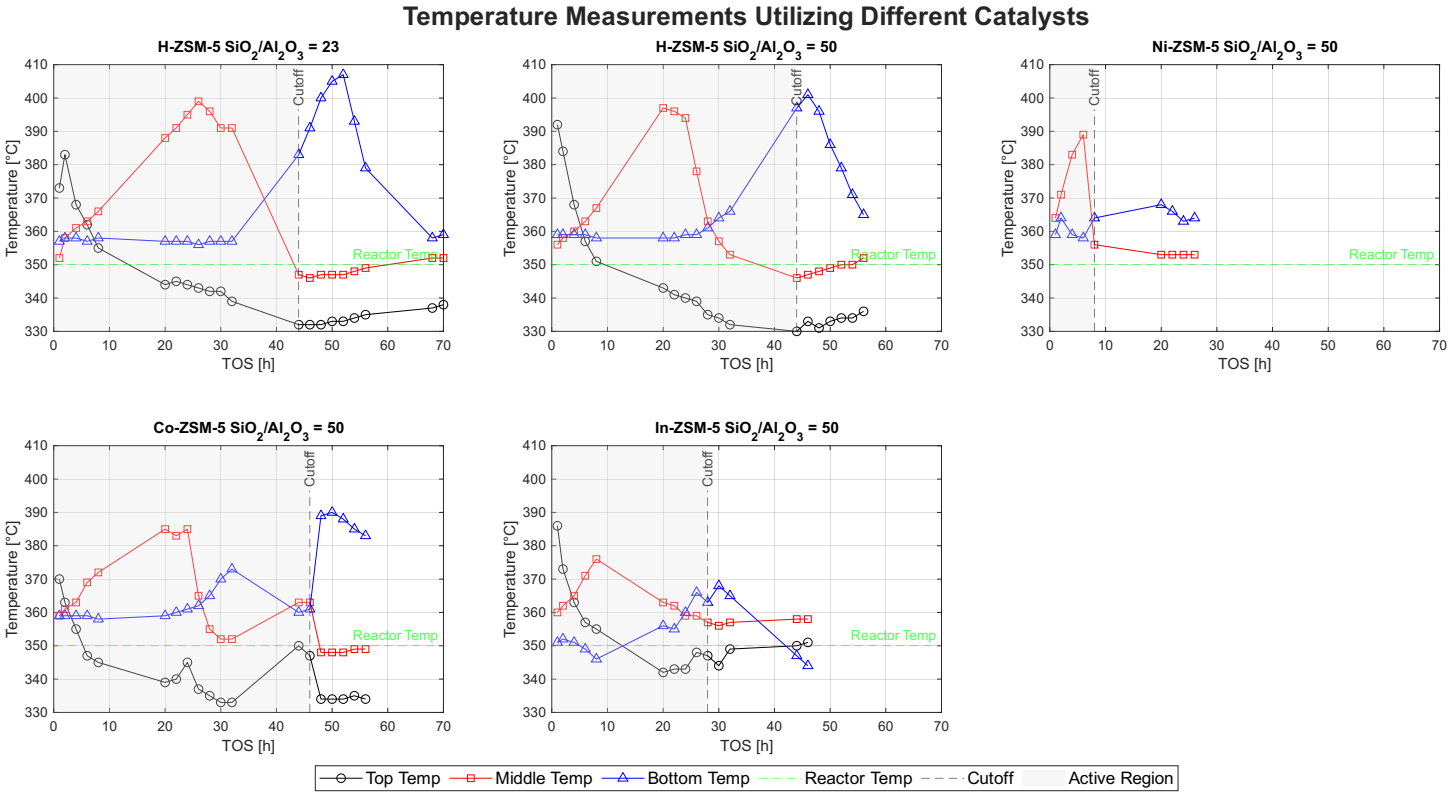

Figure 6.2: Temperature measurements throughout all campaigns of the tested catalysts. The top temperature of Ni-ZSM-5(50) is missing due to a defective thermocouple. The active region indicates the TOS of consistent yield used for mean yield calculations and mean ΔT for the campaigns.

Distinct temperature hotspots are observed for all catalysts, indicating the overall reaction is exothermic in the active regions of the reactor. Notably, the temperature at the top of the reactor rapidly drops after a short TOS due to deactivation from coke formation. This deactivation results in a temperature drop below the set reactor temperature of 350 °C, as indicated by the green line. This observation is mainly attributed to the reduced exothermic heat release from reactions in the deactivated region, forcing the reactor furnace to heat the feed from the preheated temperature of 200 °C, to the set reactor temperature of 350 °C, which causes the top section temperature to fall below the set temperature. However, these observations might also be influenced by endothermic dehydration of DME to ethene as seen in Reaction (R 1.3), which possibly still proceeds even with reduced catalyst activity due to relatively fast kinetics, similar to the comparably rapid kinetics of ethanol dehydration during ethanol to HC conversion as demonstrated by Gayubo et al. [100].
Additionally, temporary increases in the top temperature at TOS = 44 h and TOS = 46 h for Co-ZSM-5(50) were observed. This was attributed to reduced feed flow caused by air bubbles in the pump, allowing for increased heat transfer to the feed.

The active region with consistent yield is typically cut off around the same time the temperature in the bottom section peaks, indicating a shift in the primary reaction zone. For both H-ZSM-5 catalysts and the Co-ZSM-5 catalyst, the temperature peak in the bottom is slightly higher than in the middle and top sections. Whether this is also the case for the Ni-ZSM-5 catalyst is undetermined, as the catalyst deactivated significantly during the overnight run, and the top section temperature was not recorded due to the defective thermocouple. Interestingly, for the In-ZSM-5 catalyst, the temperature peaks show an opposite tendency, decreasing from the top to the bottom section. This could be attributed to the unique properties of indium, which may influence the distribution of active sites and the progression of deactivation differently compared to other metals. Table 6.4 summarizes the highest observed temperatures for the campaigns and the mean temperature of the active region with consistent yield, used for determining the heat produced from each catalyst in the MTH model in Chapter 7.

Catalyst	Max Temperature	Mean ΔT	Active Region
H-ZSM-5(23)	407 °C	12.7 °C	44 h
H-ZSM-5(50)	397 °C	9.5 °C	44 h
Ni-ZSM-5(50)	389 °C	18 °C	8 h
Co-ZSM-5(50)	390 °C	7.5 °C	46 h
In-ZSM-5(50)	396 °C	6.6 °C	28 h

Table 6.2: Highest observed temperatures as well as mean ΔT for the active region. The mean ΔT, includes temperatures below the set reactor temperature of 350 °C.

The observed temperature profiles and shifts in active regions highlight the complex relation between catalyst composition, deactivation mechanisms, and reaction exothermicity. Understanding these dynamics is crucial for optimizing catalyst performance and heat integration in MTH processes to ensure controlled temperature management for consistency in yields and quality.

6.2.1 Analysed Samples

To capture the development of HC production as the catalyst gradually deactivates and the reaction enthalpy changes, four samples from each campaign were selected for further analysis of GC-MS and SimDist. The first sample, taken at a TOS of 2 hours, represents the initial product distribution. Additional samples were collected at approximately 35% and 70% of each catalyst's total lifetime, reflecting the product composition during the early and late stages of its operational life. Finally, a sample was taken at the end-of-life of each catalyst to observe the final product distribution.

To ensure the samples accurately represent the catalyst's performance at each TOS, overnight samples were excluded from the analysis. The specific samples chosen for analysis are listed in Table 6.3.

Catalyst	Start	Lower Middle	Upper Middle	End
H-ZSM-5(23)	MB2	MB24	MB48	MB68
H-ZSM-5(50)	MB2	MB24	MB48	MB56
Co-ZSM-5(50)	MB2	MB24	MB48	MB56
Ni-ZSM-5(50)	MB2	MB8	MB22	MB26
In-ZSM-5(50)	MB2	MB8	MB28	MB46

Table 6.3: Selected samples from each catalyst campaign, representing key stages of deactivation.

6.3 Gas Chromatography-Mass Spectrometry

GC-MS analysis was utilized to determine the chemical composition of the products generated by the various catalysts. This technique combines a gas chromatogram with a mass spectrum, enabling the qualitative identification of compounds by comparing their retention times and mass spectra with those of known standards [101]. The retention time and peak magnitude provide insights into both the presence and relative abundance of each compound.

To achieve accurate concentration measurements, individual calibration of the GC-MS for each compound is required, as different compounds produce distinct peak responses. Given the complexity of the MTH product, which contains hundreds of compounds, calibration for each component is not feasible. Therefore, the relative abundance of each compound was estimated using its peak area as a fraction of the total spectrum area. The GC-MS analysis identified the 200 most abundant compounds of each sample, with the top 98% of the total peak area, typically representing around 70-110 compounds, assumed to represent the overall distribution

For this study, the products were grouped into the following key HC classes relevant to jet fuel production: Aliphatic components consisting of, n-paraffins, iso-paraffins, cyclo-aliphatics, and olefins, aromatic components, classified into BTX's, due to their petrochemical value, consisting of Benzene, Toluene, and Xylene, other aromatics, oxygenates, which are noted for their negative impact on heating value, and naphthalene, which is limited to a maximum of 3.0 vol.% in commercial jet fuel.

6.3.1 Product Distribution of Test Catalysts

The average distribution of HC classes produced by the tested catalysts is shown in Figure 6.3.

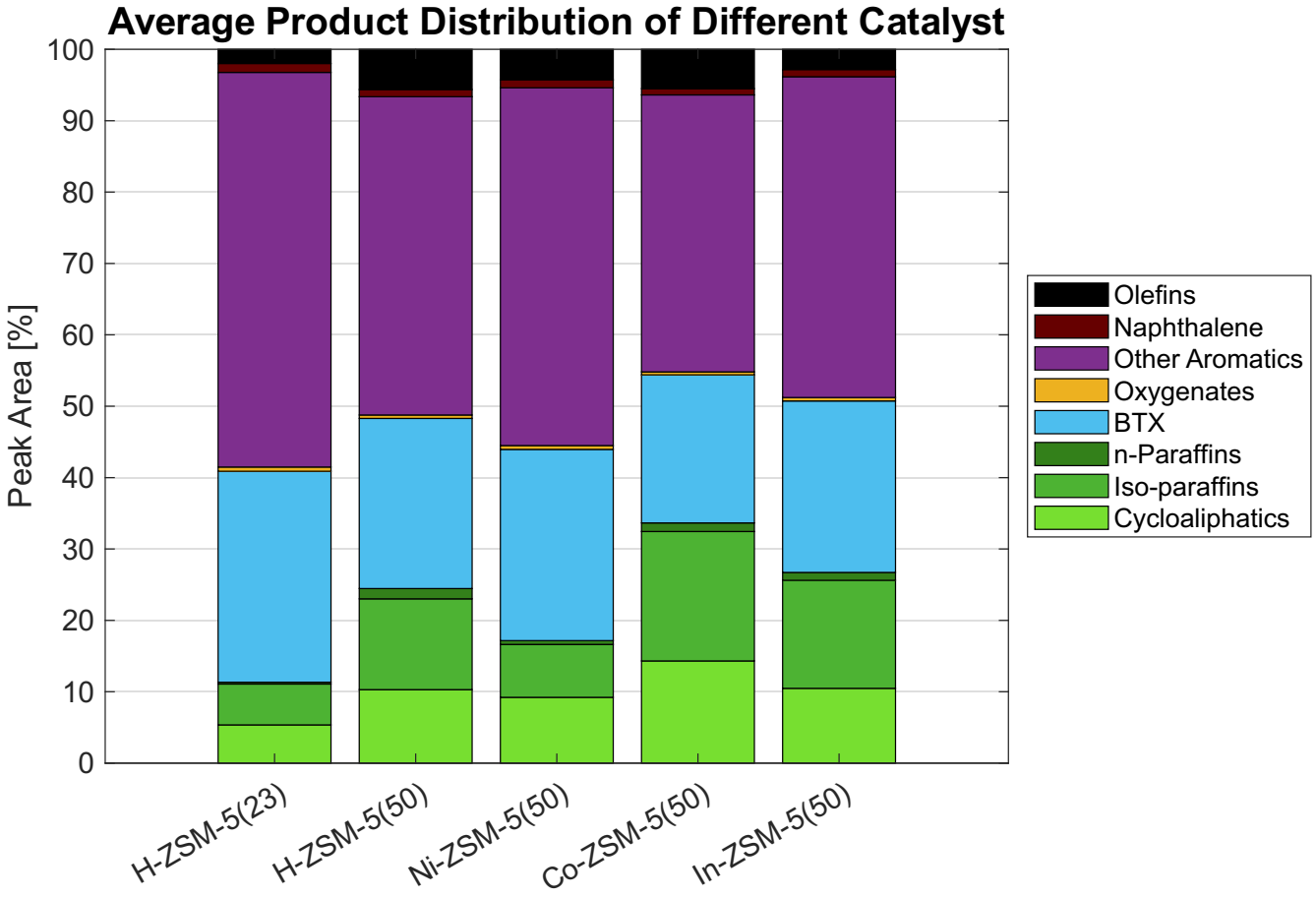

Figure 6.3: Average product distribution of the tested catalysts based on the peak area from GC-MS analysis.

General Observations

Across all catalysts, a general selectivity toward aromatic compounds over aliphatic ones was observed, consistent with findings from ethanol-to-jet temperature studies over V-ZSM-5(23) [18]. This aromatic preference is primarily due to BAS facilitating protonation of intermediates, which promotes the formation of highly reactive carbocation species. These intermediates drive oligomerization and cyclization reactions, along with cracking and isomerization. Cycloaliphatics are inherently more stable than other aliphatic compounds and will remain, and further react under dehydrogenation, removing hydrogen from cycloaliphatics to form aromatics under high temperatures. This is known as thermal dehydrogenation and is favored at higher temperatures due to its endothermic nature [102]. However, LAS, introduced through metal-loading, such as indium, also enhances dehydrogenation by promoting redox reactions that facilitate hydrogen desorption and H_2 formation [103]. Additionally, literature suggests that although ethylene trimerization reactions, combining three ethene molecules to

one, is commonly used for to form 1-hexene [104], direct trimerization of ethylene to benzene is theoretically feasible [105]. This offers a possible additional route to aromatic formation.
Due to the high stability of benzene rings, once formed, aromatics tend to persist. They typically undergo alkylation and cracking, forming longer alkyl chains that later crack into shorter aliphatics. These include light olefins that re-enter the cycle of oligomerization, cyclization, aromatization, alkylation, and cracking [106].
Similarly, almost all paraffins were observed as isomers, with linear n-paraffins limited to short-chain species like n-pentane and below. This is attributed to the complex geometry of the ZSM-5 framework, which restricts diffusion of long linear chains, causing condensation and eventual polymerization into coke [42] [107]. Similarly, most olefins were detected as isomers, with only a few short-chain exceptions.

Catalyst Differences

As expected, H-ZSM-5(50) exhibited a higher aliphatic content than H-ZSM-5(23), due to its lower acidity and corresponding shift in selectivity toward the olefinic cycle. The total aliphatic yield for H-ZSM-5(50) was 30.09%, more than double that of H-ZSM-5(23) at 13.31%. The main contributors were cycloaliphatics and iso-paraffins, with olefin content increasing from 1.98% to 5.63%.

This increase in olefins also lead to increased olefinic alkylated products, in turn contributing to a lower H/C ratio, thus reducing fuel heating value and combusting quality. However, as hydrotreating is a standard process in jet fuel production, used for saturating double bonds, to increasing both the H/C ratio and heating value, an increase in olefinic species is not necessarily detrimental. However, hydrotreating is already required to reduce the olefins to avoid gum formation for all tested catalysts. Notably, the actual H/C has not been feasible to measure due to high volatility.

Among the metal-impregnated catalysts, Ni-ZSM-5(50) was the only one to yield fewer aliphatics than the unmodified H-ZSM-5(50), suggesting that nickel shifts selectivity back toward the aromatic cycle. While nickel is generally associated with increased oligomerization and dimerization, which would lead to longer paraffins and olefins, the data suggest that many of these intermediates undergo alkylation onto aromatic rings. This process is likely enhanced by the increase in Lewis acid sites due to nickel, which promote electrophilic aromatic substitution. This hypothesis is further supported by the HC chain length distributions shown in Figure 6.7 and is further discussed in Section 6.3.4

Cobalt-impregnated ZSM-5(50) yielded the highest concentration of aliphatic compounds among the tested catalysts, aligning with expectations and previous work by Stocker [91]. Consequently, it also showed the lowest selectivity toward BTX and other

aromatic species, due to the promotion of hydrogenation reactions. Thus, an increased amount of reactive olefins required for cyclization reactions is hydrogenated into non-reactive paraffins, which remain in the final product.

Indium-impregnated ZSM-5(50) demonstrated behavior intermediate between the nickel and cobalt variants. While it showed increased aliphatic production relative to the baseline H-ZSM-5(50), it was lower than that of cobalt. Interestingly, its olefin yield decreased, despite its supposedly increased selectivity towards dehydrogenation of light alkanes. This suggests that a majority of olefins underwent alkylation onto cycloaliphatics or aromatics or were hydrogenated to form longer-chained alkanes.

The comparison between the average and initial composition of each campaign is shown in Table 6.4, highlighting the development in product distribution as the catalyst gradually deactivates.

6.3.2 Differences Between Initial and Average Product Distribution

HC Class	H-ZSM-5(23)	H-ZSM-5(50)	Ni-ZSM-5(50)	Co-ZSM-5(50)	In-ZSM-5(50)
Average Yields Throughtout Campaign					
Cyclo-aliphatics	5.36	10.30	9.22	14.32	10.48
Iso-Paraffins	5.72	12.72	7.41	18.13	15.13
n-Paraffins	0.25	1.44	0.54	1.21	1.11
BTX	29.55	23.83	26.79	20.74	24.02
Other Aromatics	55.29	44.59	50.12	38.80	44.94
Oxygenates	0.60	0.48	0.54	0.42	0.48
Naphthalene	1.25	1.01	1.13	0.87	1.01
Olefins	1.98	5.63	4.26	5.51	2.83
Initial Yield at TOS = 2h					
Cyclo-aliphatics	0.35	2.18	2.64	10.27	4.41
Iso-Paraffins	1.35	12.98	6.12	18.06	13.38
n-Paraffins	0	2.02	0.69	2.89	1.58
BTX	60.53	27.69	38.46	32.73	34.93
Other Aromatics	32.63	47.56	44.62	31.98	41.60
Oxygenates	0.23	0	0	0.44	0
Naphthalene	2.95	5.61	5.44	0.35	2.13
Olefins	0	0	0	1.35	0

Table 6.4: Average product distribution over the lifetime of tested catalysts based on GC-MS peak area percentages.

Clear changes in product distribution are observed for the tested catalysts as the catalyst gradually deactivates. Here, the main shift from aromatics to aliphatics is observed

between all catalysts, primarily affecting the yield of cycloaliphatics, as it is the last intermediate before aromatization. This is to be anticipated with high acidity directly correlating to higher favorization of the aromatic cycle, as coke formation gradually deactivates the BAS, effectively lowering its acidity.

Initially, high yields of BTX are observed, especially for the most acidic catalyst H-ZSM-5(23). These are short-chain aromatics (C_6-C_8), and their abundance suggests active cracking of longer alkyl chains, enabled by the more substantial acidity in the early stages. As the catalysts deactivate, the yield of heavier aromatics increases, while BTX yield declines, indicating reduced cracking activity.

Naphthalene production is also initially higher for the more acidic catalysts, implying increased condensation of aromatics. Since naphthalene likely acts as a precursor to polyaromatic coke, its presence supports the link between high acidity and deactivation by the formation of hard coke. Notably, despite its higher acidity, H-ZSM-5(23) produces less naphthalene than H-ZSM-5(50) and the nickel-loaded variant. This may indicate that in strongly acidic environments, naphthalene undergoes further polymerization into larger, insoluble coke species, resulting in faster and harder deactivation. However, since H-ZSM-5(23) and H-ZSM-5(50) exhibit comparable lifetimes, the nature or impact of coke may differ between them, leaving the correlation inconclusive, warranting further investigation. The nature of the coke formation will be further discussed in Section 6.5.

With the exception of H-ZSM-5(23), the yield of paraffin, particularly iso-paraffins, remains relatively constant between initial and average distributions. This further suggests limited reactivity for paraffins. For H-ZSM-5(23), the very strong acidity likely converts nearly all olefins directly into the aromatic cycle, bypassing hydrogenation pathways that lead to paraffins. At weaker acidity, more olefins remain in the olefinic cycle, and paraffin formation may be governed by chemical equilibrium, limiting further conversion, independent of acidity change from gradual deactivation.

Interestingly, Co-ZSM-5(50) displays the most stable and consistent product distribution across TOS. The aliphatic yield only slightly increases, from 32.57% to 39.17%, compared to larger shifts seen in other catalysts, especially for cycloaliphatics. This suggests that cobalt incorporation provides a more controlled reaction pathway to products less susceptible to the changes caused by gradual catalyst deactivation, making it especially attractive for applications requiring consistent product output.

6.3.3 Development of Product Distribution

The following Figures 6.4, 6.5 and 6.6, highlights the development in selectivity as the catalyst gradually deactivates. The Figures have been split into the two categories,

including all the major HC classes in the ranges representative of LPG (C_1 to C_4, Gasoline (C_5 to C_8) and Jet fuel (C_9 to C_{16}). Additionally, oxygenates, BTX's and naphthalenes are also highlighted within the major HC classes as aforementioned. The aliphatic components are further categorized into the different aliphatic classes and the said ranges. Figure 6.4 illustrates the development for the two unmodified H-ZSM5(23) and H-ZSM5(50) catalysts.

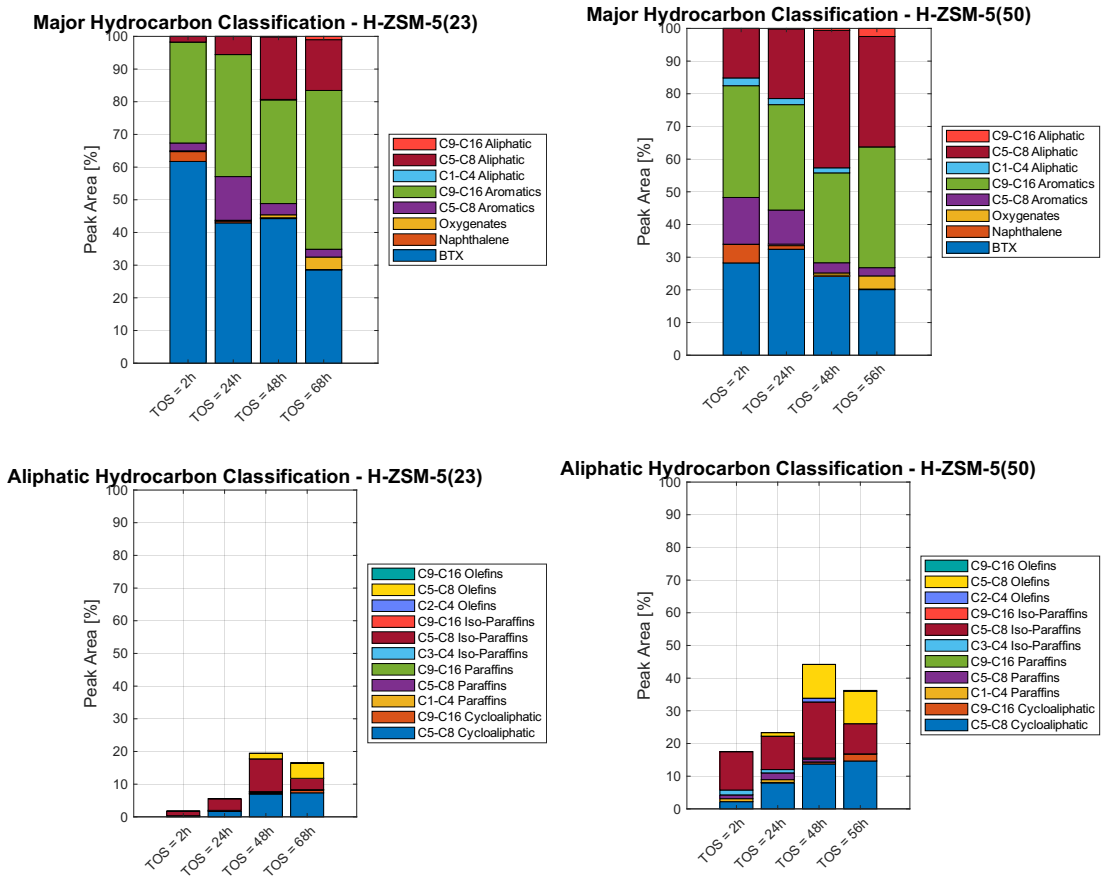

Figure 6.4: General HC classification and aliphatic HC classification through the life-time of the two unmodified catalysts H-ZSM5(23) and H-ZSM5(50), based on GC-MS peak area percentage

At longer time-on-stream (TOS), a decline in BTX components and a shift toward heavier aromatic species is observed, particularly for the higher-acidity H-ZSM-5(23). This trend likely results from catalyst deactivation, reducing cracking activity, and promoting the growth of longer alkyl chains. Alternatively, structural changes due to coke formation or irreversible deactivation may also contribute to the increased formation of heavier Hs.

A concurrent increase in gasoline-range aliphatic components is observed at higher

TOS for both catalysts. For H-ZSM-5(50), with its lower acidity, this shift highlights the enhanced selectivity toward the olefinic cycle and thus toward aliphatic products. At elevated TOS, the increased olefin selectivity further implies that reduced acidity limits the extent to which intermediates exit the olefinic cycle. In parallel, selectivity toward oxygenated species also rises, indicating their role as intermediates that are not fully deoxygenated under deactivated conditions. This further suggests that not all methanol is dehydrogenated to DME prior to undergoing subsequent reactions.

Interestingly, at the catalyst's end-of-life, at the highest TOS, selectivity toward aliphatic species decreases again, enhancing the formation of long-chain aromatics.

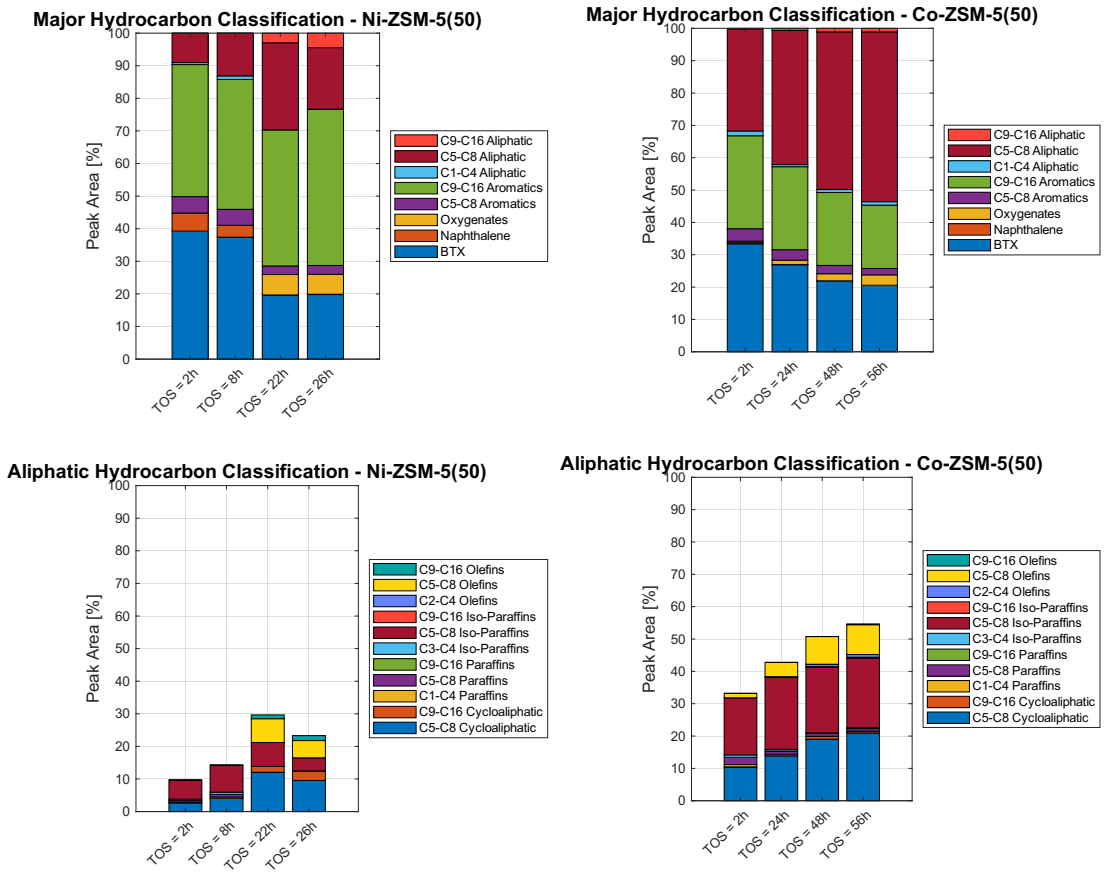

Figure 6.5: General HC classification and aliphatic HC classification through the life-time of the Ni-ZSM5(50) and Co-ZSM5(50), based on GC-MS peak area percentage

The Co-ZSM-5(50) and Ni-ZSM-5(50) catalysts exhibit similar trends to the unmodified H-ZSM-5 variants, particularly in the increased formation of heavier aromatic species relative to BTX components and concurrent increase in gasoline-range aliphatics. For Ni-ZSM-5(50), the high degree of deactivation is evident from the similar selectiv-

ity profiles at 22 and 26 hours TOS, especially in the oxygenate and olefin fractions. Notably, this catalyst also shows a slight increase in selectivity toward jet fuelrange olefins, suggesting the presence of oligomerization as a key intermediate pathway.

In contrast, the Co-ZSM-5(50) catalyst does not exhibit a decline in aliphatic selectivity, further implying that it may not have reached full deactivation under the tested conditions, unlike the other catalysts. Interestingly, it also displays a consistently higher selectivity toward gasoline-range olefins, even at low TOS, indicating a distinct catalytic behavior heavily favoring the olefinic cycle.

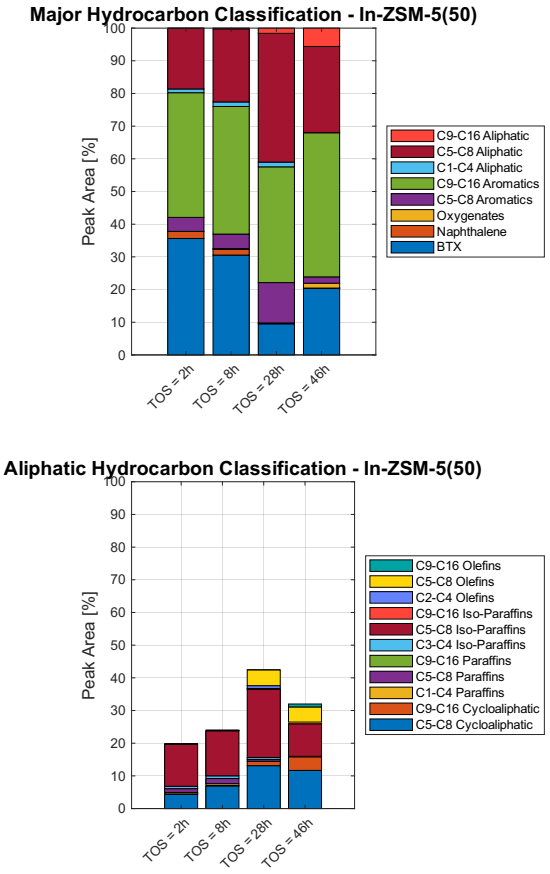

Figure 6.6: General HC classification and aliphatic HC classification through the life-time of the In-ZSM5(50), based on GC-MS peak area percentage

The indium-modified ZSM-5 displayed similar trends to the other tested catalysts. However, it uniquely exhibited increased selectivity toward jet fuelrange cycloaliphatics at higher TOS, suggesting intermediate behavior between the nickel- and cobalt-based catalysts. This may indicate a partial dehydrogenation of cyclic species, likely due to its reduced acidity.

6.3.4 Carbon Distribution of Tested Catalysts

To evaluate the influence of different catalysts on the resulting HC chain lengths, the peak areas of all identified compounds were grouped by carbon number and averaged over each campaign. The resulting distributions are shown in Figure 6.7. The primary goal is to shift the product distribution toward longer-chain HC, as these are more representative of the jet fuel range (C_9-C_{13}) compared to gasoline-range HC (C_5-C_8).

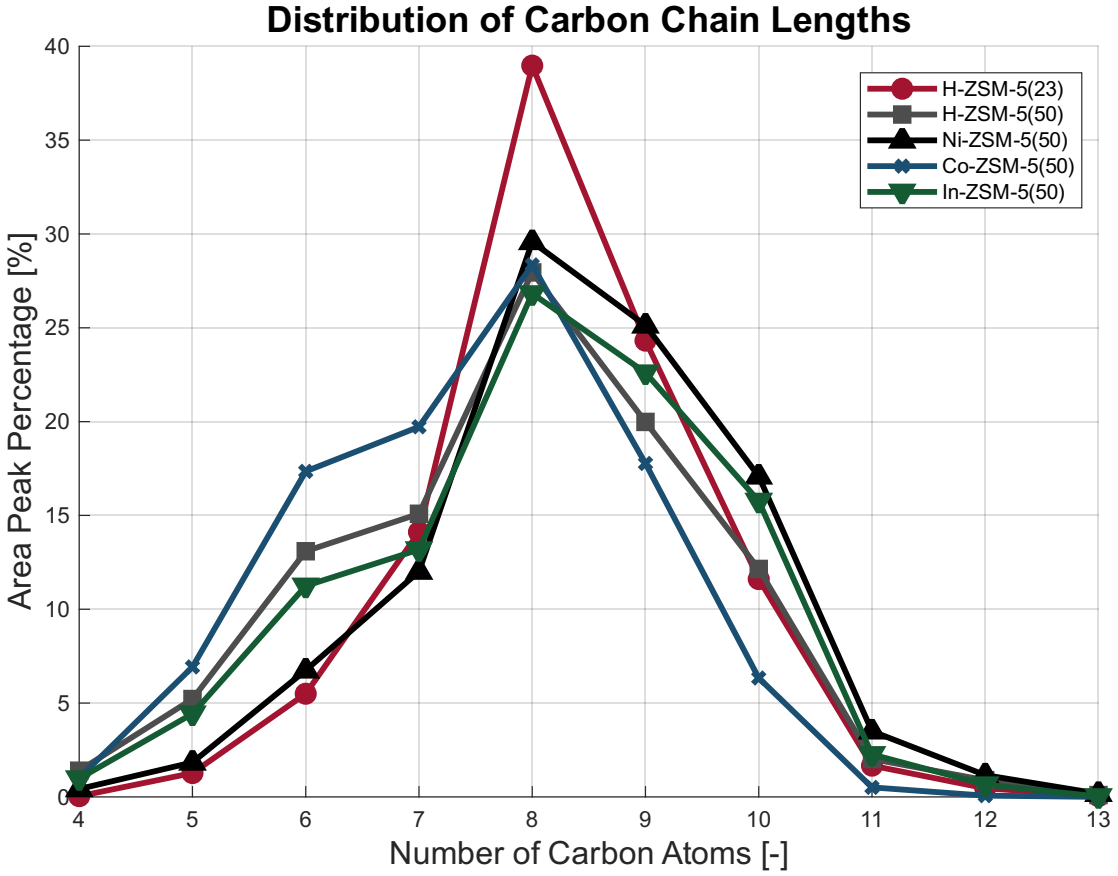

Figure 6.7: Carbon number distribution of tested catalysts.

Across all catalysts tested, the liquid products consistently fall within the C_4 to C_{13} range, with a general shift towards longer HCs for longer TOS, attributed to the formation of longer alkyl groups, caused by fewer cracking reactions, associated with the decreased acidity of the more deactivated catalyst. Any compounds below C_4 will appear within the gas phase, and compounds larger than C_{13} will generally be geometrically restricted by the catalyst's shape selectivity. The distribution indicates a peak between C_7 and C_9, indicating a preference for mid-range HCs, rationalizing its commercial use for primarily gasoline production. Notably, C_8 shows a pronounced peak, particularly for the H-ZSM-5(23) catalyst, which is composed mainly of aro-

matic compounds such as xylenes and ethylbenzene. Chemeurope generally suggests that xylene has a lower formation enthalpy than benzene and toluene, further indicating xylene as a more stable product. [108, 109]. Comparing the two baselines, H-ZSM-5(23) and H-ZSM-5(50), the pronounced C_8 peak, particularly in the more acidic H-ZSM-5(23), is thus believed to be attributed to C_8 aromatics striking an optimal balance between thermodynamic stability and molecular size, allowing them to diffuse efficiently through the ZSM-5 pore system and thereby minimize secondary reactions such as cracking or long chain alkylation.

The addition of Ni to H-ZSM-5(50) resulted in a shift toward longer carbon chains. This is consistent with nickel's known promotion of oligomerization and dimerization reactions, which facilitates the growth of longer olefins that can attach to cyclic or aromatic rings to form larger molecules. Subsequently, the yield of short HCs decreases, following that of H-ZSM-5(23), with a decreased peak of C_8 molecules and increased distribution of larger molecules.

Interestingly, In-ZSM-5(50) produces a broader and more evenly distributed carbon number profile. This suggests a dual role of indium in promoting both growth and cracking pathways, making both aromatic and aliphatic pathways accessible without a strong bias toward either, making indium an intermediate between nickel and cobalt.

Overall, these trends highlight how the catalysts acidity and metal functionality influence the chain length distribution, depending on whether the olefinic or aromatic cycle is favored.

6.4 Simulated Distillation

Correlated to the HC length distribution, SimDist was used to estimate the actual fractional distillation and evaluate the suitability of the liquid HCs for jet fuel and other fuel applications. SimDist estimates the fractional distillation behavior of the produced HCs by correlating boiling point distributions with the HC chain lengths. The ASTM D2887 method was utilized, which uses a gas chromatography (GC)-based approach with a programmed temperature ramp to determine the boiling point distribution of a sample within room temperature and 537 °C (1000 °F).
ASTM D2887 is calibrated utilizing a series of n-paraffins, which exhibit relatively lower boiling points than the aromatics and cycloaliphatics contained within the samples, as identified through GC-MS. This discrepancy introduces systematic errors in the estimation of boiling points for non-paraffinic species, potentially leading to a slight overestimation of the boiling points compared to the true boiling points. [110] [111].
The key fuel fractions were defined by the following boiling point intervals: 0-80 °C

for LPG, 80-150 °C for gasoline, 150-280 °C for jet fuel, and 280-350°C for diesel. The SimDist results for all tested catalysts are shown in Figure 6.8, with recovered HC fractions expressed as wt.%.

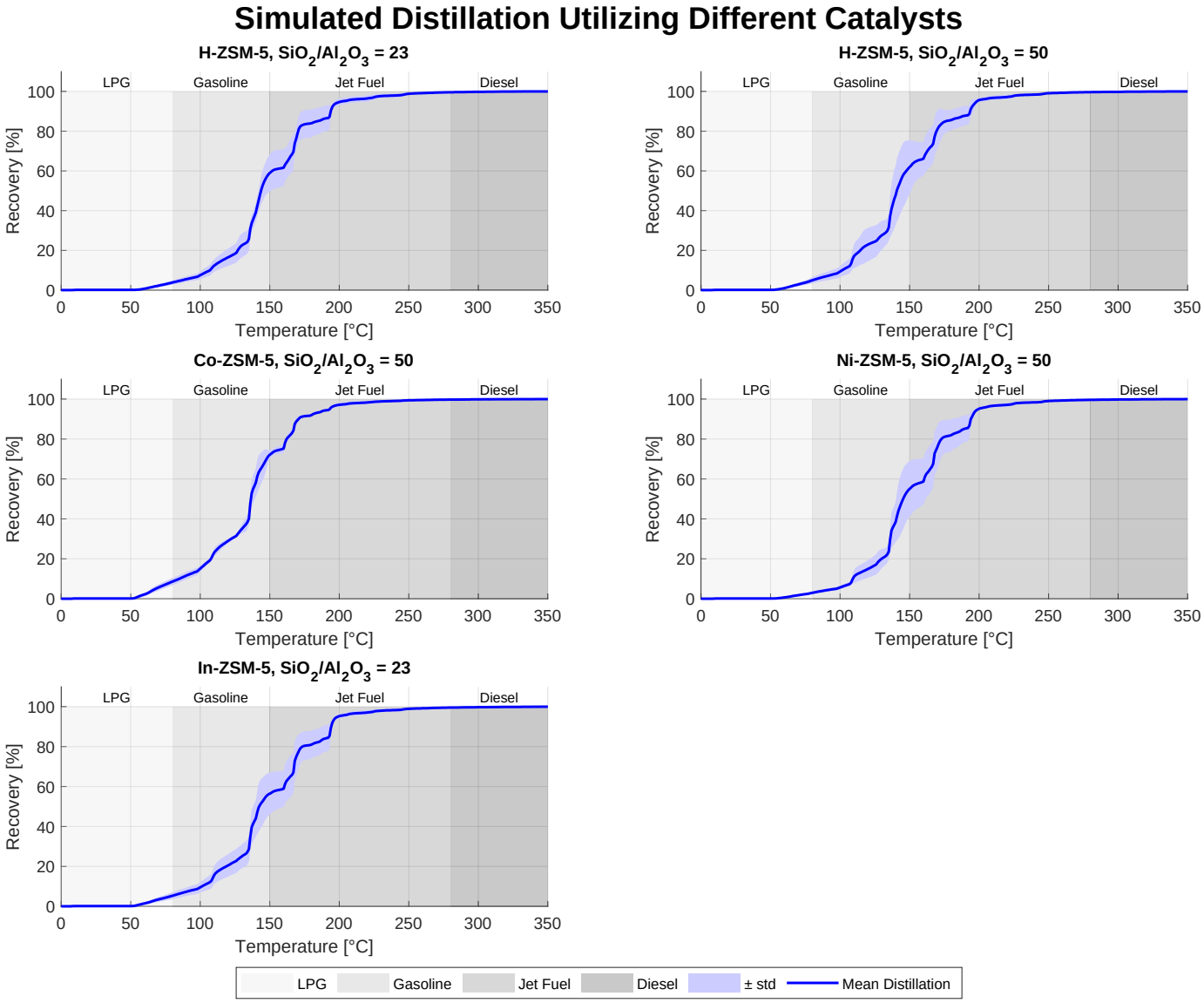

Figure 6.8: Mean simulated distillation for collected samples of all tested catalysts and their standard deviations.

To illustrate the impact of catalyst deactivation at higher TOS, the average composition of the collected samples is plotted alongside the standard deviation to represent the variability throughout the campaign. A consistent trend of increasing jet fuel fraction with longer TOS is observed for all catalysts. This could be explained by the suppres-

sion of cracking reactions at reduced acidity, and thus acidity, resulting in the growth of longer alkyl side chains onto the cycloaliphatic and aromatic compounds. Table 6.5 summarizes the cumulative recovery and its standard deviation at the boiling point cutoffs, further highlighting the evolution of product distribution over time.

Catalyst	LPG [wt.%]	Gasoline [wt.%]	Jet Fuel [wt.%]	Diesel [wt.%]
H-ZSM-5(23)	3.81 ±1.05	55.18 ±9.34	39.13 ±0.91	1.88
H-ZSM-5(50)	4.93 ±1.53	57.00 ±13.44	37.30 ±0.15	0.37
Co-ZSM-5(50)	8.59 ±1.78	63.55 ±2.27	27.62 ±0.32	0.23
Ni-ZSM-5(50)	2.96 ±0.68	52.08 ±13.95	44.61 ±0.15	0.35
In-ZSM-5(50)	5.28 ±1.68	51.19 ±10.45	43.11 ±0.04	0.42

Table 6.5: Recovered product fraction at the temperatures defining the boiling ranges of LPG, gasoline, jet fuel, and diesel. Values are given in wt.% with standard deviations indicated by ±

The distribution of recovered product fractions, determined via simulated distillation, aligns with the HC chain length trends discussed in Section 6.3.4, of which the catalyst producing longer-chained HCs exhibits the highest yields of jet fuel. Here, the highest fraction of recovered jet fuel was observed for Ni-ZSM-5(50), at approximately 44.6 wt.%, corresponding to the longer HCs produced by increased oligomerization and dimerization reactions, followed closely by In-ZSM-5(50) at 43.1 wt.%. The two unmodified ZSM-5 catalysts also exhibited significant jet fuel production, with H-ZSM-5(23) reaching 39.1 wt.% and H-ZSM-5(50) at 37.3 wt.%. In contrast, Co-ZSM-5(50) produced the lowest jet fuel fraction at 27.6 wt.%, instead favoring the gasoline-range HCs, due to its higher selectivity towards the aliphatic cycle, producing shorter HCs. These values were used to estimate the amount of representative compounds within each boiling range of the distillation model described in Chapter 7.

Notably, Co-ZSM-5(50) exhibited the lowest standard deviation at the cutoff range between gasoline and jet fuel at 150 °C of just 2.27 wt.%, in contrast to the >10 wt.% variations observed for the other catalysts, further indicating its stable product distribution over time.

6.5 Thermogravimetric Analysis of Coke Deposits on Spent Catalyst

Full deactivation was observed for all ZSM-5based catalyst campaigns, except for Co-ZSM-5, which was terminated prematurely at a liquid yield of nearly 30% of the theoretical maximum. The coke deposits on the spent catalyst pellets from each campaign are shown in Figure 6.9.

Figure 6.9: Spent catalyst of the experimental campaigns of Beta-zeolite, H-ZSM-5(23), H-ZSM-5(50), Ni-ZSM-5(50), Co-ZSM-5(50) and In-ZSM-5(50)

Notably, the Beta-zeolite (far left in the figure) shows significant signs of coke deposition despite its campaign being halted after only approximately 30 minutes of TOS. A clear variation in the extent and appearance of coke deposits is evident across the catalysts. H-ZSM-5(23) shows the darkest deposits, indicating heavier coke formation, while the cobalt-modified catalyst exhibits much lighter deposits. These differences suggest that catalyst deactivation is linked to the nature of coke species formed, which in turn is influenced by the product selectivity of each catalyst.

Thermogravimetric analysis (TGA) was thus employed to investigate the nature of coke deposits on spent catalysts and determine the temperature intervals relevant for catalyst regeneration. Each TGA experiment was performed on three separate samples of spent catalyst to account for sample variations, and standard deviations were calculated to reflect measurement variability. A fresh, unreacted catalyst pellet was also included as a reference. All measurements were conducted under a constant airflow to ensure oxidative conditions, with a linear temperature ramp of 10 °C/min and no isothermal holding period. Due to unforeseen instrument failure, TGA measurements could not be completed for all spent catalysts.
Coke formed during methanol conversion generally falls into two categories: soft coke and hard coke, which are distinguished by their chemical structure and reactivity. Soft coke typically consists of condensed aliphatic species and confined oligomers, while hard coke is dominated by polyaromatic HCs with higher thermal stability [112]. Although definitions vary in the literature [113], this study adopts the following operational classification based on combustion temperature:

- **0-200 °C:** Volatile components (e.g., physisorbed water, light organics)
- **200-400 °C:** Soft coke (aliphatic oligomers and light condensed HCs)
- **400-600 °C:** Hard coke (primarily polyaromatic species)

- **600-800 °C:** Non-volatiles (graphite-like, highly condensed polyaromatics) [114, 115]

Figure 6.10 presents the TGA results for the three catalysts studied.

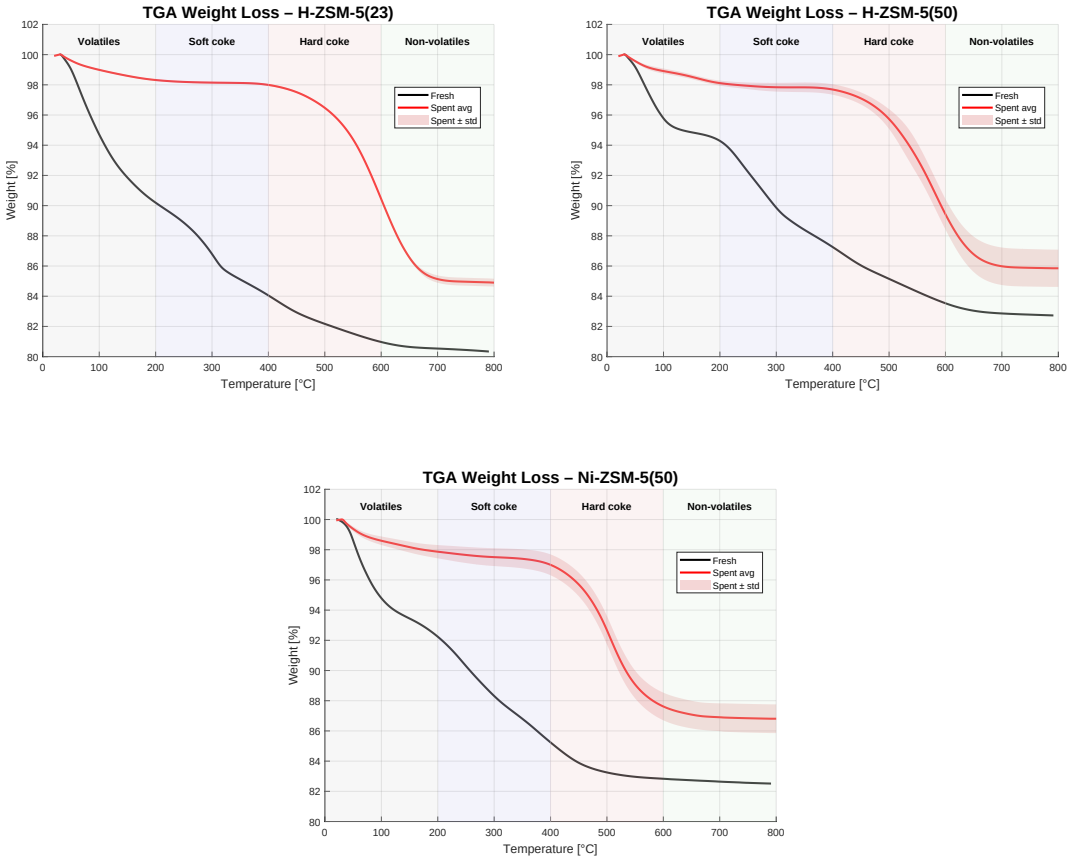

Figure 6.10: TGA results of H-ZSM-5(23), H-ZSM-5(50) and Ni-ZSM-5(50)

An interesting observation is the significant mass loss of the fresh, unreacted catalyst across the temperature range. While initial weight loss in the volatile region is expected due to moisture desorption [115], further weight reduction observed in the soft and hard coke regions is less intuitive. This is likely attributed to the presence of organic cellulosic binders in the catalyst, which begin to decompose thermally in the range of 250-500 °C [116]. Unfortunately, testing a binder-free reference sample was not feasible due to equipment failure, so this hypothesis remains unconfirmed.

Notably, the spent samples of H-ZSM-5(50) and Ni-ZSM-5(50) showed larger standard deviations between replicates, possibly due to spatial variation within the reactor bed, affecting the coke formation greater for lower acidities. However, this is not conclusive, as the exact location of spent catalyst samples remains unknown. The summary of

weight losses in each temperature-defined coke region is provided in Table 6.6.

Catalyst	Volatiles	Soft Coke	Hard Coke	Non-Volatiles
H-ZSM-5(23)	1.60	0.32	7.53	5.47
H-ZSM-5(50)	1.77	0.42	8.24	3.52
Ni-ZSM-5(50)	2.07	0.86	9.37	0.80

Table 6.6: Average weight loss wt.% due to oxidation of volatiles, soft coke, hard coke, and non-volatiles for each of the tested spent catalyst.

Across all tested catalysts, hard coke constitutes the dominant fraction of the total weight loss. In contrast, soft coke is present only in small amounts, implying it either does not accumulate or is further converted to hard coke or cracked into volatiles.

Interestingly, the impregnation of nickel in Ni-ZSM-5(50) appears to reduce the fraction of non-volatile, graphite-like coke. From a regeneration perspective, this is advantageous as it reduces the need for high-temperature oxidation, thereby reducing energy requirements and thermal stresses on the catalyst.

Although coke deposits on cobalt- and indium-impregnated catalysts were not investigated, it is anticipated that cobalt, in particular, would exhibit a higher proportion of soft coke due to its increased selectivity towards aliphatic compounds. However, since this was not experimentally tested, the extent and nature of coke formation remain uncertain.

6.6 Results and Discussion

The different catalysts demonstrated unique strengths and limitations throughout the experimental campaigns. Nickel exhibited the highest yield of jet fuel, achieving 44.6 wt.%. However, this was accompanied by a notably short catalyst lifetime, falling below 20 hours, and a relatively lower yield of aliphatic HCs compared to the other catalysts.
Cobalt stood out for its improved stability, achieving a slightly longer lifetime than the unmodified zeolite while maintaining a consistent yield. It also showed a notable increase in the aliphatic fraction of the HC products, which could enhance its potential as a jet fuel blendstock. However, cobalt also significantly reduced the average carbon chain length of the products, due to its favorization of the olefinic cycle, leading to a smaller fraction falling within the traditional jet fuel distillation range between 150-280 °C. Instead, the product profile was skewed toward the gasoline range, suggesting its suitability for blending into aviation gasoline, such as Jet B.
Indium displayed intermediate characteristics relative to nickel and cobalt. Its HC distribution, lifetime, carbon number profile, and jet fuel fraction all fell between the two.

Notably, almost all produced aliphatic species were in the range of gasoline, with few exceptions for the indium variant, indicating a low selectivity towards cycloaliphatic compounds at extended TOS. This likely suggests the framework of ZSM-5 does not allow for the formation of long aliphatics, but relies on the cyclic rings and an attached alkyl group for the formation of heavier HCs.

One aspect not investigated in this work is the effect of Le Chateliers principle. In theory, increasing the reactor pressure could shift the equilibrium toward the formation of longer, heavier HCs, favoring the jet fuel range, since fewer, larger molecules occupy less total volume than many smaller ones. This could potentially enhance jet fuel yields and warrants further investigation.

It is also important to note that experimental yields, particularly gas yields, were calculated under the assumption of 100% methanol conversion, corresponding to findings within the literature [96]. However, since the aqueous phase was not analyzed, the actual extent of methanol conversion and its correlation with catalyst activity remain unknown. Furthermore, toward the end-of-life of the catalysts, clear signs of unconverted methanol in the aqueous phase were observed, including a strong methanol odor and a cloudy appearance, coinciding with a significant drop in liquid product yield.

Attempts to conduct an experimental campaign using H-Beta zeolite failed due to operational issues. In both attempts, the pre-cooler clogged after approximately 30 minutes of run time, likely due to condensation of large aromatic compounds with high melting points. Although only a small initial product sample was collected, GC-MS analysis indicated a high selectivity towards large methylbenzenes, including tetra-, penta-, and hexa-methylbenzene, all of which have high melting points above 80°C and, thus, are believed to condense in the pre-cooler operating at atmospheric temperatures [117].

At the start of each experiment, the first hour of HC production was discarded. This was done to disregard any accumulation within the reactor and approach steady-state conditions. However, due to the relatively low pre-heater temperature of 200°C, the upper section of the reactor likely operated below the set reactor temperature of 350°C initially, resulting in an unrepresentative product distribution, prior to early catalyst deactivation.

A considerable source of experimental uncertainty was the lack of gas-phase analysis. Due to the delayed delivery of the calibration gas mixture for the gas chromatograph, which included olefins, paraffins, and permanent gases, the gas-phase products were not quantified. This limited the ability to evaluate how each catalyst influenced gaseous selectivity. Insights into the selectivity towards hydrogenation of short olefins

and the formation of paraffins were thus not possible. Furthermore, an insight into the extent of cracking reactions and the formation of odd-carbon-number HCs such as propene, which cannot be formed by ethylene oligomerization, was therefore not possible. These analyses could have provided valuable information about the reaction pathways and the mechanisms specific to each catalyst.

Chapter 7

Experimental-Based Methanol-to-Hydrocarbon Model

Experimental analysis through GC-MS, revealed that chemical composition of of the produced liquid HC, changes significantly based on the utilized catalyst. Furthermore, SimDist analysis showcased that some catalysts yielded higher recovery within the jet fuel range compared to others. To investigate how the recovery affects the required energy requirements, a experimental based MTH model has been developed. This model will aim to quantify the overall carbon -and hydrogen conversion from producing the CO_2 in the MEA CC process, to the kerosene produced, based on gathered data from laboratory (lab) experimental results. The model will likewise also aim to quantify the various tested catalysts, in their performance of producing kerosene and fuel in general.

7.1 Methanol to Hydrocarbon Synthesis Model

The model is constructed in Aspen Plus and utilizes a "RYIELD" reactor to simulate the products produced in the lab, since SimDist curves predetermine the output of this block. The MTH model can be seen in Figure 7.1

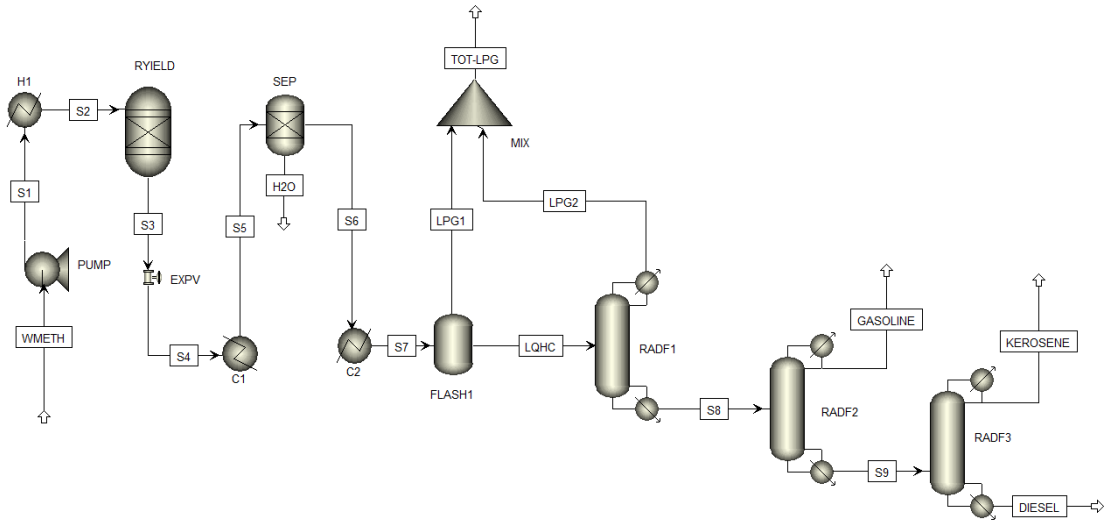

Figure 7.1: Aspen Plus MTH model based on experimental results

The MTH model features a feed stream "WMETH" which represents the product stream from the methanol synthesis model, with a mass fraction of 64/36 MeOH/H_2O, respectively. This stream is pressurized to 2 bar via a pump and preheated to 350°C

via "H1" before it enters the reactor "RYIELD". Here, the output is specified based on experimental results from the SimDist and GC-MS in Chapter 5. Due to limitations, direct determination of the chemical composition of the gas phase was not possible. Therefore, its composition was estimated based on data from analogous experiments using comparable catalysts. The utilized gas composition can be see in Table 7.1

Compound	Mass Fraction [%]	Description
CH_4	16.49	Methane
C_2H_6	10.33	Ethane
C_3H_8	10.33	Propane
C_4H_{10}	6.26	Butane
C_2H_4	10.44	Ethene
C_3H_6	25.47	1-Propene
C_4H_8	20.67	1-Butene

Table 7.1: Chemical composition of the gas phase utilized in the MTH Aspen Plus Model. [118] [119]

GC-MS results exhibited that the produced liquid HC mixture consisted of paraffins, iso-paraffins, olefins, cyclo-aliphatics, and aromatics. Therefore, to mimic the behaviour of the compounds produced from the experiments, a variety of compounds have been chosen. These compounds can be found in Table E.1 in Appendix E. These compounds were selected to represent successive boiling point intervals of 20 °C, covering a total range from 20 °C to 300 °C. The compounds undergo distillation over a 20 °C temperature interval, during which a portion of the total mass is recovered based on their volatility, enabling the quantification of typical fuel fractions, such as LPG, gasoline, kerosene, and diesel, that are commonly produced through fractional distillation.
From Section 6.2, it was found that during reaction in the reactor for all experiments, the temperature increased from the original 350 °C. Depending on the catalyst used, the observed temperature increase was from 10 to 60 °C in different locations inside the reactor. To account for this exothermic observation, the outlet temperature of the "RYIELD" was set based on the total average temperature in the reactor of the active catalyst region. The utilized temperature for the outlet streams for the different catalysts can be seen in Table 7.2. The product stream from the "RYIELD" reactor is then expanded to 1.013 bar, and cooled to 25°C. The water is afterwards removed in the "SEP" block, and the liquid and gas HC are sent into a cooler "C2". In this step, the mixture is cooled to a temperature corresponding to a defined liquid-to-gas ratio, as specified by process design criteria. This temperature is selected such that the vaporliquid equilibrium ensures no more than 4 wt.% of gasoline-range HCs are carried over into the LPG product stream. [120]. An allowance of maximum of 4 wt.% heavy fraction in the light fraction is utilized based on regulations and guidelines from the *Occupational Safety and Health Administration* (OSHA)[121]. Afterwards, the liquid and

the gas are separated in a flash tank, where the liquids are then further sent on to distillation. Here, it is separated in a three-stage separation process, where the remaining LPG is first separated, followed by gasoline, and lastly, by kerosene and diesel.

The compounds chosen to mimic the compounds produced in the lab, is chosen based on boiling point and chemical composition. However, it is almost impossible to determine the exact same compounds in a mathematical model. Therefore, to determine how good a representation the chosen compounds are, the carbon and hydrogen efficiency η_C and η_H, respectively, are determined.

	H-ZSM-5(23)	**H-ZSM-5(50)**	**Ni-ZSM-5(50)**	**Co-ZSM-5(50)**	**In-ZSM-5(50)**
T_{avg} Reactor [°C]	362.69	359.53	368.00	357.51	356.58
η_C	93.09	91.31	92.29	88.33	92.57
η_H	103.59	103.29	103.35	102.70	103.59

Table 7.2: Exothermic temperature input based on experimental observations, actual carbon and hydrogen conversion

Table 7.2 presents that the η_C undershoots the amount of carbon present in the liquid phase, compared to the amount of carbon entering the system through methanol. The opposite indication seen in the η_H where the amount of hydrogen is higher than the amount of hydrogen sent into the system. These observations likely indicate a mismatch in the atom balance, which is also almost impossible to uphold, since exact reactions are not specified. Furthermore, it also indicates that the chosen representative compounds do not completely fit the conversion. Additionally, the relation between η_H and η_C indicates that the chosen compounds also have a lower H/C ratio, compared to the actual product. To account for these deviations, the η_C and η_H are normalized to assume total conversion to these compounds in the model.

7.1.1 Distillation Parameters

The distillation process utilizes three separate RadFrac columns, which act as a distillation tower. However, due to complexity and more strict convergence criteria, a simpler DSTWU column is used as an initial guess. This DSTWU is a simpler and more stable column compared to the RadFrac. However, the DSTWU, struggles to determine the correct energy requirements, which is why it is used as an initial guess for the RadFrac column. The input parameters for the three RadFrac columns can be found in Table E.3 in Appendix E.1. The radfrac conditions are based on the recovery percentages on some of the compounds presented in Appendix E, each representing a boiling range. The recovery, of the three "RADFRAC" columns can be seen in Table 7.3

	Light Component	Boiling Range [°C]	Recovery	Heavy Component	Boiling Range [°C]	Recovery
RADFRAC1	C_6H_{14}	60-80	0.95	C_7H_{16}	80-100	0.04
RADFRAC2	C_9H_{20}	140-160	0.95	$C_{10}H_{22}$	160-180	0.04
RADFRAC3	$C_{16}H_{34}$	280-300	0.95	$C_{17}H_{36}$	300+	0.04

Table 7.3: Recovery of the radfrac distillation columns used in the MTH model

In addition to OSHA recommendations, allowing up to 4 wt.% of heavy components in the light fraction is based on energy considerations. Reducing the heavy content further would require increased reflux, leading to higher energy consumption in both the condenser and reboiler.

Furthermore, since LPG in liquid form is not desired, a partial condenser in "RADFRAC1" has been chosen to allow all vapor distillate. This reduces the required cooling duty of that specific condenser, since the majority of the products in the stream have boiling points below -20 °C. To remove the requirement for additional coolers in the system, the condensers in "RADFRAC2" and "RADFRAC3" have been chosen to be total condensers, which result in 100% liquid distillate. The input parameters for the three radfrac columns based on each catalyst can be seen in Table E.2 in Appendix E.1.

To ensure consistency, all the tested catalysts utilize the same distillation conditions. Depending on the mixture of HC, more or less reflux is needed to ensure the recovery design parameters presented in Table 7.3, are upheld. Furthermore, since the inputs from the "DSTWU" columns only act as an initial guess, design specs have been set for all three radfracs. These design specs ensure that the maximum amount of heavy fraction in each of the light fraction streams is restricted to 4 wt.%. A comparison analysis has been made to see the catalytic effects on the required duty for the separation process. To see the effects of the different catalysts on the conversion of methanol to HC, a catalytic comparison has been made.

7.2 Results and Energy Requirements

From the MTH synthesis model, water, LPG, gasoline, and kerosene are all products from the conversion process of wet methanol to kerosene. The model assumes 100% conversion of methanol through the reactor at optimal conditions, where the catalyst is not deactivated [96]. The kerosene production is highly dependent on the type of catalyst utilized, since it affects the chemical composition of the liquid HCs produced. To get a better understanding of the catalytic selectivity towards compounds in the kerosene range, a catalyst comparison has been made.

This comparison aims to evaluate the catalytic performance on various parameters,

such as selectivity towards compounds in the kerosene range, η_C, η_H, and energy requirements for separation into LPG, gasoline, kerosene, and diesel. In Table 7.4, the selectivity towards the different products, carbon conversion from CO_2 to both liquid HC and to kerosene, and the required duty can be seen.

Parameter	Unit	H-ZSM-5(23)	H-ZSM-5(50)	Ni-ZSM-5(50)	Co-ZSM-5(50)	In-ZSM-5(50)
			Key Parameters			
$\eta_{C\rightarrow Lq_{HC}}$	[%]	38.62	41.24	41.93	40.24	36.72
$\eta_{C\rightarrow Kerosene}$	[%]	13.52	11.60	16.69	8.85	14.66
$\eta_{H\rightarrow Lq_{HC}}$	[%]	14.18	14.74	15.53	13.34	13.17
$\eta_{H\rightarrow Kerosene}$	[%]	4.68	3.93	5.83	2.94	5.06
LPG	[kg/hr]	5935.55	5939.71	5568.98	5484.65	6087.16
Gasoline	[kg/hr]	1970	1947.38	2064.61	2329.86	1716.69
Kerosene	[kg/hr]	1275.85	1072.74	1563.03	794.58	1376.50
Diesel	[kg/hr]	379.52	396.67	274.75	446.69	329.38
Exp Lq/Gas Ratio	[kg/kg]	0.753	0.697	0.852	0.782	0.706
Sim Lq/Gas Ratio	[kg/kg]	0.611	0.575	0.701	0.651	0.562
			Energy requirements			
PUMP Duty,W_{PUMP}	[kW_e]	1.28	1.28	1.28	1.28	1.28
H1 Duty,Q_{H1}	[kW_{th}]	22704.9	22704.9	22704.9	22704.9	22704.9
C1 Duty,Q_{C1}	[kW_{th}]	-25065.2	-25034.2	-25212.1	-25171.3	-24873.3
SEP Duty,Q_{SEP}	[kW_{th}]	-43.87	-47.83	-45.47	-43.30	-43.35
C2 Duty,Q_{C2}	[kW_{th}]	-211.71	-62.97	-25.82	-100.96	-53.02
			RADFRAC1			
Condenser Duty,Q_{RC1}	[kW_{th}]	-242.22	-116.23	-112.14	-140.58	-101.96
Reboiler Duty,Q_{RR1}	[kW_{th}]	741.30	398.60	431.07	451.19	389.61
			RADFRAC2			
Condenser Duty,Q_{RC2}	[kW_{th}]	-387.16	-368.32	-427.49	-408.41	-336.63
Reboiler Duty,Q_{RR2}	[kW_{th}]	427.12	410.86	467.15	450.35	379.44
			RADFRAC3			
Condenser Duty,Q_{RC3}	[kW_{th}]	-129.96	-108.21	-154.58	-86.68	-137.34
Reboiler Duty,Q_{RR3}	[kW_{th}]	157.09	136.11	174.70	117.78	161.04

Table 7.4: Results from the MTH synthesis model, including key parameters, and heat requirements for all tested catalysts.

To compare the performance of the empirical model to the experimental results, a Lq/Gas ratio is utilized. This parameter is based on the amount of product exiting in the gas stream compared to the liquid stream, which is also defined in Equation (7.1)

$$Lq/Gas = \frac{\dot{m}_{\text{Liquid}}}{\dot{m}_{\text{Gas}}} \tag{7.1}$$

This ratio provides additional information related to the compounds chosen to rep-

resent the liquid and the gas mixture. It can be seen from Table 7.4, that deviations between the simulated Lq/Gas ratio and the experimental Lq/Gas ratio exist. These discrepancies arise from the normalization of compounds used to represent both gas and liquid compositions. Additionally, the experimental gas composition, unlike the simulated one, is not accounted for, which further contributes to the deviations.

From Table 7.4 it can be seen that the type of catalyst has a significant impact on the production of kerosene. Ni-ZSM-5(50) and In-ZSM-5(50) present a slightly higher conversion to compounds in the kerosene range compared to H-ZSM-5(23), H-ZSM-5(50), and significantly more than Co-ZSM-5(50). By looking further at Ni-ZSM-5(50), it can be seen that both the η_C and η_H for both products in the liquid HC range, but also the kerosene, is superior compared to any of the other catalysts. Looking at Co-ZSM-5, its selectivity towards compounds in the kerosene is lacking behind some of the other, with higher selectivity towards compounds in the gasoline range. Looking at the different catalysts' selectivity towards compounds in the kerosene range, they range from 8.77% to 16.50%, with Co-ZSM-5(50) and Ni-ZSM-5(50) being suboptimal and superior, respectively. From Section 6.3.2 it was also presented that cobalt, was significantly more selective towards aliphatics in the gasoline range. This is also what is seen in the MTH model, with Co-ZSM-5(50) having a selectivity towards compounds in the gasoline range of 25.73%. All tested catalysts tend to have similar selectivity towards compounds in the gas phase. This selectivity ranges from 58.80% to 64.01% with Ni-ZSM-5(50) being the least selective towards compounds in the LPG range, and In-ZSM-5(50) being the most.

As shown in Table 7.4, the initial preheating of the feed stream and the subsequent cooling of the product stream account for the majority of the total heat duty. However, since these utilities are comparable in magnitude, but opposite in thermal direction, a heat integration strategy may be feasible, with one stream requiring heating and the other cooling. This opportunity for heat recovery is discussed further in Chapter 8. Furthermore, it can also be seen that the separation column requires a cooling duty, even though the temperature does not change. This is due to the phase change of the mixture, changing from mostly liquid to mostly gas during the removal of water. Additionally, the radfrac separation columns indicate similar operational trends across all catalysts. Nevertheless, differences in product composition result in some catalysts demanding significantly higher reboiler and condenser duties.

All of the processes described previously require heating and cooling to some extent, with some requiring significantly more than others. A heat integration analysis has been made to investigate the possibility of heat integration between all of the described processes, potentially co-locating them next to one another, to increase the system's overall efficiency.

Chapter 8

Heat Integration

Most industrial processes involving heating and cooling incorporate some degree of heat integration to improve energy efficiency. Whether implemented internally, within a single process, or externally, between separate processes, heat integration often leads to reduced utility consumption and economic benefits. This is typically executed through pinch analysis, which is used to identify the minimum external energy requirements to operate a system, through internal or external energy utilization.

This chapter examines the potential for co-locating the MEA CC model, the AWE model, the methanol synthesis, and the experimental MTH model, to enable the recovery and reuse of excess heat, such as from heaters or coolers, in other parts of the system. The analysis focuses on identifying feasible opportunities for heat recovery, rather than developing a complete heat exchanger network.

Stream	Supply Temperature [°C]	Target Temperature[°C]	Duty [MW_{th}]	Description
Anime-based MEA Carbon Capture Model				
RICHSOL2	52.3	107	42.732	Pre-heater
LEANSOL1	119.4	40	-47.626	Post-cooler
CO2H2O	105.0	25	-14.790	CO_2 Condenser
RICHSOL3	107	119.4	29.105	Reboiler
Alkaline Water Electrolysis Hydrogen Production Model				
S15	75.0	71.0	-75.0	Recirc Cooler
OUT-CA	75.0	25.0	-1.618	H_2 Flash
OUT-AN	75.0	25.0	-0.835	O_2 Flash
Methanol Synthesis Model				
$MSC1_{Stage1}$	95.42	25	-1.24	Intercooling
$MSC1_{Stage2}$	95.48	25	-1.24	Intercooling
$MSC2_{Stage1}$	121.05	25	-0.77	Intercooling
$MSC2_{Stage2}$	140.19	25	-0.97	Intercooling
S3	103.10	220	1.173	Post-mixing
PROD	262.3	25	-80.217	Post-reaction
S8	28.7	220	47.989	Post-compression
Methanol-to-HC Synthesis Model				
S1	25	350	22.704	Pre-heater
S4	360.22($\pm$4.64)	25	-25.07($\pm$0.13)	Post-cooler
S5	25	24.9	-0.045($\pm$0.002)	Sep-Unit
S6	25	12.19($\pm$4.29)	-0.090($\pm$0.07)	Post-Sep cooler
$RADFRAC1_{Cond}$	62.05($\pm$1.08)	35.79($\pm$3.16)	-0.143($\pm$0.057)	Pre-condenser
$RADFRAC1_{Reb}$	139.35($\pm$4.40)	139.46($\pm$4.03)	0.482($\pm$0.146)	Pre-reboil
$RADFRAC2_{Cond}$	135.99($\pm$2.39)	126.42($\pm$2.60)	-0.386($\pm$0.035)	Pre-condenser
$RADFRAC2_{Reb}$	191.51($\pm$3.31)	191.61($\pm$3.28)	0.427($\pm$0.034)	Pre-reboil
$RADFRAC3_{Cond}$	208.28($\pm$3.23)	183.73($\pm$0.41)	-0.123($\pm$0.026)	Pre-condenser
$RADFRAC3_{Reb}$	301.09($\pm$0.04)	301.19($\pm$0.04)	0.149($\pm$0.022)	Pre-reboil

Table 8.1: Required heating and cooling during MTH synthesis model for all tested catalysts. All units are in kW

A notable key takeaway is that during the MSC in the methanol synthesis, the temperature increases, and is cooled through intercooling. However, after the last stage, no cooling is added, to save energy requirements, since the streams is heated further after mixing. Furthermore, the supply temperature, target temperature, and duty for the MTH model presented in Table 8.1 is the average taken over all the tested catalysts, with included standard deviations. From this, it can be seen that the difference between the simulated duty requirements and the temperatures is minor. Based on these minor deviations, it has been chosen to conduct pinch analysis on one of the catalysts. The pinch analysis is used to understand each system's actual required duty. The analysis will aim to determine the net heat surplus and deficit, and where potential

heat integration can be made.

8.1 Pinch Analysis Across Systems

The pinch analysis is based on the duty and temperature requirements for using the Co-ZSM-5(50) catalyst, which is chosen due to its stability and overall fuel production. The regular composite curves (CCV) and the grand composite curve (GCC) are used to describe the amount of required utility available from other parts of the total system.

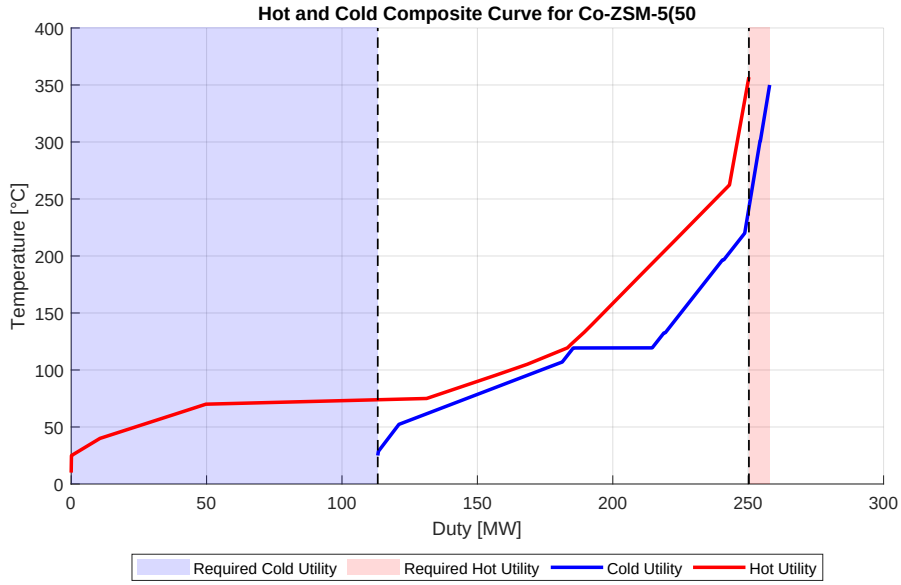

Figure 8.1: CCV for full system integration

On the CCV shown in Figure 8.1, it can be seen that significantly more external cooling is required compared to external heating. It can also be seen that approximately 140 MW of both heating and cooling can be integrated across all the systems, which reduces the required duty significantly compared to not co-locating the MEA CC, the AWE, the methanol synthesis, and the MTH synthesis. By looking at GCC presented in Figure 8.2, it can be seen that the pinch point is located at 121.8 °C. This corresponds to the temperature demand of the reboiler from the CCV process, including the chosen minimum temperature difference of $\Delta T_{\text{min}} = 5°\text{C}$.

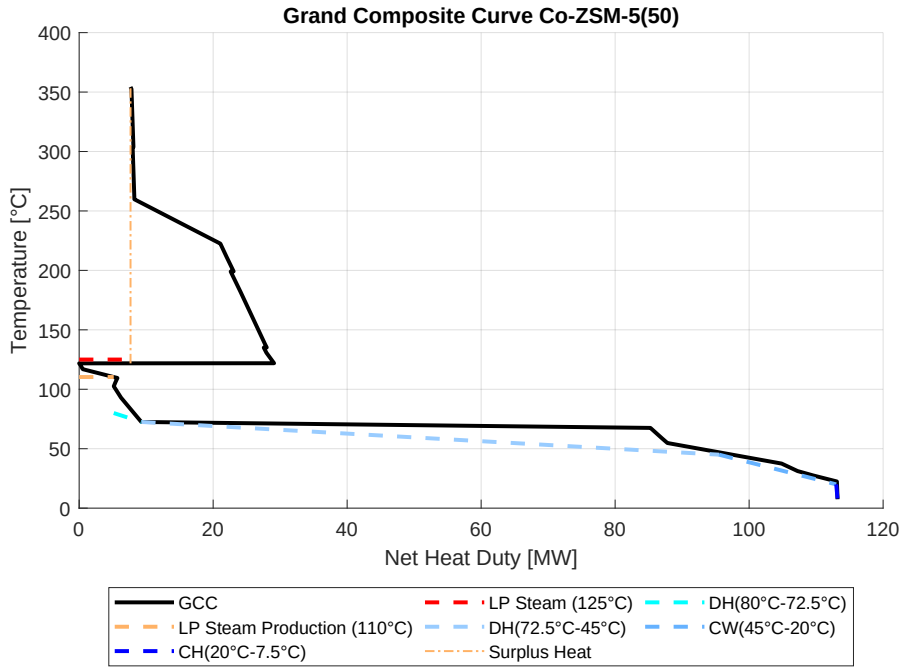

Figure 8.2: GCC for full system integration

Looking at the GCC, it can be seen that above pinch point, almost all the required heat can be covered by utilizing full system integration. The remaining 7.6 MW heat requirement can be covered by low-pressure (LP) steam, medium-pressure (MP) steam, and high-pressure (HP). However, being able to use LP steam at 125 °C instead of HP steam, brings significant economic advantages, since LP steam is significantly cheaper compared to Hp steam.
Below the pinch point, almost no excess cooling duty is available for integration. However, due to the pinch point being at 121.8 °C it is possible to produce some LP steam through the cooling of a hot stream at 110 °C. This produced LP steam could, through the utilization of a compressor, be compressed to increase the temperature, so that it could be utilized for heating above the pinch point. This would eliminate the requirement for external LP steam entirely, further increasing the system efficiency. A possible heat integration with the district heating (DH) system could be made from 80 °C to 45 °C, which is also shown by the GCC in Figure 8.2. A proposal of two separate heat exchangers is made, to cover the temperature change from 80 °C to 45 °C. One covers the steeper cooling requirement from 80 °C to 72.5 °C, and another from 72.5 °C to 45 °C. However, since the cold stream from the DH is only heated to 72.5 °C and not the demanded 80 °C, a temperature boost is needed, which could be covered by a heat pump. The remaining cooling requirement from 45 °to 20 °C, and 20 °C to 7.5 °C, can be covered by cooling water (CW) and a cooling chiller, respectively. Cooling through CW is chosen since it can be beneficial since in scenarios where heat integrations with cold large reservoirs, like the sea or cooling ponds, is relatively in-

expensive. Furthermore, cooling below this point, chilled cooling presents as a viable solution, since some cases present the requirement for cooling below 0 °C

8.2 Catalyst Utility Requirement Comparison

To investigate the possible difference in energy requirements by utilizing different catalysts, a utility comparison has been conducted. The overall heating and cooling requirement by utilizing the different tested catalysts can be seen in Table 8.2

	H-ZSM-5(23)	**H-ZSM-5(50)**	**Ni-ZSM-5(50)**	**Co-ZSM-5(50)**	**In-ZSM-5(50)**
Min Hot Utility [MW_{th}]	7.84	7.59	7.30	7.66	7.76
Min Cold Utility [MW_{th}]	113.19	112.98	112.81	113.2	112.9
T_{Pinch} [°C]	121.8	121.8	121.8	121.8	121.8

Table 8.2: Minimum hot and cold utility requirement, and pinch temperature for the different tested catalysts.

From Table 8.2, it can be seen that the changes between the utility requirements from the different catalysts are insignificant. However, since the chemical composition of the product produced from the various catalysts varies, the majority of the changes come from the separation process. It was found that during the separation process of the products, produced over H-ZSM-5(50), the temperature during gas separation ended up at -2.5 °C. To reach this temperature, more cooling through chilling is required, which is more expensive than delivering the required cooling through CW.

8.2.1 System Efficiency Before and After Integration

An analysis of the system efficiency is made to see the impact of the system integration. To describe the efficiency of the fuel production and the total system, two different terms are used. These are referred to as the energetic jet-fuel efficiency (EJFE), and the total system efficiency η_{Tot} is used. These are presented in Equations (8.1) and (8.2)

$$EJFE = \frac{\dot{m}_{\text{Fuel}} \cdot LHV_{\text{Fuel}}}{\dot{m}_{\text{H}_2} \cdot LHV_{\text{H}_2,\text{in}} + Q_{\text{Ext}}} \tag{8.1}$$

Here $\dot{m}_{\text{Fuel}}$ is the mass flow of the total fuel produced, including gasoline, kerosene, and diesel. $\dot{m}_{\text{H}_2,\text{in}}$ is the mass flow of hydrogen produced from the AWE unit, LHV_{Fuel} and LHV_{H_2} are the LHV of the produced fuel and H_2, respectively.

$$\eta_{\text{Tot}} = \frac{\dot{m}_{\text{Fuel}} \cdot LHV_{\text{Fuel}}}{\dot{m}_{\text{H}_2} \cdot LHV_{\text{H}_2,\text{in}} + Q_{\text{Ext}} + P_{\text{Ext}}} \tag{8.2}$$

Unlike the EJFE, the η_{Tot} considers the required electrical power P_{Ext}, which is also needed in the system. The LHV of the produced fuels, along with the calculated efficiencies, can be seen in Table 8.3

	H-ZSM-5(23)	**H-ZSM-5(50)**	**Ni-ZSM-5(50)**	**Co-ZSM-5(50)**	**In-ZSM-5(50)**
$\text{LHV}_{\text{Kerosene}}$ [MJ/kg]	41.44	41.47	41.58	41.88	41.87
LHV_{Fuel}[MJ/kg]	41.51	42.32	41.86	43.62	41.68
$\text{EJFE}_{\text{Kerosene}}$[%]	5.50	4.63	6.78	3.45	5.94
$\text{EJFE}_{\text{Fuel}}$[%]	15.63	14.69	17.10	15.42	15.63
η_{Tot}[%]	7.36	6.91	8.04	7.26	7.36
$\eta_{Tot,Heat}$[%]	9.35	8.78	10.20	9.22	9.34
$\eta_{Tot,NI}$[%]	4.96	4.66	5.40	4.90	4.96

Table 8.3: System efficiencies including and excluding cooling requirement, Fuel efficiency, and no interation

Table 8.3 presents two new efficiencies $\eta_{Tot,Heat}$ and $\eta_{Tot,NI}$, which are the total system efficiency where only heating demand is covered, and the total system efficiency, with no heat integration. It has been chosen to investigate this, since it was found that DH could cover the majority of the cooling demand. Depending on the system's location, this cooling duty could be considered low cost, compared to other cooling duty costs, such as cooling through refrigerant chilling.

Analysis showed that without system integration, the total system efficiency ranged from 4.66% to 5.4%. However, by utilizing the excess heat available within the co-located system, efficiency increased to 8.04%. This could be further improvedup to 10.2% depending on the catalyst, when considering only the required hot utility, as cooling within the 72.5 °C to 45 °C range can be considered very low-cost. Catalyst selectivity was also found to have a significant impact on the EJFE. As shown in Table 8.3, $\text{EJFE}_{\text{Fuel}}$ ranged from 14.69% to 17.1%, while $\text{EJFE}_{\text{Kerosene}}$ followed a similar trend, varying from 4.63% to 6.78% depending on the catalyst. Among the tested catalysts, Ni-ZSM-5(50) demonstrated the highest production of jet fuel-range compounds and the highest total system efficiency. However, experimental testing also revealed that this catalyst had a significantly shorter lifetime compared to the others.

As discussed in Chapter 1, commercial jet fuels must meet specific quality requirements. One of these requirements is the LHV, which must exceed 42 MJ/kg for Jet-A fuel. In the simulations, all produced fuels exhibited an LHV below this threshold. This discrepancy can likely be linked to the representative compounds used for the different boiling ranges. These compounds are primarily simple in structure and lack molecular complexity, which may result in a lower LHV compared to the actual fuel.

Heat integration analysis revealed that co-locating the different processes can offer

substantial cost and energy savings. Simulations showed that external energy demands could be met using LP steam, while most of the cooling demand could be supplied by DH at potentially minimal cost. Additionally, the simulations indicated that catalyst selectivity significantly influences overall system efficiency by affecting product quality.

Chapter 9

Conclusion

This thesis experimentally investigated the catalytic performance of different ZSM-5-based catalysts in turning wet methanol into sustainable aviation fuel (SAF) in a single-stage continuous methanol-to-jet (MTJ) process. Besides experimentally testing, a complete system model was developed to model the overall energy requirements of producing SAF from methanol. This model involved an equilibrium-based monoethanolamine (MEA) carbon capture (CC) CO_2 process, an alkaline water electrolysis (AWE) for hydrogen (H_2) production, a kinetic methanol synthesis, and an experimental methanol-to-hydrocarbon (MTH) model to estimate the catalytic selectivity towards compounds in the jet fuel range. The model was based on a full-scale point source CC project in Denmark, which aimed to capture 280.000 tonnes of CO_2 per year, providing a realistic foundation for evaluating the integration of capture and conversion technologies.

A pinch analysis was used to investigate the possible advantages of co-locating an MEA CC plant, an AWE plant, a methanol synthesis plant, and an MTH synthesis based on experimental assessment. This analysis aimed to determine the possibility of internal heat recovery through co-location. The pinch analysis revealed that without system integration, the overall system efficiency for total liquid fuel production, including electric power consumption, ranged from 4.66% to 5.40%, depending on the selected catalyst. Through co-location this efficiency was further increased to a range from 6.91% to 8.04%, highlighting the importance of heat integration.
Furthermore, it was revealed that the majority of the cold utility required could be covered by relatively inexpensive district heating (DH), thereby potentially reducing the cost of needed cold utility. By assuming no cost of the cold utility, and heat integrating the system with the DH system, the system efficiency could be increased up to 10.20%, depending on the utilized catalyst. The overall energetic jet fuel efficiency (EJFE) for kerosene, was evaluated from the production of H_2 through AWE, and varied from 3.45% to 6.78%. In contrast, the total $EJFE_{Fuel}$ varied from 14.69% to 17.10%, with Ni-ZSM-5(50) indicating the highest EJFE for both kerosene and total fuels, while, Co-ZSM-5(50) indicated the lowest EJFE for jet fuel and H-ZSM-5(50) exhibited the overall lowest EJFE.

Through experimental MTH modeling, it was found that the $\eta_{C\rightarrow Kerosene}$ varied from 8.85% to 16.69% with Ni-ZSM-5(50) having the highest conversion. This suggested that a significant amount of the captured CO_2 was not utilized for jet fuel but instead ended up in the gasoline range and the gas phase, with minimal losses throughout the system through purge streams. Furthermore, the $\eta_{H\rightarrow Kerosene}$, pointed towards this tendency, as the amount of hydrogen which ended up in the kerosene range varied

from 2.94% to 5.83%, due to high amounts ending up in water production through both methanol systhesis, and the dehydration of methanol to ethene. Furthermore, the lower heating value (LHV) of the kerosene was estimated through simulation, and varied from 41.44 MJ/kg to 41.88 MJ/kg, depending on the catalyst, with Co-ZSM-5(50) yielding the highest LHV.

The MTH experiments revealed a clear relationship between catalyst deactivation and changes in product distribution. As time-on-stream (TOS) increased, reduced activity, caused by coke accumulation, led to a shift from short-chain aromatics to heavier aromatics and more aliphatic components. This was accompanied by an increase in aliphatic HC yield, indicating that deactivation disfavored cracking reactions and shifted the acidity to favor the aliphatic cycle.

Liquid yields varied among catalysts. The unmodified H-ZSM-5 catalysts with SiO_2/Al_2O_3 ratios of 23 and 50 had liquid yields of 43.0 wt.% and 41.1 wt.% with equal active lifetimes of 44 h. The lower acidity of the H-ZSM-5(23) lead to an increased yield of aromatics due to the shift towards the aromatic cycle, of 86.09%, compared to 69.43% of H-ZSM-5(50).
Nickel-modified ZSM-5 achieved the highest average liquid yield of 46.0 wt.% of which the jet fuel-range yield was 44.61 wt.%, but suffered from a short lifetime <20 hours and rapid deactivation due to its high selectivity towards aromatics of 78.01 %.
In contrast, the cobalt-modified catalyst delivered more stable, though slightly lower, liquid yields of 43.9 wt.% over extended operation of 46 h, demonstrating superior lifetime and stability. However, due to a high selectivity towards aliphatics, of 37.96 %, almost exclusively in the gasoline range, the average yield within the jet-fuel range was lower, at just 27.62 wt.%.
Indium offered a balanced compromise between selectivity and stability, with an average liquid yield of 41.4 wt.%, of which 43.1 wt.% was within the distillation range of jet fuel, with an operational lifetime of 28 h. Likewise, an intermediate between aromatic and aliphatic selectivity at 68.96% and 28.44% respectively, was also identified.
The dominance of gasoline-range aliphatics across all catalysts was believed to be attributed to the diffusion limitations of the ZSM-5 framework, which constrains the formation of longer aliphatic jet-range molecules, relying on the cyclic rings for the formation of heavier HCs.

In conclusion, catalyst choice involves a trade-off between jet fuel selectivity, stability, and coke tolerance. Cobalt-modified ZSM-5 shows promise for stable operation and lighter aviation fuels, suggesting its potential for Jet B applications. In contrast, nickel delivers higher jet-range output at the cost of reduced longevity, limiting its practical use. Effective catalyst design will require optimization of both product selectivity and resistance to deactivation.
.

Chapter 10

Future Work

This thesis establishes the foundation for understanding the direct influence of catalyst selectivity and performance on the production of liquid HCs in the LPG, gasoline, kerosene, and diesel range. However, various important parameters and aspects of catalytic performance are yet to be covered. This chapter aims to highlight the potential areas that could further expand this study to get a more comprehensive understanding of the MTJ process and its potential.

10.1 Gas Analysis

Due to limitations in the available laboratory equipment, it was not possible to measure the chemical composition of the gas phase produced by each catalyst directly. As a result, the gas composition was estimated based on literature data from similar catalysts. Direct analysis of the gas phase would allow for a more accurate assessment of catalytic behavior by providing detailed insights into the product distribution. This understanding is essential for identifying precise reaction pathways and improving process modeling.

10.2 Aqueous Phase Analysis

Beyond gas-phase analysis, examining the aqueous phase could offer valuable information about the methanol conversion in the MTH synthesis. This would provide a more comprehensive evaluation of catalytic performance. Quantifying the exact methanol conversion could also help close existing gaps in the estimated mass balances and enhance the overall accuracy of the process assessment.

10.3 Catalyst Regeneration

In this study, the catalysts were tested until full deactivation and then removed from the experimental setup without undergoing regeneration. In practical applications, catalyst regeneration is standard practice to extend catalyst lifetime and improve economic performance. Including regeneration experiments would offer a more realistic understanding of catalyst durability and could reveal changes in catalytic activity after repeated use.

10.4 Gas Recirculation

Gas recirculation is a common practice in industrial processes to improve reactant utilization. During methanol synthesis, recirculation significantly increased the conversion of H_2 and CO_2 into methanol. Applying a similar approach to the MTH process could potentially increase the yield of liquid hydrocarbons, particularly in the kerosene range. Implementing gas-phase recirculation may also provide economic benefits by enhancing overall process efficiency and product yield.

10.5 Influence of Direct-Air-Capture

The MEA-based CC model used in this thesis is based on PSCC, which extracts CO_2 from flue gas. However, this method cannot achieve complete CO_2 removal and demands substantial thermal energy per tonne of CO_2 captured, raising the system's total heat requirement. DAC presents an alternative that uses less thermal energy but requires significantly more electricity. DAC also offers the potential for net-negative CO_2 emissions, as it captures atmospheric CO_2. This could improve overall system efficiency by reducing energy losses associated with converting electricity to heat.

10.6 Economic Assesment

An economic evaluation of the integrated system was not included in this thesis. Conducting such an assessment would provide valuable insight into the costs associated with constructing and operating the proposed system. It could also help estimate the production cost of synthetic fuels and assess their competitiveness with conventional jet fuels. Moreover, an economic study could evaluate the financial advantages of co-location through the implementation of a heat exchanger network.

10.7 Heat Exchanger Network

The heat integration analysis in this thesis focused solely on estimating potential energy savings from co-locating the processes. In real-world industrial applications, a detailed heat exchanger network would be necessary to determine the exact number and placement of heat exchangers. Developing a complete heat exchanger network, alongside an economic analysis, would yield a more thorough understanding of both energy recovery potential and system costs.

Bibliography

[1] CO2levels.org. Atmospheric co2 levels graph. https://www.co2levels.org//„ 2025.

[2] CO2levels.org. Atmospheric co2 levels graph. https://www.statista.com/statistics/264699/worldwide-co2-emissions///„ 2025.

[3] United Nations Climate Change. The paris agreement. https://unfccc.int/process-and-meetings/the-paris-agreement?gclid=CjwKCAiA3KefBhByEiwAi2LDHFXPgxxSAJSzqJPCsUEqhx9w2H0FY_BT_JzVLpa6LONWbJb6LXY1JhoCVWYQAvD_BwE&fbclid=IwY2xjawIW7cNleHRuA2FlbQIxMAABHT8M9wzZyzIKQHGUYaZJJYneZwp7j6YGTmV6KpknuoD_Plq81-AxUPvNrA_aem_z0s-u0mQb85aTygBSjiyuA„ 2025.

[4] Candelaria Bergero, Greer Gosnell, Dolf Gielen, Seungwoo Kang, Morgan Bazilian, and Steven J Davis. Pathways to net-zero emissions from aviation. *Nature Sustainability*, 6(4):404–414, 2023.

[5] Our World in Data. Cars, planes, trains: where do co emissions from transport come from? https://ourworldindata.org/co2-emissions-from-transport, 2024.

[6] Boeing. Commerical market outlook 2022 - 2041. https://www.boeing.com/content/dam/boeing/boeingdotcom/market/assets/downloads/CMO_2022_Report_FINAL_v02.pdf, 2022. Last accessed 14th of Oktober 2024.

[7] Statista. Estimated annual average growth rates for passenger air traffic from 2023 to 2043, by region. https://www.statista.com/statistics/269919/worldwide-growth-rates-for-passenger-traffic/, 2023. Last accessed 14th of Oktober 2024.

[8] International Council on Clean Transportation (ICCT). Vision 2050: A strategy to decarbonize the global transport sector by mid-century. *white paper*, 2020.

[9] International Air Transport Association. A global approach to reducing aviation emissions. https://www.yumpu.com/en/document/view/24408947/a-global-approach-to-reducing-aviation-emissions-from-air-france/, 2014. Last accessed 14th of Oktober 2024.

[10] European Aviation Environmental Association. Sustainable aviation fuels. https://www.easa.europa.eu/en/domains/environment/eaer/sustainable-aviation-fuels, 2024.

[11] Chervon. Aviation fuels technical review. https://www.chevron.com/-/media/chevron/operations/documents/aviation-tech-review.pdf, 2007. Last accessed 28th of Oktober 2024.

[12] CSGNetwork. Aviation jet fuel information. http://www.csgnetwork.com/jetfuel.html, 2024.

[13] Energy Information Administration. Petroleum other liquids. https://www.eia.gov/dnav/pet/pet_pnp_pct_dc_nus_pct_a.htm, 2024.

[14] Shell. Civil jet fuel. https://www.shell.com/business-customers/aviation/aviation-fuel/civil-jet-fuel-grades.html, 2024.

[15] Skybrary. Ignition of fuels. https://skybrary.aero/articles/ignition-fuels, 2024.

[16] Aviationfile. Jet fuel types. https://www.aviationfile.com/jet-fuel-types/, 2023.

[17] ExxonMobil. World jet fuel specifications. chrome-extension://efaidnbmnnnibpcajpcglclefindmkaj/http://large.stanford.edu/courses/2017/ph240/chhoa1/docs/exxon-2008.pdf, 2008.

[18] Rasmus Morel Aske Blankenfeldt. Temperature study of catalytic conversion of ethanol to sustainable aviation fuel over v-zsm-5, 2024.

[19] Shane Kosir, John Feldhausen, David Bell, Dylan Cronin, Randall Boehm, and Joshua Heyne. Quantitation of olefins in sustainable aviation fuel intermediates using principal component analysis coupled with vacuum ultraviolet spectroscopy. *Frontiers in Fuels*, 1:1246950, 2023.

[20] Tara J Fortin, Thomas J Bruno, and Tara M Lovestead. Comparison of heat capacity measurements of alternative and conventional aviation fuels. *International Journal of Thermophysics*, 44(1):5, 2023.

[21] U.S Department of Energy. Sustainable aviation fuel. https://afdc.energy.gov/fuels/sustainable-aviation-fuel, 2022. Last accessed 16th of Oktober 2024.

[22] Md Fahim Shahriar and Aaditya Khanal. The current techno-economic, environmental, policy status and perspectives of sustainable aviation fuel (saf). *Fuel*, 325:124905, 2022.

[23] Brandon Han Hoe Goh, Cheng Tung Chong, Hwai Chyuan Ong, Tine Seljak, Tomaž Katrašnik, Viktor Józsa, Jo-Han Ng, Bo Tian, Srinibas Karmarkar, and Veeramuthu Ashokkumar. Recent advancements in catalytic conversion pathways for synthetic jet fuel produced from bioresources. *Energy Conversion and Management*, 251:114974, 2022.

[24] Miaojia Song, Xinghua Zhang, Yubao Chen, Qi Zhang, Lungang Chen, Jianguo Liu, and Longlong Ma. Hydroprocessing of lipids: An effective production process for sustainable aviation fuel. *Energy*, page 129107, 2023.

[25] Energy Efficiency Renewable Energy. Sustainable aviation fuel. https://afdc.energy.gov/fuels/sustainable-aviation-fuel, 2023.

[26] Sudha Eswaran, Senthil Subramaniam, Scott Geleynse, Kristin Brandt, Michael Wolcott, and Xiao Zhang. Dataset for techno-economic analysis of catalytic hydrothermolysis pathway for jet fuel production. *Data in brief*, 39:107514, 2021.

[27] MANUEL GARCIA-PEREZ Kristin Brandt Abid H. Tanzil, Lina Martinez-Valencia and Michael P. Wolcott. Fischer tropsch techno-economic analysis, v. 2.2. https://rex.libraries.wsu.edu/esploro/outputs/model/99900620482301842, 2021.

[28] MANUEL GARCIA-PEREZ Kristin Brandt Abid H. Tanzil, Lina Martinez-Valencia and Michael P. Wolcott. Hydroprocessed esters and fatty acids techno-economic analysis, v. 2.2. https://rex.libraries.wsu.edu/esploro/outputs/model/99900620482201842, 2021.

[29] MANUEL GARCIA-PEREZ Kristin Brandt Abid H. Tanzil, Lina Martinez-Valencia and Michael P. Wolcott. Alcohol to jet techno-economic analysis, v. 2.2. https://rex.libraries.wsu.edu/esploro/outputs/model/99900620482101842, 2021.

[30] Kelly Cox, Marguerite Renouf, Aidan Dargan, Christopher Turner, and Daniel Klein-Marcuschamer. Environmental life cycle assessment (lca) of aviation biofuel from microalgae, pongamia pinnata, and sugarcane molasses. *Biofuels, Bioproducts and Biorefining*, 8(4):579–593, 2014.

[31] Enzo Favoino and Michele Giavini. Bio-waste generation in the eu: Current capture levels and future potential, 2nd edition - 2024. *Bio-based Industries Consortium (IBC)*, 2024.

[32] IEA Bioenergy Task. Progress in commercialization of biojet/sustainable aviation fuels (saf): Technologies and policies. 2024.

[33] World economic forum McKinsey Company. Clean skies for tomorrow: Delivering on the global power-to-liquid ambition insight report may 2022. https://www.mckinsey.com/~/media/mckinsey/industries/aerospace%20and%20defense/our%20insights/clean%20skies%20for%20tomorrow%20delivering%20on%20the%20global%20power%20to%20liquid%20ambition/clean-skies-for-tomorrow-delivering-on-the-global-power-to-liquid-ambition.pdf, 2022.

[34] International Civil Aviation Organisation. Saf rules of thumb. https://www.icao.int/environmental-protection/Pages/SAF_RULESOFTHUMB.aspx, 2024.

[35] International Air Transport Association. Jet fuel price monitor. https://www.iata.org/en/publications/economics/fuel-monitor/, 2024.

[36] Magno F. Santos, Antonio E. Bresciani, Newton L. Ferreira, Gabriel S. Bassani, and Rita M.B. Alves. Carbon dioxide conversion via reverse water-gas shift reaction: Reactor design. *Journal of Environmental Management*, 345:118822, 2023.

[37] Thushara Kandaramath Hari, Zahira Yaakob, and Narayanan N Binitha. Aviation biofuel from renewable resources: Routes, opportunities and challenges. *Renewable and Sustainable Energy Reviews*, 42:1234–1244, 2015.

[38] Ulf Neuling and Martin Kaltschmitt. Conversion routes from biomass to biokerosene, 2018.

[39] Carlos Ortega, Mojtaba Rezaei, Volker Hessel, and Gunther Kolb. Methanol to dimethyl ether conversion over a zsm-5 catalyst: Intrinsic kinetic study on an external recycle reactor. *Chemical Engineering Journal*, 347:741–753, 2018.

[40] Uffe Vie Mentzel. Towards a methanol economy: Zeolite catalyzed production of synthetic fuels. 2010.

[41] Irina Yarulina, Abhishek Dutta Chowdhury, Florian Meirer, Bert M Weckhuysen, and Jorge Gascon. Recent trends and fundamental insights in the methanol-to-hydrocarbons process. *Nature Catalysis*, 1(6):398–411, 2018.

[42] DM Bibby, NB Milestone, JE Patterson, and LP Aldridge. Coke formation in zeolite zsm-5. *Journal of Catalysis*, 97(2):493–502, 1986.

[43] Zhiwei Wang, Jie Zhang, Yuhang Zhu, Jie Wang, Hongzhi Li, Feng Wang, Wenrong Han, and Zhiping Jiang. Recent progress in the modification of acidic catalysts for methanol-to-jet fuel: A review. *Frontiers in Chemistry*, 8:586, 2020.

[44] Arthur W Chester and Eric G Derouane. *Zeolite characterization and catalysis*, volume 360. Springer, 2009.

[45] Todd J Toops, Andrew J Binder, Pranaw Kunal, Eleni A Kyriakidou, and Jae-Soon Choi. Analysis of ion-exchanged zsm-5, bea, and ssz-13 zeolite trapping materials under realistic exhaust conditions. *Catalysts*, 11(4):449, 2021.

[46] AcsMaterial. Technical data sheet acs material sapo-34. https://www.acsmaterial.com/pub/media/catalog/product/t/d/tds-sapo-34$_2$40228.*pdf*, 2024. *Accessed* : $11 - 05 - 2025$.

[47] AcsMaterial. Technical data sheet acs material ssz-13. https://www.acsmaterial.com/pub/media/catalog/product/2/0/20231222$_t$ds$_s$sz − 13.*pdf*, 2024. *Accessed* : 11 − 05 − 2025.

[48] Zhenglong Li, Andrew Lepore, Brian H. Davison, and Chaitanya K. Narula. Catalytic conversion of biomass-derived ethanol to liquid hydrocarbon blendstock: Effect of light gas recirculation. *Energy & Fuels*, 30(12):10611–10617, 2016.

[49] VS Pavlov, DV Bruter, VL Zholobenko, and II Ivanova. Effects of the physicochemical properties of zeolite catalysts on their deactivation in methanol-to-hydrocarbons conversion (a review). *Petroleum Chemistry*, 64(2):210–234, 2024.

[50] Startup Schoggi. Swiss startup metafuels secures $9m to revolutionize aviation with sustainable fuel breakthroughs, January 2025. Accessed: 2025-05-08.

[51] Ørsted. Carbon capture and storage to reach net-zero globally well have to remove up to 10 billion tonnes of co2 per year by 2050*. https://orsted.com/en/what-we-do/renewable-energy-solutions/bioenergy/carbon-capture-and-storageour-biogenic-co2-sources, 2016. Accessed: 04-05-2025.

[52] Energistyrelsen. Technology data - generation of electricity and district heating. https://ens.dk/en/analyses-and-statistics/technology-data-generation-electricity-and-district-heating, 2016. Accessed: 02-05-2025.

[53] Phyllis2. wood + bark, pine chips (1269). ://phyllis.nl/Biomass/View/1269/, 1998. Accessed: 2025-04-16.

[54] Formation and removal of biomass-derived contaminants in fluidized-bed gasification processes.

[55] Logstor. District energy energy efficiency for urban areas. https://www.logstor.com/-media/5270/dbdh-white-paper.pdf, 2016. Accessed: 02-05-2025.

[56] Danish Energy Agency. Carbon capture, transport and storage - technology descriptions and projections for long-term energy system planning. `https://ens.dk/analyser-og-statistik/teknologikatalog-kulstoffangst-transport-og-lagring`, 2024.

[57] Kamaldeep Sharma. Carbon capture methods. `https://www.moodle.aau.dk/pluginfile.php/3527645/mod_resource/content/3/Carbon%20Capture%20Methods_Lecture%205.pdf`, 2024.

[58] Bushra Khatoon, M Siraj Alam, et al. Study of mass transfer coefficient of co2 capture in different solvents using microchannel: a comparative study. In *Computer Aided Chemical Engineering*, volume 49, pages 691–696. Elsevier, 2022.

[59] Ahmed M Bukar and Muhammad Asif. Technology readiness level assessment of carbon capture and storage technologies. *Renewable and Sustainable Energy Reviews*, 200:114578, 2024.

[60] Peter Markewitz, Wilhelm Kuckshinrichs, Walter Leitner, Jochen Linssen, Petra Zapp, Richard Bongartz, Andrea Schreiber, and Thomas E Müller. Worldwide innovations in the development of carbon capture technologies and the utilization of co 2. *Energy & environmental science*, 5(6):7281–7305, 2012.

[61] Lars ErikØi. Comparison of aspen hysys and aspen plus simulation of co2 absorption into mea from atmospheric gas. *Energy Procedia*, 23:360–369, 2012.

[62] Paty Arango Munoz. Stripper modification of a standard mea process for heat integration with a pulp mill, 2020.

[63] Udara Sampath PR Arachchige and Morten Christian Melaaen. Aspen plus simulation of co2 removal from coal and gas fired power plants. *Energy Procedia*, 23:391–399, 2012.

[64] Claudio Madeddu, Massimiliano Errico, and Roberto Baratti. *CO2 capture by reactive absorption-stripping: modeling, analysis and design*. Springer, 2018.

[65] Inna Kim, Karl Anders Hoff, and Thor Mejdell. Heat of absorption of co2 with aqueous solutions of mea: new experimental data. *Energy Procedia*, 63:1446–1455, 2014.

[66] Sai Hema Bhavya Vinjarapu, Randi Neerup, Anders Hellerup Larsen, Sebastian Nis Bay Villadsen, Nicolas von Solms, Søren Jensen, Jakob Lindkvist Karlsson, Jannik Kappel, Henrik Lassen, Peter Blinksbjerg, et al. Pilot-scale co2 capture demonstration of heat integration through split flow configuration using 30 wt% mea at a waste-to-energy facility. *Separation and Purification Technology*, 345:127311, 2024.

[67] JJ Vazquez-Esparragoza, JC Polasek, VN Hernandez-Valencia, MW Hlavinka, and JERRY BULLIN. A simple application of murphree tray efficiency to separation processes. *Chemical Engineering Communications*, 160(1):91–101, 1997.

[68] Koteswara Rao Putta, Diego D.D. Pinto, Hallvard F. Svendsen, and Hanna K. Knuutila. Co2 absorption into loaded aqueous mea solutions: Kinetics assessment using penetration theory. *International Journal of Greenhouse Gas Control*, 53:338–353, 2016.

[69] Aleksander Krótki, Lucyna Więcław-Solny, Adam Tatarczuk, Marcin Stec, Andrzej Wilk, Dariusz Śpiewak, and Tomasz Spietz. Laboratory studies of post-combustion co 2 capture by absorption with mea and amp solvents. *Arabian Journal for Science and Engineering*, 41:371–379, 2016.

[70] Colin Alie. Co 2 capture with mea: integrating the absorption process and steam cycle of an existing coal-fired power plant. Master's thesis, University of Waterloo, 2004.

[71] Mai Bui, Claire S Adjiman, André Bardow, Edward J Anthony, Andy Boston, Solomon Brown, Paul S Fennell, Sabine Fuss, Amparo Galindo, Leigh A Hackett, et al. Carbon capture and storage (ccs): the way forward. *Energy & Environmental Science*, 11(5):1062–1176, 2018.

[72] Qi Feng, Gaoyang Liu, Bing Wei, Zhen Zhang, Hui Li, Haijiang Wang, et al. A review of proton exchange membrane water electrolysis on degradation mechanisms and mitigation strategies. *Journal of Power Sources*, 366:33–55, 2017.

[73] International Solar Alliance Green Hydrogen Innovation Centre. Technology. `https://isa-ghic.org/technology`, 2024.

[74] Oliver Schmidt, Ajay Gambhir, Iain Staffell, Adam Hawkes, Jenny Nelson, and Sheridan Few. Future cost and performance of water electrolysis: An expert elicitation study. *International journal of hydrogen energy*, 42(52):30470–30492, 2017.

[75] Iva Ridjan Skov and Hamza Abid. Renewable aviation e-saf catalogue and system impacts. 2024.

[76] Mónica Sánchez, Ernesto Amores, David Abad, Lourdes Rodríguez, and Carmen Clemente-Jul. Aspen plus model of an alkaline electrolysis system for hydrogen production. *International journal of hydrogen energy*, 45(7):3916–3929, 2020.

[77] Thyssenkrupp Nucera. Industrial-scale water electrolysis for green hydrogen production. https://www.thyssenkrupp-nucera.com/wp-content/uploads/2023/11/thyssenkrupp-nucera$_{g}reen - hydrogen_{b}rochure_{w}eb.pdf$?, 2023. *Accessed* : $11 - 05 - 2025$.

[78] Danfoss. Europes largest electrolysis plant under construction is powered by danfoss drives. https://www.danfoss.com/en/about-danfoss/news/dds/europe-s-largest-electrolysis-plant-under-construction-is-powered-by-danfoss-drives, 2022. Accessed: 11-05-2025.

[79] ENERTRAG. Electrolysis corridor in eastern germany ipcei joint project creates a strong hub for green hydrogen. https://enertrag.com/projects-show-cases/hydrogen-projects/electrolysis-corridor-in-eastern-germany, 2022. Accessed: 11-05-2025.

[80] Niels D Nielsen, Anker D Jensen, and Jakob M Christensen. The roles of co and co2 in high pressure methanol synthesis over cu-based catalysts. *Journal of Catalysis*, 393:324–334, 2021.

[81] Xiaoti Cui. Fuel cells, hydrogen technology and power-to-x - converting co2 to methanol: an introduction. `https://www.moodle.aau.dk/pluginfile.php/3543994/mod_resource/content/1/Lecture%209%20part%202%20e-methanol%20production.pdf`, 2024.

[82] Xiaoti Cui, Søren Knudsen Kær, and Mads Pagh Nielsen. Energy analysis and surrogate modeling for the green methanol production under dynamic operating conditions. *Fuel*, 307:121924, 2022.

[83] David Peterson, James Vickers, and Dan DeSantis. Hydrogen production cost from pem electrolysis 2019. Technical Report DOE/EE-19009, U.S. Department of Energy, Hydrogen and Fuel Cells Program, 2020. Accessed: 2025-04-16.

[84] Statista. Carbon capture cost worldwide by technology 2022. `https://www.statista.com/statistics/1304575/global-carbon-capture-cost-by-technology/`, 2024. Accessed: 2025-04-16.

[85] Morten Bjørgen, Stian Svelle, Finn Joensen, Jesper Nerlov, Stein Kolboe, Francesca Bonino, Luisa Palumbo, Silvia Bordiga, and Unni Olsbye. Conversion of methanol to hydrocarbons over zeolite h-zsm-5: On the origin of the olefinic species. *Journal of Catalysis*, 249(2):195–207, 2007.

[86] Su-Un Lee, Tae-Wan Kim, Kwang-Eun Jeong, Sungjune Lee, Min Cheol Shin, and Chul-Ung Kim. Compositional dependence of co-and mo-supported beta zeolite for selective one-step hydrotreatment of methyl palmitate to produce bio jet fuel range hydrocarbons. *RSC advances*, 13(3):2168–2180, 2023.

[87] Yanliang Zhai, Wanli Zhang, Xianggang Lu, Jun Wang, Jian Zhang, Lili Ma, Zhixiang Zhang, and Zhijun Li. Preparation of hierarchical co/beta catalyst and its application in hydrogenation of co to aviation kerosene. *Crystals*, 13(7):1053, 2023.

[88] Jirí Cejka, Avelino Corma, and Stacey Zones. *Zeolites and catalysis: synthesis, reactions and applications*. John Wiley & Sons, 2010.

[89] Hélène Olivier-Bourbigou, PAR Breuil, Lionel Magna, Tiphaine Michel, M Fernandez Espada Pastor, and Damien Delcroix. Nickel catalyzed olefin oligomerization and dimerization. *Chemical Reviews*, 120(15):7919–7983, 2020.

[90] Arno De Klerk. *Fischer-tropsch refining*. John Wiley & Sons, 2012.

[91] Michael Stöcker. Methanol-to-hydrocarbons: catalytic materials and their behavior. *Microporous and mesoporous materials*, 29(1-2):3–48, 1999.

[92] Ming Yin, Jifeng Pang, Jin Guo, Xianquan Li, Yujia Zhao, Pengfei Wu, and Mingyuan Zheng. Tailoring ni based catalysts by indium for the dehydrogenative coupling of ethanol into ethyl acetate. *Green Energy Environment*, 9(8):1321–1331, 2024.

[93] Zen Maeno, Shunsaku Yasumura, Xiaopeng Wu, Mengwen Huang, Chong Liu, Takashi Toyao, and Ken-ichi Shimizu. Isolated indium hydrides in cha zeolites: speciation and catalysis for nonoxidative dehydrogenation of ethane. *Journal of the American Chemical Society*, 142(10):4820–4832, 2020.

[94] Jiaxu Liu, Ning He, Wei Zhou, Long Lin, Guodong Liu, Chunyan Liu, Jilei Wang, Qin Xin, Guang Xiong, and Hongchen Guo. Isobutane aromatization over a complete lewis acid zn/hzsm-5 zeolite catalyst: performance and mechanism. *Catalysis Science & Technology*, 8(16):4018–4029, 2018.

[95] Helmut Knözingerm and Karl Kochloefl. *Heterogeneous Catalysis and Solid Catalysts Organometallic Compounds and Homogeneous Catalysis is a separate Keyword*. Wiley-VCH Verlag GmbH Co. KGaA, 2005.

[96] Zhaohui Liu and Jianfeng Huang. Fundamentals of the catalytic conversion of methanol to hydrocarbons. *Chemical Synthesis*, 2(4):N–A, 2022.

[97] Misael García Ruiz, Dora A Solís Casados, Julia Aguilar Pliego, Carlos Márquez Álvarez, Enrique Sastre de Andrés, Diana Sanjurjo Tartalo, Raquel Sainz Vaque, and Marisol Grande Casas. Zsm-5 zeolites modified with zn and their effect on the crystal size in the conversion of methanol to light aromatics (mta). *Reaction Kinetics, Mechanisms and Catalysis*, 129:471–490, 2020.

[98] Ebrahim Mohiuddin, Masikana M Mdleleni, and David Key. Catalytic cracking of naphtha: The effect of fe and cr impregnated zsm-5 on olefin selectivity. *Applied Petrochemical Research*, 8:119–129, 2018.

[99] Isa Carolina Silva Costa, Elisabete Moreira Assaf, and José Mansur Assaf. Improving coking resistance and catalytic performance of ni catalyst from lanio3 perovskite by dispersion on sba-15 mesoporous silica for hydrogen production by steam reforming of ethanol. *Topics in Catalysis*, 67(19):1318–1333, 2024.

[100] Ana G Gayubo, Ana M Tarrío, Andres T Aguayo, Martin Olazar, and Javier Bilbao. Kinetic modelling of the transformation of aqueous ethanol into hydrocarbons on a hzsm-5 zeolite. *Industrial & engineering chemistry research*, 40(16):3467–3474, 2001.

[101] Shimadzu. Overview of gcms. `https://www.shimadzu.eu/service-support/technical-support/gas-chromatograph-mass-spectrometry/overview/overview_of_gcms.html`, ND.

[102] Clarence D. Chang and Anthony J. Silvestri. The conversion of methanol and other o-compounds to hydrocarbons over zeolite catalysts. *Journal of Catalysis*, 47(2):249–259, 1977.

[103] Yu-Jue Du, Wen-De Hu, Chuan-Ming Wang, Jian Zhou, Guang Yang, Yang-Dong Wang, and Wei-Min Yang. First-principles microkinetic analysis of lewis acid sites in zn-zsm-5 for alkane dehydrogenation and its implication to methanol-to-aromatics conversion. *Catalysis Science & Technology*, 11(6):2031–2046, 2021.

[104] Subhas Madavu Salian, Mahuya Bagui, and Raksh Vir Jasra. Industrially relevant ethylene trimerization catalysts and processes. *Applied Petrochemical Research*, pages 1–13, 2021.

[105] OV Bragin, AV Preobrazhenskii, and AL Liberman. Catalytic cyclotrimerization of ethylene to benzene. *Bulletin of the Academy of Sciences of the USSR, Division of chemical science*, 23:2654–2659, 1974.

[106] Yanjun Zhang, Yao Liu, and Jianwei Li. In situ synthesis of metal-containing zsm-5 and its catalytic performance in aromatization of methanol. *ACS omega*, 7(28):24241–24248, 2022.

[107] Lu Song, Juan Carlos Navarro de Miguel, Sarah Komaty, Sang-Ho Chung, and Javier Ruiz-Martinez. Role of phosphorus on zsm-5 zeolite for the methanol-to-hydrocarbon reaction. *ACS Catalysis*, 15(7):5623–5639, 2025.

[108] ChemEurope. Standard enthalpy change of formation (data table). `https://www.chemeurope.com/en/encyclopedia/Standard_enthalpy_change_of_formation_%28data_table%29.html`. Accessed: 2025-05-21.

[109] ChemEurope. Toluene (data page). `https://www.chemeurope.com/en/encyclopedia/Toluene_%28data_page%29.html`.

[110] Simulated distillation of petroleum fractions using astm d2887. Technical report, Agilent Technologies, n.d. Accessed: 2025-05-21.

[111] Simulated distillation of petroleum products by gc according to astm d2887. Technical report, Thermo Fisher Scientific, n.d. Application Note D22163.

[112] Marta Díaz, Eva Epelde, José Valecillos, Sepideh Izaddoust, Andrés T. Aguayo, and Javier Bilbao. Coke deactivation and regeneration of hzsm-5 zeolite catalysts in the oligomerization of 1-butene. *Applied Catalysis B: Environmental*, 291:120076, 2021.

[113] Baodong Wang and George Manos. A novel thermogravimetric method for coke precursor characterisation. *Journal of Catalysis*, 250(1):121–127, 2007.

[114] Xu Hou, Liu Zhao, and Zhenheng Diao. Roles of alkenes and coke formation in the deactivation of zsm-5 zeolites during n-pentane catalytic cracking. *Catalysis Letters*, 150:2716–2725, 2020.

[115] Ifeanyi Michael Smarte Anekwe and Yusuf Makarfi Isa. Influence of metal doping on the coke formation of a novel hierarchical hzsm-5 zeolite catalyst in the conversion of 1-propanol to fuel blendstock. *RSC advances*, 15(6):3988–3999, 2025.

[116] Gamzenur Özsin. Assessing thermal behaviours of cellulose and poly (methyl methacrylate) during co-pyrolysis based on an unified thermoanalytical study. *Bioresource technology*, 300:122700, 2020.

[117] 1,2,4,5-tetramethylbenzene, 97%. https://www.avantorsciences.com/si/en/product/769455/1-2-4-5-tetramethylbenzene-97, 2025. Thermo Fisher Scientific, CAS No. 95-93-2, Molecular Formula: $C_{10}H_{14}$, Molecular Weight: 134.22 g/mol.

[118] Yan Gao, Binghui Zheng, Guang Wu, Fangwei Ma, and Chuntao Liu. Effect of the si/al ratio on the performance of hierarchical zsm-5 zeolites for methanol aromatization. *RSC Advances*, 6:83581–83588, 2016.

[119] Morten Bjørgen, Stian Svelle, Finn Joensen, Jesper Nerlov, Stein Kolboe, Francesca Bonino, Luisa Palumbo, Silvia Bordiga, and Unni Olsbye. Conversion of methanol to hydrocarbons over zeolite h-zsm-5: On the origin of the olefinic species. *Journal of Catalysis*, 249(2):195–207, 2007.

[120] Paulsen M.M, Petersen S.B, Pedersen T.H, and Lozano E.M. High-temperature direct air capture for utilisation in fischer-tropsch synthesis. *Applied Energy*, 369, 2024.

[121] Occupational Safety and Health Administration (OSHA). 1910.110 - Storage and Handling of Liquefied Petroleum Gases, 2023. Accessed: 2025-05-26.

[122] Hesamedin Hekmatmehr, Ali Esmaeili, Maryam Pourmahdi, Saeid Atashrouz, Ali Abedi, Meftah Ali Abuswer, Dragutin Nedeljkovic, Mohammad Latifi, Sherif Farag, and Ahmad Mohaddespour. Carbon capture technologies: A review on technology readiness level. *Fuel*, 363:130898, 2024.

[123] Klein Sanford and Nellis Gregory. *Thermodynamics*. Cambridge University Press, 2017. ISBN: 978-0-521-19570-6.

Appendix A

Selection of Technologies
A.1 Carbon Capture

Four primary sources of CO_2 for CC exist, depending on the process by which the CO_2 is captured and will be referred to as the CC option. Several CC technologies exist for the capture of CO_2 based on either physical or chemical separation processes.

A.1.1 Carbon Capture Options

Direct air capture

Direct air capture (DAC) captures CO_2 directly from the atmosphere at very low concentrations of approximately 426 ppm or 0.0426 vol.%, making the capture process energy intensive. However, DAC is the only technology removing already emitted CO_2 from the carbon cycle, making the technology carbon negative. DAC also does not require external infrastructure and can be built at locations with cheap and excess energy.

Post-combustion

Post-combustion CC captures CO_2 after combustion, typically used as *point source capture* (PSC) on the flue gases of power plants or other industries with large combustions. Depending on the fuel used, the CO_2 concentrations typically vary from 4 vol.% to 14 vol.% and vary in impurities depending on the used fuel. Post-combustion CC can easily be retrofitted to flue gases of existing infrastructure [56].

Oxy-fuel combustion

Oxy-fuel combustion can be used to greatly increase the concentration of CO_2 of flue gasses by using pure oxygen instead of air. This makes the carbon capture easier and less energy intensive by reaching CO_2 concentration >95 vol%. However, this is not widely used for carbon capture as operation costs are increased and traditionally limited to processes requiring the higher temperatures of oxy-fuel combustion, such as welding and metal cutting, with some new applications emerging within the cement production industry [60]. Retrofitting of oxy-fuel combustion is easy, but separation of air is expensive, as cryogenic conditions is required. Considerations regarding material selection for withstanding higher flame temperatures of oxy-fuel combustion must also be taken into account.

Pre-combustion

Pre-combustion CC captures CO_2 from the process or product streams of chemical processes, such as hydrogen production through steam reforming of natural gas, anerobic digestion to produce biogas, or gasification processes for syngas production. Depending on the chemical processes, the CO_2 concentration will differ but typically varies between 15-40% [122]. As pre-combustion CC is not placed on the flue gas but integrated within the process, implementation requires planning during the construction phase of the plant.
Table A.1 summarizes the advantages and disadvantages of different CC options.

	DAC	**Post-combustion**	**Pre-combustion**	**Oxy-fuel**
CO_2 Concentration	0.04 vol.%	4-14 vol.%	15-40 vol.%	75-98 vol.%
Major impurities	N_2, O_2	N_2, O_2, H_2O	CH_4, CO, H_2	H_2O
Other impurities	-	NO_x, SO_x	NO_x, SO_x, H_2S	NO_x, SO_x
TRL	6-7 (Some commercial, still evolving)	9 (Mature and widely deployed)	6-9 (Depended on the application)	6-8 (Demonstration plants)
Advantages	Carbon negative, deployable anywhere, easy upscaling.	Mature technology, easily retrofitted to existing plants.	High CO_2 concentrations and more energy efficient, possible retrofitting to existing plants.	Very high CO_2 concentrations and efficiencies, low capital costs, easy retrofitting.
Disadvantages	Very low CO_2 concentration and low separation efficiency, high energy requirements leading to high CO_2 cost.	Limited applications, low CO_2 concentrations and low separation efficiency, energy intensive.	Not commercial for all processes, complex integration, and high capital costs.	Expensive/energy intensive separation step for air under cryogenic conditions, complex scale-up.

Table A.1: Overview of different CC options [122], [56], [60]

.

A.1.2 Carbon Capture Technologies

Depending on the selected CC option, the concentration of CO_2 varies greatly. Consequently, the CC technology must exhibit a certain level of selectivity to effectively separate CO_2 from the ambient air, flue gas, or process stream, considering their operating conditions and impurities. In general, four main separation technologies are used.

Physical and Chemical Absorption

In physical and chemical absorption, CO_2 is absorbed within a solvent and desorbed by a change in thermodynamic conditions. Physical absorption relies on the solubility of CO_2 in a given solvent, while chemical absorption relies on the equilibrium and kinetics between the CO_2 and the solvent.

Physical Adsorption

In adsorption, CO_2 is taken up on the surface of another material, the adsorbent, on which the amount of adsorbed CO_2 relies on the adsorption isotherm. The adsorption isotherms describe the equilibrium of adsorbed CO_2 at a given temperature and pressure, in which desorption relies on their change.

Membrane

In membranes, the permeability of different molecules is utilized to physically separate the CO_2 from a flue gas by permeating either the CO_2 molecules or the other molecules through a membrane.

Cryogenic Carbon Capture

In cryogenic carbon capture, the CO_2 is separated through distillation by cooling the flue gas below the dew or frost point of CO_2 to where it sublimates or condenses, of which the CO_2 can be stored in solid or liquid form.

The most widely used separation technology consists of amine-based chemical absorption, of which *mono-ethanol-amine* (MEA) is the most commonly used solvent with a TRL of 9 [59]. MEA consists of a primary amine and primary alcohol with the chemical formula $HOCH_2CH_2NH_2$, and its absorption will be the focus for the CC used within this project.

Appendix B

Estimation of flue gas

To estimate the flue gas produced from the combustion of pinewood chips with bark, the composition of the wood chips must be converted from mass fraction to moles.

$$n_i = \frac{mf_i \cdot m_{fuel}}{MW_i} \tag{B.1}$$

where the mass of m_{fuel} is determined by $n_C = 1$.
From this, the flue gas composition is calculated by element balance. All carbon is converted to CO_2, and all hydrogen in the fuel is converted to water, and all the sulfur is converted to SO_2. For the oxygen, some is contained in the wood chips and the rest is supplied from air. At stoichiometric conditions, no excess oxygen will be present in the flue gas, as it is used for the formation of CO_2, SO_2, and H_2O; however, since 50% excess air is used, the oxygen in the flue gas will 50% of what is used for said formations. The nitrogen is inert and will be 3.76 times the amount of oxygen supplied from the air, equal to a nitrogen/oxygen air ratio of 0.79/0.21.

$$\begin{aligned} n_{CO2} &= n_C \\ n_{H2O} &= n_H/2 \\ n_{SO2} &= n_S \\ n_{O2_{air}} &= (n_C + \frac{n_H}{4} + n_S - \frac{n_O}{2}) \cdot \lambda \\ n_{O2_{flue}} &= (n_C + \frac{n_H}{4} + n_S - \frac{n_O}{2}) \cdot \lambda - 1 \\ n_{N2} &= (3.76 \cdot n_O 2_a ir + n_N/2) \end{aligned}$$

The moles in the flue gas are then converted to mol fractions and mass fractions:

$$\begin{aligned} y_i &= \frac{n_i}{\sum_{i=1}^{j} n_i} \\ mf_i &= \frac{y_i MW_i}{\sum_{i=1}^{j} MW_i y_i} \end{aligned}$$

Unit	CO_2	H_2O	SO_2	N_2	O_2
mol.%	12.33	8.871	0.002743	72.39	6.415
wt.%	18.48	5.444	0.005985	69.08	6.993

Table B.1: Chemical composition of flue gas from combustion of pine wood chips with bark [54].

Appendix C

Alkaline Water Electrolysis Model

Throughout the AWE model, various parameters have been calculated using a MATLAB model. Table C.1 shows additional conditions for the AWE Model.

Coefficient	Value	[Unit]
Polarization curve		
r_1	4.45153×10^{-5}	[Ω m^2]
r_2	6.88847×10^{-9}	[Ω m^2 $^\circ$C^{-1}]
d_1	-3.12996×10^{-6}	[Ω m^2]
d_2	4.47137×10^{-7}	[Ω m^2 bar^{-1}]
s	0.33824	[V]
t_1	-0.01539	[m^2 A^{-1}]
t_2	2.00181	[m^2 $^\circ$C^2 A^{-1}]
t_3	15.24178	[m^2 $^\circ$C^2 A^{-1}]
Faraday efficiency		
f_{11}	478645.74	[A^2 m^{-4}]
f_{12}	-2953.15	[A^2 m^{-4} $^\circ$C^{-1}]
f_{21}	1.03960	[-]
f_{22}	-0.00104	[$^\circ$C^{-1}]

Table C.1: Coefficients used for the electrochemical model of an alkaline water electrolysis[76].

Appendix D

Methanol Synthesis Kinetic Parameters

The kinetic model is based on the primary methanol production route presented by Reaction R 1.1 and Reaction R 4.9, which is the WGS reaction. The reaction rate based on the driving force and the adsorption rate can be seen in Table D.1

Reaction Kinetics	Reaction
$r_{MeOH} = k_d \frac{P_{CO_2} P_{H_2} - K_1^{-1} P_{H_2O} P_{MeOH} / P_{H_2}^2}{(1 + k_c P_{H_2O} / P_{H_2} + k_a P_{H_2}^{0.5} + k_b P_{H_2O})^3}$	R 1.1
$r_{RWGS} = k_e \frac{P_{CO_2} - K_2 P_{H_2O} P_{CO} / P_{H_2}}{1 + k_c P_{H_2O} / P_{H_2} + k_a P_{H_2}^{0.5} + k_b P_{H_2O}}$	R 4.9
$K_1 = 10^{-10.592 + \frac{3066}{T}} \approx \exp\left(-24.389 + \frac{7059.726}{T}\right)$	
$K_2 = 10^{2.029 + \frac{-2073}{T}} \approx \exp\left(-4.672 + \frac{4773.26}{T}\right)$	

Table D.1: Reaction kinetics used in the Aspen Plus methanol synthesis model[82]

I Table D.1 k_d and k_e is the reaction kinetics for Reactions R 1.1 and R 4.9 respectively. k_a, k_b, and k_c is the adsorption coefficients for the kinetic reactions. These adsorption coefficients are calculated from the Arrhenius equation as presented in Equation (D.1), where the activation energy as a constant B

$$k = Ae^{\frac{B}{RT}} \tag{D.1}$$

For the methanol synthesis model, the kinetic parameters, are described in Table D.2

Kinetic Parameters	A	B
k_a [$bar^{-0.5}$]	0.499	17197
k_b [bar^{-1}]	6.62x10^{-11}	124119
k_c [-]	3453.38	-
$k_d[\frac{mol}{kg \cdot s \cdot bar^2}]$	1.07	36696
$k_d[\frac{mol}{kg \cdot s \cdot bar}]$	1.22x10^{11}	-94765

Table D.2: Kinetic parameters used the adsorption constants and the kinetic constants in the Aspen Plus methanol synthesis model[82]

By taking the natural logarithm of the kinetic parameters presented in Table D.2, the desired parameters for aspen plus can be found. These parameters are presented in Table D.3

$k_i = k\exp(-E_a/RT)$	k	E_a
k_d	1.07x10 $^{-3}$ $\left[\frac{\text{mol}}{\text{kg·s·bar}^2}\right]$	-36696 $\left[\frac{\text{kJ}}{\text{kmol}}\right]$
k_e	1.22x10 ^{7} $\left[\frac{\text{mol}}{\text{kg·s·bar}}\right]$	94765 $\left[\frac{\text{kJ}}{\text{kmol}}\right]$

$\ln k_i = A_i + B_i/T$	A_i	B_i
$\ln K_1^{-1}$	24.389	-7059.726
$\ln K_2$	-4.762	4773.16
$\ln k_a$	-0.695149	2068.44
$\ln k_b$	-23.438	14928.92
$\ln k_c$	8.14711	-

Table D.3: Input values for the Aspen Plus methanol synthesis model[82]

D.1 Methanol Synthesis Stream Results

	HYDROGEN	**CO_2**	**S3**	**RFEED**	**PROD**	**RECIRC**	**S9**	**WMEOH**
T [°C]	25.00	10.00	121.71	219.93	275.85	220.00	25.64	25.64
P [bar]	6.70	1.01	60.00	60.00	59.66	60.00	1.01	1.01
CO [Mol%]	0.00	0.00	0.00	1.98	2.23	2.30	0.02	0.00
CO_2 [Mol%]	0.00	100.00	25.00	6.59	4.02	4.24	0.61	0.11
H_2 [Mol%]	100.00	0.00	75.00	91.20	87.71	93.27	0.69	0.01
H_2O [Mol%]	0.00	0.00	0.00	0.04	3.01	3.17	0.35	0.14
CH_3OH [Mol%]	0.00	0.00	0.00	0.19	3.16	0.21	49.31	49.86
Mole Flow [kmol/hr]	2181.37	727.12	2908.50	25642.08	24209.17	22733.58	1452.91	1432.97
Mass Flow [tonne/hr]	43.97	32.00	36.40	137.50	137.50	101.10	36.30	35.88

Table D.4: Stream results from the methanol synthesis model presented in Figure 4.6

D.1.1 Compressor Work Sensitivity Analysis

To minimize the amount of compressor work required from the system, a sensitivity analysis has been conducted on the compressor work to identify the ideal pressure for the system to operate at. Furthermore, an isentropic efficiency of 0.74 is assumed for all evaluated compression steps in this process [123]. The pressure was varied from 30 to 60 bar, and can be seen in Figure D.1

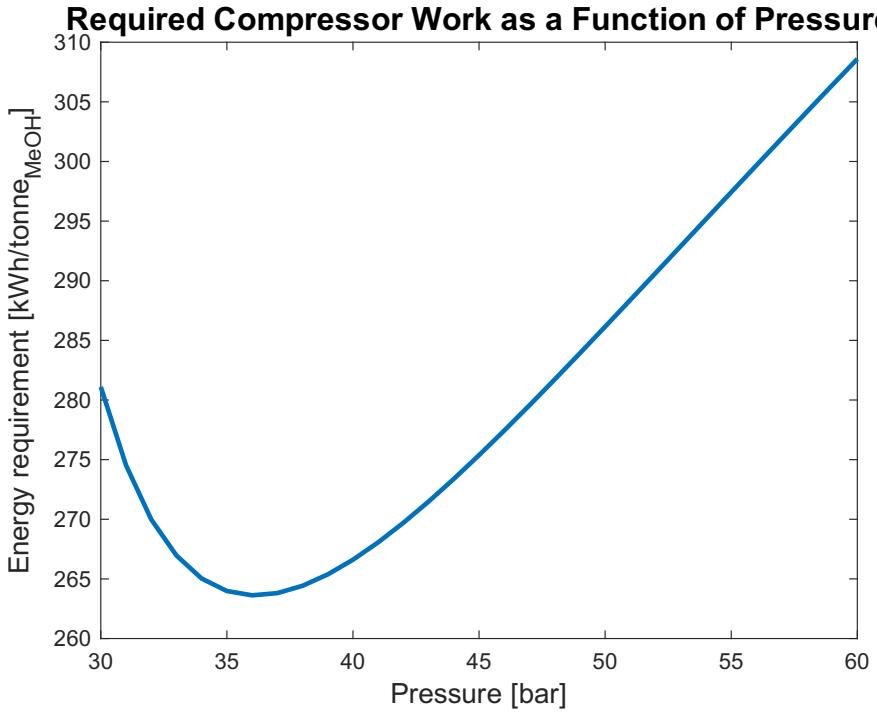

Figure D.1: Sensitivity analysis of required compressor work per tonne of methanol produced as a function of the pressure

It can be seen in Figure D.1 that when the operation pressure is increased, the required compressor work is decreased. However, when an operation pressure of 36 bar is reached, the required compressor work increases again. Furthermore, increasing the pressure beyond 36 bar does not impact the total methanol production. Therefore, the methanol synthesis model was operated at 36 bar to minimize the required input compressor work.

Appendix E

Methanol-to-Hydrocarbon Compounds

The MTH model utilizes a variety of HC compounds to represent the hundreds of different compounds revealed by the GC-MS analysis. Furthermore, the chosen compounds in Table E.1 represents different boiling ranges of HC in the temperature range from 20 °C to 300 °C, along with a variety of gasses which is used to estimate the produced gas composition of the produced gas.

Compound Name	**Chemical Formula**	**Boiling Point [°C]**	**Density$_{25C}$ [g/cm^3]**
N-Paraffins			
Methane	CH_4	-161.49	$6.57x10^{-4}$
Ethane	C_2H_6	-88.6	$1.24x10^{-3}$
Propane	C_3H_8	-42.04	$1.83x10^{-3}$
Butane	C_4H_{10}	-0.5	$2.44x10^{-3}$
Hexane	C_6H_{14}	68.73	0.656
Nonane	C_9H_{20}	150.82	0.717
Decane	$C_{10}H_{22}$	174.15	0.728
Tridecane	$C_{13}H_{28}$	235.47	0.750
Tetradecane	$C_{14}H_{30}$	253.58	0.759
Pentadecane	$C_{15}H_{32}$	270.68	0.764
Hexadecane	$C_{16}H_{34}$	286.86	0.769
Heptadecane	$C_{17}H_{36}$	302.15	0.772
Iso-Paraffins			
Iso-Butane	C_4H_{10}	-11.72	$2.43x10^{-3}$
2-Methyl-Hexane	C_7H_{16}	90.05	0.6734
2-Methyl-Undecane	$C_{12}H_{26}$	210.00	0.742
Olefins			
Ethylene	C_2H_4	-103.74	$1.11x10^{-3}$
1-Propylene	C_3H_6	-47.7	$1.74x10^{-3}$
1-Butylene	C_4H_8	-6.24	$2.34x10^{-3}$
1-Pentene	C_5H_{10}	30.07	0.635
1-Undecene	$C_{11}H_{22}$	192.67	0.747
Cycloaliphatics			
Cyclopentane	C_5H_{10}	49.25	0.741
1,2-Dimethylcyclohexane	C_8H_{16}	129.79	0.792
Aromatics			
Toulene	C_7H_8	110.63	0.864
Other Compounds			
Water	H_2O	100	0.994
Methanol	CH_3OH	64.7	0.789
Carbon-Dioxide	CO_2	-78.45	$1.81x10^{-3}$

Table E.1: N-Paraffins, Iso-Paraffins, Olefins, Cycloaliphatics, Aromatics, and other compounds utilized in the MTH model

E.1 MTH Radfrac and DSTWU Design Specs

This section presents the design specs for the radfracs used in the MTH model. Furthermore, it also presents the initial conditions used in DSTWU columns.

	RADFRAC1	**RADFRAC2**	**RADFRAC3**
	H-ZSM-5(23)		
Reflux Ratio[-]	1.68	1.20	0.11
Number of Stages[-]	18	21	82
Feed $\text{Stage}_{\text{Above Stage}}$ [-]	8	11	42
Condenser Pressure [bar]	1.013	1.013	1.013
Distillate to Feed Ratio [-]	0.38	0.62	0.83
	H-ZSM-5(50)		
Reflux Ratio[-]	3.66	1.09	0.11
Number of Stages[-]	17	21	84
Feed $\text{Stage}_{\text{Above Stage}}$ [-]	8	11	43
Condenser Pressure [bar]	1.013	1.013	1.013
Distillate to Feed Ratio [-]	0.15	0.64	0.81
	Ni-ZSM-5(50)		
Reflux Ratio[-]	4.07	1.33	0.09
Number of Stages[-]	17	21	94
Feed $\text{Stage}_{\text{Above Stage}}$ [-]	8	11	48
Condenser Pressure [bar]	1.013	1.013	1.013
Distillate to Feed Ratio [-]	0.12	0.59	0.89
	Co-ZSM-5(50)		
Reflux Ratio[-]	2.83	0.93	0.19
Number of Stages[-]	17	21	60
Feed $\text{Stage}_{\text{Above Stage}}$ [-]	8	11	31
Condenser Pressure [bar]	1.013	1.013	1.013
Distillate to Feed Ratio [-]	0.20	0.71	0.77
	In-ZSM-5(50)		
Reflux Ratio[-]	3.35	1.18	0.10
Number of Stages[-]	17	21	88
Feed $\text{Stage}_{\text{Above Stage}}$ [-]	8	11	45
Condenser Pressure [bar]	1.013	1.013	1.013
Distillate to Feed Ratio [-]	0.15	0.58	0.86

Table E.2: Input parameters for the radfrac distillation columns in Aspen Plus

In table E.2 the input conditions for the radfac columns based on the specific catalyst can be seen. These conditions is based on achieving a recovery of 95 wt.% of the light fraction, with an allowance of 4 wt.% of the heavy fraction in the light fraction. These conditions are based on initial simulated DSTWU columns, which inputs can be seen

in Table E.3.

	Reflux Ratio	Light Component	Recovery	Heavy Component	Recovery
DSTWU1	-1.4	C_6H_{14}	0.95	C_7H_{16}	0.04
DSTWU2	-1.4	C_9H_{20}	0.95	$C_{10}H_{22}$	0.04
DSTWU3	-1.4	$C_{16}H_{34}$	0.95	$C_{17}H_{36}$	0.04

Table E.3: DSTWU separation conditions with condenser and reboiler pressure of 1.013 bar [120]

The chosen reflux ratio of -1.4 is based on the assurance of sufficient reflux within the condenser column. By having a negative reflux ratio in Aspen Plus, it ensures that the actual reflux ratio is 1.4 times higher than the minimum reflux ratio.